AFRL-ML-WP-TR-2006-4027

NANOSTRUCTURED PROTECTIVE COATINGS

Douglas L. Schulz and Gregory J. McCarthy

North Dakota State University
Center for Nanoscale Science and Engineering
1805 NDSU Research Park Drive North
Fargo, ND 58102

Mark Horn, Paul Sunal, and Russell Messier

The Pennsylvania State University

Robert W. Collins and Chi Chen

University of Toledo

Gary McGuire and Mark Ray

International Technology Center

JANUARY 2006

Final Report for 01 July 2003 – 31 January 2006

STINFO FINAL REPORT

MATERIALS AND MANUFACTURING DIRECTORATE
AIR FORCE RESEARCH LABORATORY
AIR FORCE MATERIEL COMMAND
WRIGHT-PATTERSON AIR FORCE BASE, OH 45433-7750

NOTICE

Using Government drawings, specifications, or other data included in this document for any purpose other than Government procurement does not in any way obligate the U.S. Government. The fact that the Government formulated or supplied the drawings, specifications, or other data does not license the holder or any other person or corporation; or convey any rights or permission to manufacture, use, or sell any patented invention that may relate to them.

This report was cleared for public release by the Air Force Research Laboratory Wright Site (AFRL/WS) Public Affairs Office (PAO) and is releasable to the National Technical Information Service (NTIS). It will be available to the general public, including foreign nationals.

PAO Case Number: AFRL/WS 06-0476, 21 Feb 2006.

THIS TECHNICAL REPORT IS APPROVED FOR PUBLICATION.

/s/

JOHN G. JONES, Project Engineer
Nonstructural Materials Branch
Nonmetallic Materials Division

/s/

JEFFREY H. SANDERS, Chief
Nonstructural Materials Branch
Nonmetallic Materials Division

/s/

PERSIS A. ELWOOD, Deputy Chief
Nonstructural Materials Branch
Nonmetallic Materials Division
Materials and Manufacturing Directorate

This report is published in the interest of scientific and technical information exchange and its publication does not constitute the Government's approval or disapproval of its ideas or findings.

REPORT DOCUMENTATION PAGE

Form Approved
OMB No. 0704-0188

1. REPORT DATE *(DD-MM-YY)*	2. REPORT TYPE	3. DATES COVERED *(From - To)*
January 2006	Final	07/01/2003 – 01/31/2006

4. TITLE AND SUBTITLE

NANOSTRUCTURED PROTECTIVE COATINGS

5a. CONTRACT NUMBER
F33615-03-2-5035

5b. GRANT NUMBER

5c. PROGRAM ELEMENT NUMBER
62102F

6. AUTHOR(S)

Douglas L. Schulz and Gregory J. McCarthy (North Dakota State University)
Mark Horn, Paul Sunal and Russell Messier (The Pennsylvania State University)
Robert W. Collins and Chi Chen (University of Toledo)
Gary McGuire and Mark Ray (International Technology Center)

5d. PROJECT NUMBER
4349

5e. TASK NUMBER
L1

5f. WORK UNIT NUMBER
02

7. PERFORMING ORGANIZATION NAME(S) AND ADDRESS(ES)

North Dakota State University
Center for Nanoscale Science and Engineering
1805 NDSU Research Park Drive North
Fargo, ND 58102

The Pennsylvania State University

University of Toledo

International Technology Center

8. PERFORMING ORGANIZATION REPORT NUMBER

9. SPONSORING/MONITORING AGENCY NAME(S) AND ADDRESS(ES)

Materials and Manufacturing Directorate
Air Force Research Laboratory
Air Force Materiel Command
Wright-Patterson AFB, OH 45433-7750

10. SPONSORING/MONITORING AGENCY ACRONYM(S)
AFRL/MLBT

11. SPONSORING/MONITORING AGENCY REPORT NUMBER(S)
AFRL-ML-WP-TR-2006-4027

12. DISTRIBUTION/AVAILABILITY STATEMENT
Approved for public release; distribution is unlimited.

13. SUPPLEMENTARY NOTES
Report contains color.

14. ABSTRACT (*Maximum 200 words*)

Recent developments in the field of "superhard" coatings are of interest to the Air Force for their potential superior wear resistance properties. The Nanostructured Protective Coatings (NPC) program was designed to establish a collaborative team of three entities having complementary hard materials competencies. The long-term goal was to enhance the fundamental understanding of superhard coatings and utilize this understanding to develop practical coatings needed by the Air Force. Work during the first phase focused on the two component system of nanocrystalline titanium nitride (nc-TiN) and amorphous silicon nitride (a-SiNx) where remarkable hardness values (45-80GPa) were first reported. Because scale-up to industrial-scale processes is the long-range goal of the program, the emphasis has been on physical vapor deposition (PVD) rather than the chemical vapor deposition (CVD) methodologies. The objectives of the first phase were accomplished, particularly in enhancing the understanding of PVD parameters, depositing coatings on practical substrates such as the Ti6Al4V used for turbine blades, and developing a versatile laboratory-scale erosion test relevant to this application.

15. SUBJECT TERMS
superhard coatings, nanocrystalline titanium nitride (nc-TiN), amorphous silicon nitride (a-SiNx), physical vapor deposition (PVD), chemical vapor deposition (CVD)

16. SECURITY CLASSIFICATION OF:			17. LIMITATION OF ABSTRACT:	18. NUMBER OF PAGES	19a. NAME OF RESPONSIBLE PERSON (Monitor)
a. REPORT Unclassified	**b. ABSTRACT** Unclassified	**c. THIS PAGE** Unclassified	SAR	122	John G. Jones **19b. TELEPHONE NUMBER** *(Include Area Code)* (937) 904-4327

Standard Form 298 (Rev. 8-98)
Prescribed by ANSI Std. Z39-18

Table of Contents

Abstract

Recent developments in the field of "superhard" coatings (generally defined as those having Vickers hardness in excess of 40 GPa) are of interest to the Air Force for their potential superior wear resistance properties. The Nanostructured Protective Coatings (NPC) program was designed to establish a collaborative team of three entities (Pennsylvania State University, International Technology Center, and North Dakota State University) having complementary hard materials competencies. The long-term goal was to enhance the fundamental understanding of superhard coatings and utilize this understanding to develop practical coatings needed by the Air Force. Work during the first phase of what was designed as a multiphase program focused on the two component system of nanocrystalline titanium nitride (nc-TiN) and amorphous silicon nitride (a-SiN$_x$) where remarkable hardness values (45-80GPa) were first reported by Veprek and co-workers. Because scale-up to industrial-scale processes is the long-range goal of the program, the emphasis has been on physical vapor deposition (PVD) rather than the chemical vapor deposition (CVD) methodologies used by Veprek. The objectives of the first phase of this study were to: (1) study the deposition, characterization, and optimization of Ti-Si-N nanocomposites; (2) analyze interface structures *in-situ* during deposition using real-time spectroscopic ellipsometry (RTSE), and *ex-situ* by a variety of analytical techniques and mechanical properties measurements; and (3) establish at North Dakota State University's new Center for Nanoscale Science and Engineering the capability to deposit and evaluate hard coatings for military needs. The project accomplished its Phase I objectives, particularly in enhancing the understanding of PVD parameters, depositing coatings on practical substrates such as the Ti6Al4V used for turbine blades, and developing a versatile laboratory-scale erosion test relevant to this application.

1.0 INTRODUCTION

Recent developments in the field of "superhard" coatings (generally defined as those having Vickers hardness in excess of 40 GPa) are of interest to the Air Force for their potential superior wear resistance properties. Instead of being a single uniform material, superhard coatings are nanometer-scale, alternating layers of nanocrystalline (nc) and amorphous (a) materials (known as multilayers or superlattices), or nanocomposites of these materials. A substrate interface layer may also be part of the coatings system. Thin coatings of such materials can provide protection of surfaces against wear in vital applications such as machining tools. They can also be applied at high wear interfaces in military vehicles and in extreme environments such as those in space. In addition to great hardness, these coatings can add oxidation resistance, chemical stability, low coefficient of friction, and toughness, and can be tailored for excellent adherence and compatibility to the substrate.

The long-term *goal* of the Nanostructured Protective Coatings (NPC) program is to apply innovative methodology to develop a fundamental understanding of the materials, deposition parameters, and resultant nanostructures that will lead to new superhard nanostructured protective coatings that meet military needs. Work during the first phase of what was designed as a multiphase program focused on the two component system of nanocrystalline titanium nitride (nc-TiN) and amorphous silicon nitride (a-SiN$_x$) where remarkable hardness values (45-80GPa) were first reported by Veprek and co-workers. Because scale-up to industrial-scale processes is the long-range goal of the program, the emphasis has been on physical deposition (PVD) rather than the chemical vapor deposition (CVD) methodologies used by Veprek.

The *objectives* of the first phase of this study were to: (1) study the deposition, characterization, and optimization of Ti-Si-N nanocomposites; (2) analyze interface structures *in-situ* during deposition using real-time spectroscopic ellipsometry (RTSE), and *ex-situ* by a variety of analytical techniques and mechanical properties measurements; and (3) establish at North Dakota State University's new Center for Nanoscale Science and Engineering the capability to deposit and evaluate hard coatings for military needs.

This program was a collaboration of three entities having different emphases and bringing different research capabilities:

- Pennsylvania State University (PSU), University Park, Department of Engineering Science and Mechanics, and the Materials Research Institute. Pulsed DC sputter deposition, plasma characterization, RTSE, hard coatings and thin film materials characterization. During the course of the work, Prof. Robert Collins moved to the University of Toledo, but continued his work on the program, jointly at Toledo and Penn State.
- International Technology Center (ITC), Research Triangle Park, North Carolina. Ion beam sputter deposition (IBSD) and cathodic arc deposition, thin film materials characterization.
- North Dakota State University (NDSU) Center for Nanoscale Science and Engineering (CNSE). Testing methodology, and scale-up after transfer of NPC deposition technology from PSU.

The three entities collaborated electronically, through monthly conference calls, and through off-site workshops.

The period of performance for the work presented here was two years, roughly from the summer of 2003 through summer of 2005.

The project accomplished its Phase I objectives, particularly in enhancing the understanding of PVD parameters, depositing coatings on practical substrates such as the Ti6Al4V used for turbine blades, and developing a versatile laboratory-scale erosion test relevant to this application.

1

2.0 NPC PROGRAM AT THE PENNSYLVANIA STATE UNIVERSITY

2.1 Introduction

The program at PSU can be separated into two distinct components. One was the thorough investigation of the formation of nanocomposites using pulsed-dc sputter deposition and the other was using real-time spectroscopic ellipsometery to evaluate the evolution of TiN nanocrystals. These two topics will be discussed in full in separate sections (2.2 and 2.3/Appendix A) and general conclusions and recommendations will be given for both in Section 2.4.

2.2 Pulsed DC Sputter Deposition of Nanocomposites

2.2.1 Depositional Methods and Parameter Characterization

The nc-TiN/a-SiN$_x$ films were deposited using reactive pulsed dc magnetron co-sputtering. The solid materials used for film fabrication were obtained from Kurt J. Lesker Co. and consisted of three inch sputter targets 7.62 cm (3 inch) $\times$ 6.35 mm (0.25") of titanium (99.995% purity) and phosphorous doped n-type silicon (99.999% purity). The reactive sputtering gases are 99.99% purity argon and nitrogen (99.99% purity). The targets were properly conditioned using an initial one hour burn-in that starts with a 30 minute, low power (50 W) soak. This was followed by a 0.5 W/sec ramp to the final maximum power at which sputtering occurred during film deposition. For the titanium target, the final power is 400 W and 150 W for the silicon target.

The deposition system is a circular system with two 7.62 cm (3 inch) Torus sputter guns from Kurt J. Lesker. One gun is mounted 90° with respect to the film plane and the other is offset 45° to one side (refer to Figure 2.2-1) in a sputter down configuration. The vertically mounted gun houses titanium target while the 45° gun the silicon target. The angled configuration of the silicon target containing sputter gun provided a combinatorial approach to film deposition with respect to the film ratio of TiN to SiN$_x$. Constant power densities of 8.8 W/cm^2 and 3.3 W/cm^2 are used for the Ti and Si targets, respectively. The chamber is pumped by a Pfeiffer 520 l/s turbo pump backed by a mechanical pump with typical base pressures of 1.3×10^{-5} Pa (1×10^{-7} Torr). The substrates are placed on a 7.62 cm diameter heated, biased substrate stage (SU300) from US Incorporated. Electric heating tape provided continuous heating of the chamber walls to temperatures between 60–90° C. Since the tape was wound around the barrel of the cylindrical chamber, the door and back circular wall were at the lowest temperature. Heating of the chamber reduces the adsorption of water and other gaseous molecules onto the inner chamber surfaces. This heating reduces the pumping time and level of contamination, specifically of water, which has been shown to be an essential step with these films.

The sputter guns are each powered by an ENI RPG-50 pulsed dc power supply, which generates an asymmetric bipolar signal when operating in pulsing mode. The pulsed dc mode is limited with respect to the frequency range, duty cycle, reverse, and duty voltages. The signal generated is bipolar and asymmetric but can only output frequencies from 50 to 250 kHz with a fixed reverse voltage of +90 to +100 V regardless of the frequency. The ENI-RPG50 power supplies have the capability to be programmed to run recipes for the ramp-up and film sputtering processes.

Preliminary characterization of films sputtered with Ar/N$_2$ at various ratios indicated that the Si$_3$N$_4$ phase were substoichiometric, i.e. nitrogen deficient. Thus, the depositions were performed using pure nitrogen atmosphere at pressures of 0.67 and 1.33 Pa (5 and 10 mTorr) to encourage the maximum amount of nitrogen disassociation and ionization. An adhesion layer of ~40 Å thick Ti having a surface roughness of 4–5 Å was consistently used to optimize the adhesion of the subsequently deposited nanocomposite film. The vacuum is not broken in between the adhesion layer and nanocomposite film. Specific sputter parameters for the adhesion layer came from work on the RTSE system and are as follows:
1) 1.33 Pa (10 mTorr) of argon.
2) 40 second deposition.
3) 100 W of power at 166 kHz with a duty cycle of 50 % (3 μs).

For the nanocomposite thin film deposition, ramp-up and film sputter recipes are shown in Tables 2.2-1 and 2.2-2. Once the deposition has completed, the gases are turned off, the power supplies are shut down, and the chamber

vented with nitrogen. The substrates are promptly removed and the XRD glass is stored in a vacuum desiccator. The other substrates are immediately used to determine the film thickness and stress.
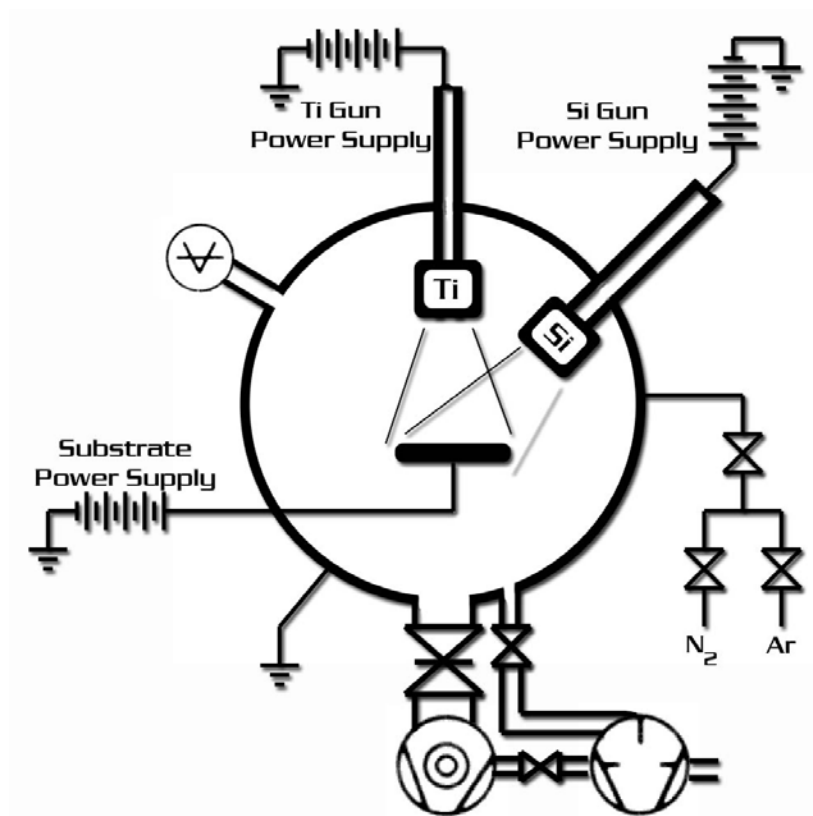

Figure 2.2-1. Schematic of the deposition system used to fabricate Ti-Si-N nanocomposites.

Table 2.2-1: Ramp–up recipe followed for each nanocomposite deposited.

Power (W)	Time (sec)
0 – 50 (both Ti and Si)	10
50 (both Ti and Si)	60
50 – 400 (Ti)	350
50 – 150 (Si)	350

Table 2.2-2: Film sputter recipe followed for each nanocomposite deposited.

Power (W)	Time (sec)
400 (Ti) 150 (Si)	Time required to deposit desired thickness
400 – 0 (Ti) 150 – 0 (Si)	5

2.2.2 Deposited Film Characterization

The thin films are deposited onto silicon and glass substrates for charaterization by XPS, XRD, FTIR, nanoindentation, and stress measurements. During a standard deposition, glass and silicon substrates are used for the various characterization techniques. The film thickness and, consequently, the deposition rate are computed from

3

step profiles obtained using a Tencor® P-10 profilometer, while the electrical resistivity of the films is measured using a 4D Model 280C four–point probe instrument with an attached pc for automated, repeatable routines.

The plasma within the system was characterized with respect to the plasma density, ion species, and energies. Combining information gathered from a Langmuir probe and a Hiden Analytical Limited Electrostatic Quadrupole Plasma (EQP) analyzer paints a comprehensive picture of the bombardment of the growing film on the substrate. A Scintag Model X2 theta-theta goniometer with Cu K alpha–1 / alpha–2, normal focus x-ray tube XRD system was used to investigate the crystallinity of the films and determine the preferred orientation. Since the films are composed of nanometer sized crystals, grazing angle geometry was used to collect the data. On average, the acquisition times were long (on the order of 1 hour per sample) since the scan range was 10˚ to 64˚ in 0.02˚ steps with a 2.5 second count time.

Compositional information was obtained by a Kratos Analytical Axis Ultra XPS with an Al Kα source and depth profile capable using argon ion etching. The tool was used to obtain relative composition of titanium, silicon, oxygen, carbon and nitrogen after ion milling 20 nm into the film. Bonding energy information was then analyzed to verify the phases present and the level of mixing. The identification of elemental silicon, silicon dioxide, and silicon nitride is possible from where the bonding energy peaks occur.

Morphology analysis is conducted with a Leo 1530 field emission SEM. The images produced permit identification of the film morphology and measurement of the size scales involved therein. A conductive gold or carbon coating is not needed to avoid charging effects since the films are conductive. This eliminates any conductive coating artifacts and allows inspection of the actual film. To get a better idea of the nanostructure of these films, TEM analysis was utilized. Very thin nanocomposite films on the order of ~500 Å were deposited onto 3 mm diameter copper grids. Since the analysis occurs through transmission, the films needed to be on the order of the expected nanocrystal size. The grids have a carbon film on one side allowing the nanocomposite to deposit on open areas in the copper grid.

A Tencor® FLX–2320 with two different lasers of 720 nm and 650 nm wavelengths, are available to measure the sample curvature before and after film deposition with a resolution of 0.00003 m^{-1}. The substrates were measured across the center of the square (0°) and one of the diagonals (–45°). Preliminary hardness, H_v, and reduced modulus, E_r, information were measured on a Hysitron Triboindenter. A dedicated diamond Berkovitch indenter tip was used to perform nanoindentation on the films.

2.2.3 Results and Discussion for DC Sputtered Films

The first order of business with respect to fabrication of these thin films is to verify that we are depositing a material with nanoscale sized crystallites. This nanostructure is critical for goal of improving the mechanical hardness according to the guidelines put forth by Veprek and Reiprich [1]. The initial XRD results shows that there are nanometer-sized crystallites from the low intensity and broad peaks as seen in Figure 2.2-1.

The Scherrer formula gives crystallite sizes of 38, 19, and 16 nm for the (111), (200), and (220) orientations, respectively. The preferred orientation for all the nanocomposite thin films is the (200), whose Scherrer formula calculated crystal size is representative of the majority nanocrystals found in the thin film.

To verify the nanocrystalline structure and sizes found from the XRD results, TEM was used to image the material. From the bright field images, the presence of a nanocrystalline material is obvious (Figure 2.2-3). Measurement of the actual crystal size for the same film conditions as shown in Figure 2.2-3 yields a crystal size of 6 nm.
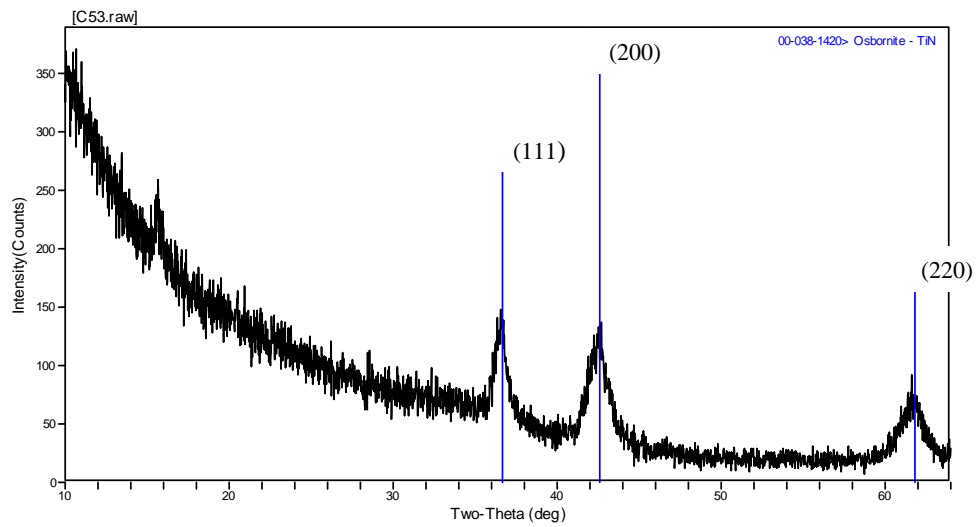
Figure 2.2-2. XRD profile for a Ti-Si-N nanocomposite deposited at 5 mT N_2 and 250 kHz.
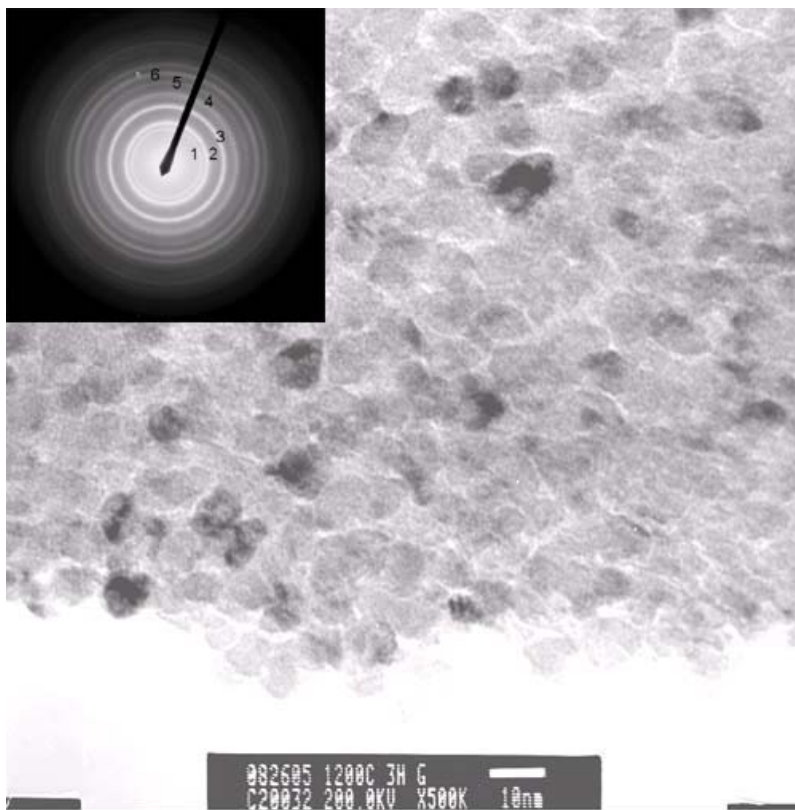

Figure 2.2-3. TEM bright-field image of a Ti-Si-N nanocomposite deposited at 5 mT N_2 and 250 kHz showing the distinct nanocrystalline structure.

The next design criterion to meet is to verify that the TiN and SiN$_x$ phases are indeed present. To accomplish this, XPS binding energies were investigated. The accepted Ti 2p value for the TiN phase is 455.4 eV, while it is 101.6 eV for Si 2p in the SiN$_x$ phase. Figure 2.2-4 shows the variation of both the Ti and Si 2p peaks as a function of pulsing frequency. The slight variation at the low frequencies correlates to the increased Si content found in these films, while the decrease at 200 kHz indicates some degree of elemental silicon within the film. Overall, these results indicate that both TiN and SiN$_x$ are present within the nanocomposite thin films. However, the XPS results found high relative concentrations of oxygen (1 – 5 at. %), which appeared to have consequences for the mechanical properties of the film.

The next step in the process of investigating these fabricated Ti-Si-N nanocomposites was to mechanically test them using the Hysitron Triboscope. Upgrades to the Hysitron Triboscope were recently made and include: a dedicated AFM, hardware changes that eliminate noise in the load-displacement data, and software changes that vastly improve tip drift correction issues. Hardness and modulus data taken on this instrument are very reliable due to these upgrades and improved indenting protocol on the user side. Most notably, the drift rates during indenting have been reduced to under 0.1 nm/sec and typically are under 0.05 nm/sec, which lends confidence in the numbers generated for H$_v$ and E$_r$. Results for the 10 mT N$_2$ series of nanocomposites are shown in Figure 2.2-5.

The thin films shown in Figure 2.2-3 were indented using three depths corresponding to 5, 10, and 15 % of the total film thickness. This was done because there is no consensus in the literature pertaining to a standardized indent depth, which is doubtful to ever exist due to variation in film properties. The deeper 10 and 15 % indent depths show better correlation with each other than does the 5 %, which, after investigation of the surface roughness, is on the order of the surface roughness. Therefore, the indents at 5 % are unreliable and should be disregarded, but are worthy to note since they show a danger in indenting to too shallow a depth.

To better understand the variation in the H$_v$ results, an investigation of the plasma properties was conducted. This reasoning behind looking at the plasma was that all the many variables in PVD affect the plasma, which is responsible for the bombardment of the growing thin film. One single variable was identified and investigated as something that is universal among PVD systems. This variable is the momentum-per-atom at the growing film surface. When this is identified, it can then be related to the mechanical properties. This relationship allows one to engineer the mechanical properties of these Ti-Si-N nanocomposites, irrespective of the PVD system in which they are fabricated. This allows the momentum-per-arriving atom to be a universal variable that can be used by anyone on any PVD system to engineer their Ti-Si-N nanocomposite thin film mechanical properties.

The first step in analysis of the momentum-per-atom was to use a Langmuir probe to determine the probe potential, which is used to calculate various other plasma properties. The probe was biased and swept from -50 to +50 V, while the probe voltage was recorded using an oscilloscope. A typical plot of the measured probe voltage versus the calculated probe current and the resulting curve fit are shown in Figure 2.2-6. Ultimately, the momentum per arriving atom was calculated from the calculated plasma potential, density, and floating potential. The raw probe and bias voltage data for each scan were loaded into a Matlab m-file and used to plot and calculate all of the properties. The minimum of the derivative curve, shown in Figure 2.2-6(b), determines the plasma potential.

The probe was positioned at the substrate to measure conditions that the growing film would experience. Therefore, the plasma potentials are lower than if the probe were directly in the plasma. However, the momentum values should represent closely level of bombardment at the growing film surface. To determine the momentum-per-atom, the equation

$$\frac{P}{a} = \sum \frac{J_i}{a} \sqrt{2m_i E_i} \qquad \text{(amu eV)}^{\frac{1}{2}}$$

was used. The equation sums the contributions from all ionized species present in the plasma from the J$_i$/a term, which is the ion current density over the total arriving flux of atoms.

The ionized species present in the plasma was determined using a Hiden EQP mass and energy analyzer. This instrument was used to determine the ratio of the major ionized species at the substrate position. It was found that the majority of the ionized species in the plasma is N$_2^+$ with N$^+$, Ti$^+$, SiN$^+$, and TiN$^+$ comprising the remaining species. The energy analysis of N$_2^+$ and N$^+$ show that distribution is bimodal with a larger low energy peak <5 eV

6

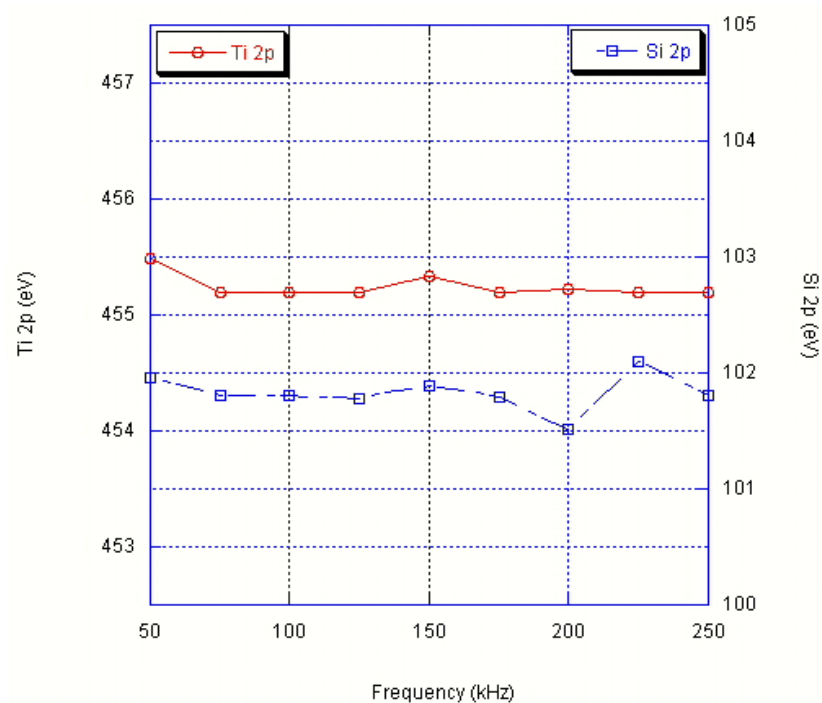Figure 2.2-4. The XPS binding energies for Ti and Si 2p as a function of pulsing frequency. The values vary little from accepted energy numbers and give confidence that TiN and SiN_x phases are present in the thin films.
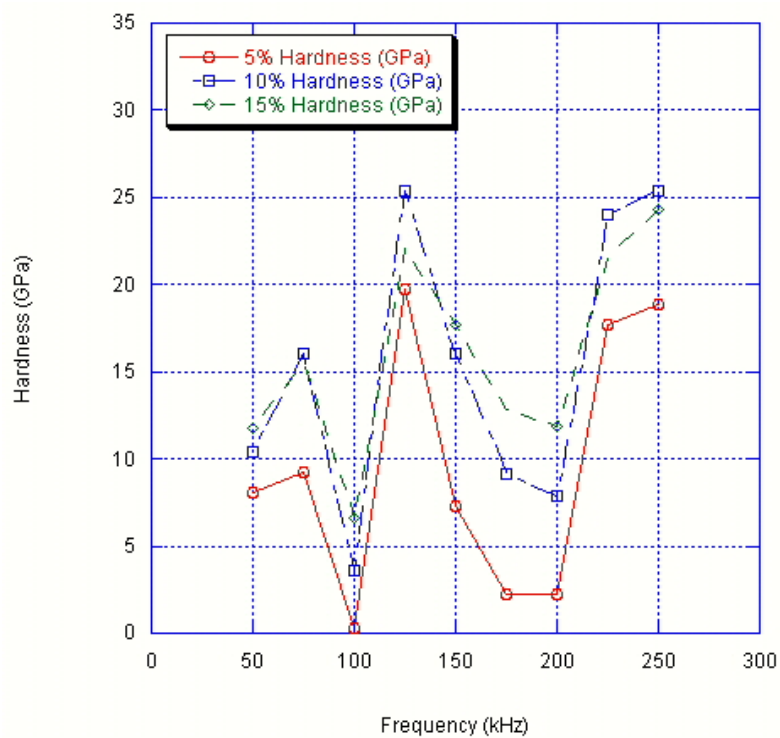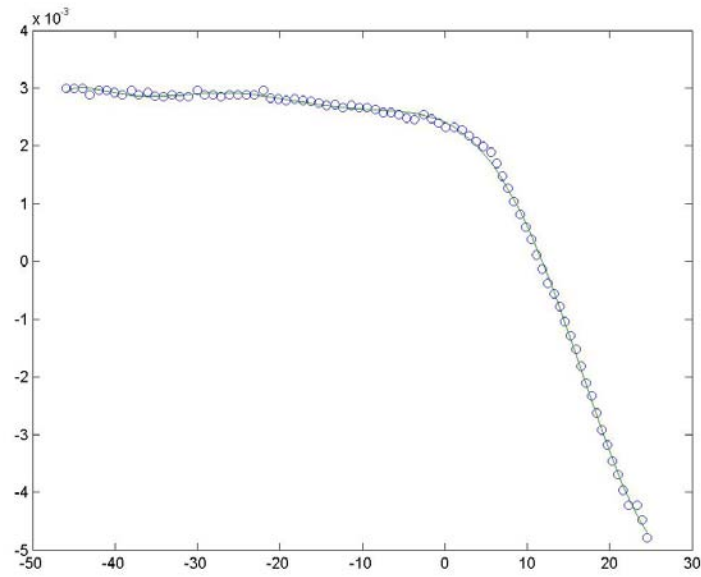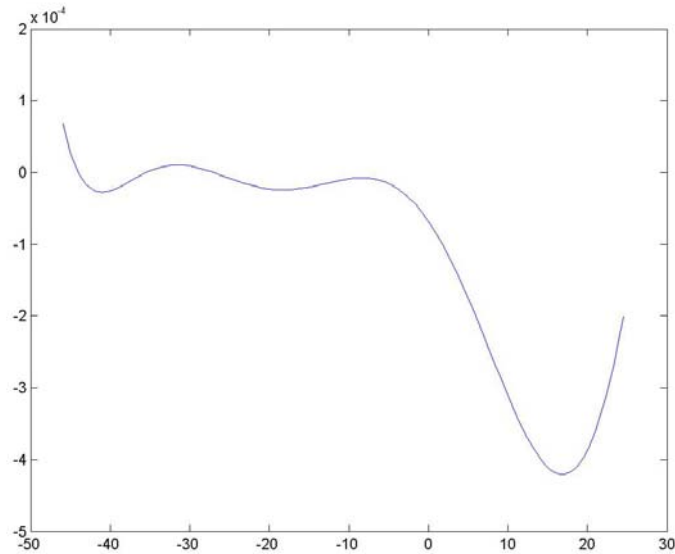

Figure 2.2.-5. Variation of the Vickers hardness with pulsing frequency and indent depth (% of total film thickness) for a Ti-Si-N nanocomposite deposited at 10 mT N_2.

7

(a)

(b)

Figure 2.2-6. Plot of (a) the measured Langmuir probe voltage vs. current and b) the calculated derivative from which the plasma potential is measured at the minimum. (250 kHz, 5 mT N$_2$)

and a smaller higher energy peak of 70 to 75 eV. The high energy peaks were about four orders of magnitude less than the low energy peaks, yet still play the larger role in contributing to the momentum-per-atom.

The final step is to compare the mechanical properties of the TI-Si-N nanocomposites to the momentum-per-atom and draw conclusions. Figure 2.2-7 shows the momentum-per-atom and the Vickers hardness as a function of pulsing frequency. There appears to be a good correlation between the hardness and the momentum-per-atom as a

8

function of frequency. The variation is due to the variation of the ion flux at the growing film surface. The mass of the ions appears not to affect the momentum to a large degree.
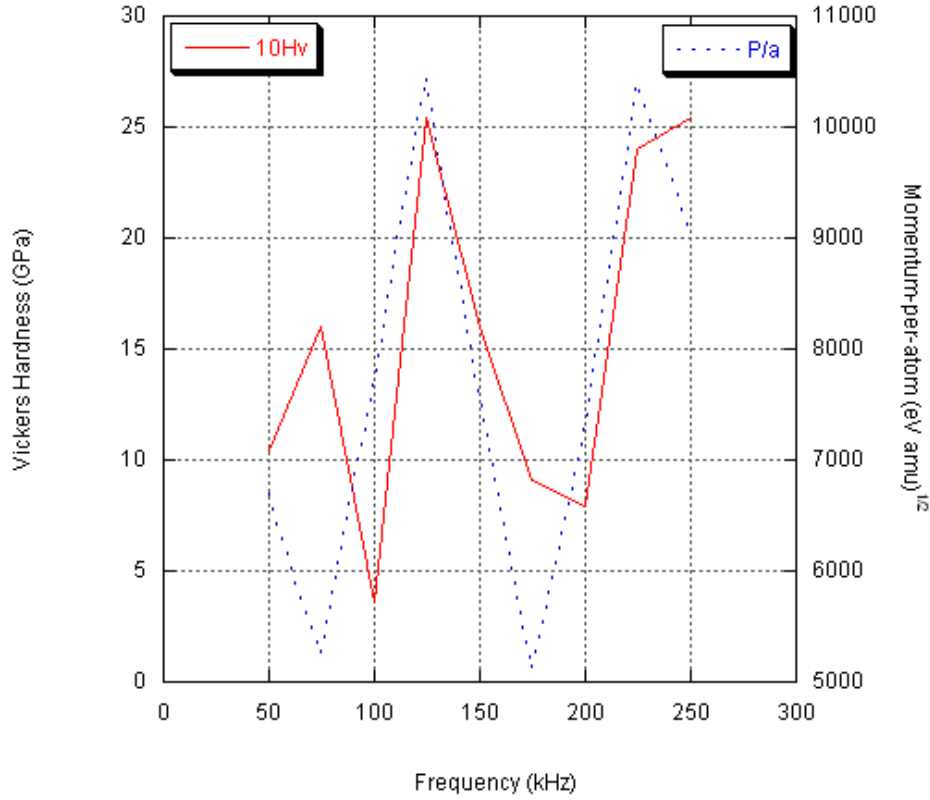

Figure 2.2-7. The Vickers hardness plotted with the momentum-per-atom (P/a) as a function of frequency. There is a correlation between the two indicating that as P/a increases, so to will the hardness.

When the hardness is plotted with against the momentum and a linear fit is performed, the required momentum necessary to produce a nanocomposite with a certain hardness is defined. Figure 2.2-8 shows that as the pressure is increased from 5 to 10 mT, the momentum required also increases. This trend is assumed to continue as the pressure increases further. A possible explanation may lie with the contribution of energetic neutrals contributing to the overall momentum-per-atom delivered to the growing film surface. Since we did not have the capability to measure this quantity, it was not included in the momentum analysis. This does not mean there is no contribution by energetic neutrals, which may be measured by comparing nanocomposite hardness between very high pressures and comparing to nanocomposites deposited using very low pressure.

A revised equation that considers energetic neutrals is

$$\frac{P}{a} = \frac{P_I}{a} + \frac{P_N}{a}$$

where P_I is the ion contribution and P_N is the energetic neutral contribution to the overall delivered momentum-per-atom. Inserting the contribution by each ion and neutral specie results in

$$\frac{P}{a} = \sum_i \left(\frac{J_i}{a} \sqrt{2 m_i E_i} \right) + \sum_j \left(\frac{J_j}{a} \sqrt{2 m_j E_j} \right) \qquad \text{(amu eV)}^{\frac{1}{2}}$$

which includes all particles bombarding the growing thin film. A method to determine the flux of energetic neutrals must be developed before they can be included in the aforementioned equation.
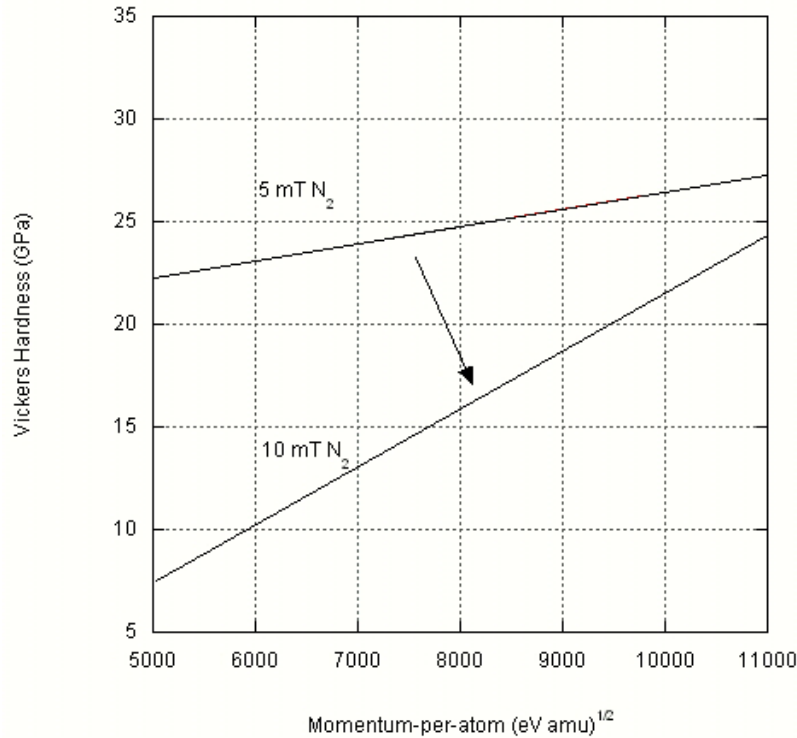
9

Figure 2.2-8. The plot shows pressure dependence on the momentum-per-atom with respect to the resulting hardness. The linear fit indicates that a higher momentum is required for a constant hardness as the pressure increases.

A statistical approach was taken in order to help identify which process and property variables play the largest role in determining the resulting mechanical properties. A linear correlation was performed between many variables including: plasma density, plasma potential, electron temperature, ion flux, momentum-per-atom, the amount of crystallographic orientations, and the film stress. From loading plots shown in Figure 2.2-9(a and b), the best correlations are lines that overlap the 10Hv lines or are opposite from it.

From these plots, a correlation matrix lists the percent of variability explained by each individual variable with respect to the hardness. A confidence is listed (p-value) for each of the correlation values listed. For the nanocomposites deposited at 10 mT, there is a positive correlation between the momentum and hardness, where the momentum explains 68% of the variation in the hardness with a 96% confidence. The 5 mT data series is a bit more difficult to relate directly to the momentum. The hardness at 5 mT best correlates with the relative amount of (111) crystallographic orientation, in a negative manner. The relative amount of (111) crystallographic orientation explains 83% of the variability in the hardness with 99% confidence. Interestingly, the momentum explains the greatest variability in the relative amount of (111) orientation (83% with 53% confidence). This indicates an indirect route relating the momentum to the hardness, through the relative amount of (111).

2.3 Real Time Spectroscopic Ellipsometry of Ti and TiN Films

The reader is referred to Appendix A for a report prepared by Professor Robert Collins.

2.4 Conclusions and Recommendations

Fabrication of hard thin films according to Veprek's generic design principles were investigated using the Ti-Si-N material system. The thin films were fabricated using a unique experimental setup consisting of two synchronized sputter sources powered by a pulsed dc (mid-rf) signal in a reactive environment (N_2).
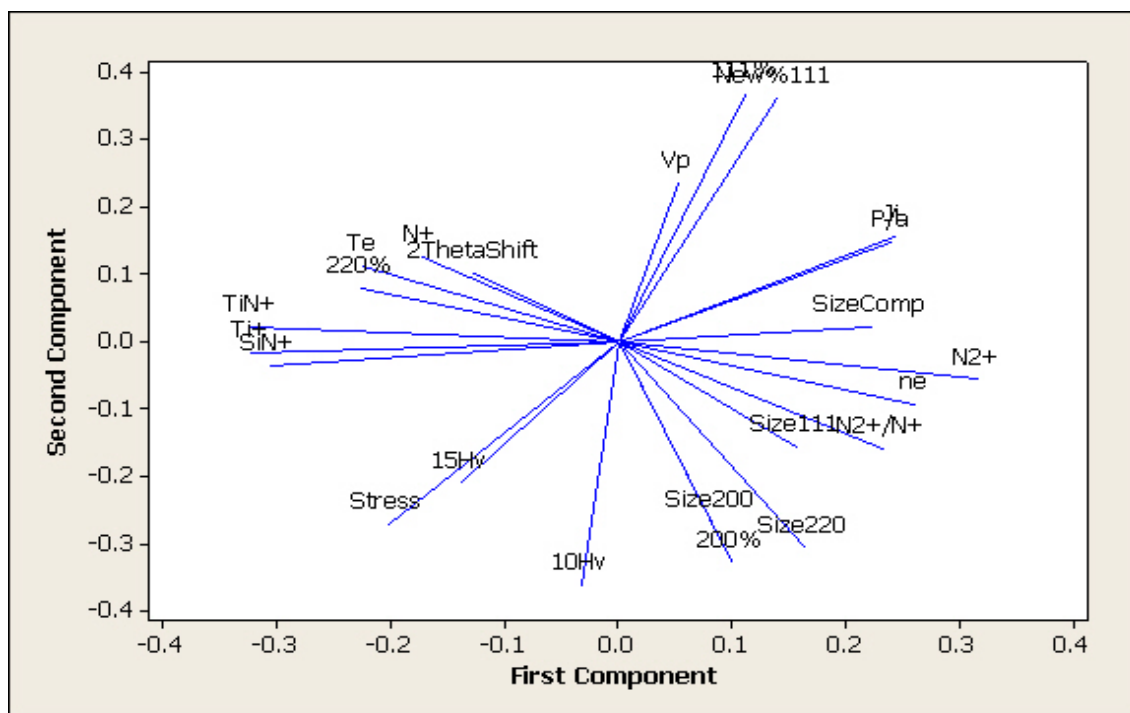
(a)
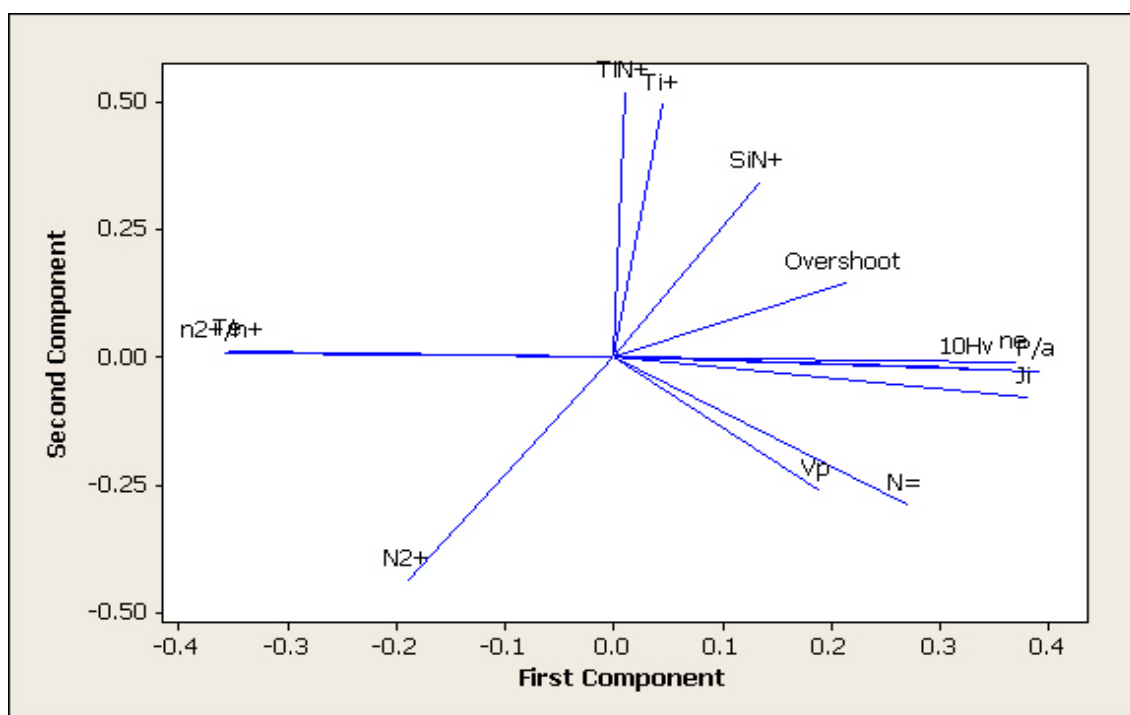
(b)

Figure 2.2-9. Loading plots that graphically show the correlation between process variables for nanocomposites deposited at (a) 5 mT and (b) 10 mT.

11

The characterization of the film nanostructure clearly shows that they are nanocomposites. This is found from the low intensity and broad XRD peaks and bright-field TEM images. The nanocrystal sizes range from 5 to 40 nm depending on deposition conditions. Phase identification was completed using XPS, which found the Ti and Si 2p binding energies indicative of TiN and SiN_x phases. A problem with oxygen contamination was identified and addressed, but we were unable to decrease the oxygen content below 1 at. %.

The mechanical properties of the films show them to be less hard than those reported by other investigators looking at the same material system by PVD. The maximum hardness obtained in the present study was 33 GPa in a film deposited at 5 mT N_2 at 250 kHz with the substrate biased with -75 V. Oxygen impurities are a likely cause of the lower hardnesses compared to literature values for the pure system. This would be consistent with recent reports by Veprek et al. [2] that as little as 1 at.% of oxygen causes a decrease in hardness to the 30GPa range, instead of the 45-55GPa typical of pure Ti-Si-N nanocomposites

Identification of a universal variable, the momentum-per-atom, and calculation of its value at various sputter pressures and pulsing frequencies were completed using a Langmuir probe and a mass-energy analyzer. The momentum-per-atom was found to correlate to the hardness of the fabricated Ti-Si-N nanocomposite thin films, allowing a degree of mechanical property engineering.

During work on RTSE of Ti deposition it was found that a narrow range of sputtering pressure (~10 mTorr) promotes surface diffusion without bombardment damage. This leads to (i) the largest clusters in the nucleation stage of growth (ds= 17 Å at db= 0 Å); (ii) the strongest coalescence effect (Δds = 14 Å for db = 3 $\rightarrow$ 50 Å); and (iii) the smoothest surface after coalescence (ds = 3 Å at db = 55 Å). To obtain a stable surface during bulk film growth and the smoothest surface in a thick film, a low pressure is best (optimum case at 2.5 mTorr: ds = 30 Å at db = 300 Å). To obtain the highest density film during bulk growth, a low pressure and a low power are best (optimum case at 5 mTorr and 50 W).

The observations made during the growth of TiN films show features common to those made during Ti growth. First, immediate roughness development and evolution is observed at the lowest pressures, whereas nucleation and coalescence to smooth surfaces are observed under conditions of moderated ion bombardment. In addition, longterm stability of surfaces at low pressures is noted, whereas significant instability occurs at high pressures. TiN clusters ~15-50 Å in size can be obtained in one and two step processes, and these may be suitable for formation of controlled nanocomposite structures. Finally, atomically smooth TiN films having thicknesses in the range of ~ 20 - 50 Å can be obtained at elevated pressures for incorporation into coherent multilayer structures.

Work identified for a follow-on study includes: exploration of RTSE of nanocomposites with two sputter guns where the nanocomposites could be fabricated using simultaneous deposition or multilayer deposition; and further exploration of pulsed DC sputter deposition of nanocomposites with non-columnar morphology and low oxygen content.

References Cited

[1] Veprek, S. and S. Reiprich (1995). "A concept for the design of novel superhard coatings." *Thin Solid Films* **268**: 64-71.

[2] Veprek, S., H.-D. Maenning, A. Niederhofer, D. Ma, and S. Mukherjee (2004). "Degradation of superhard nanocomposites by built-in impurities." *J. Vac. Sci. Technol.* **B22(2)**: L5-L9.

3.0 NPC PROGRAM AT THE INTERNATIONAL TECHNOLOGY CENTER

3.1 Introduction

The goal of Nanoprotective Coatings was to produce superhard coatings with hardness >40GPa, and to determine the growth conditions for such films in terms of growth rate, temperature, composition, and ion bombardment. These conditions are not transferable to all deposition systems, therefore the ultimate goal was to further breakdown the growth conditions to determine the energy or momentum per atom at the surface required to achieve superhard films. This universal parameter for describing ion surface interactions could then be translated to any deposition system once the growth parameters of that system had been completely studied.

International Technology Center (ITC) proposed using an Ion Beam Sputter Deposition (IBSD) system for the analysis of these conditions. Single composition and multi-layer superlattice films were proposed that had similar compositions to the continuous composition nanocrystalline films grown by PSU. The films were grown in the IBSD system which was originally designed for depositing multilayer metal thin films over a 100mm to 150mm wafer area with an edge to edge uniformity of $\pm$ 1%. The advantage that ion beams provide in determining the energy per atom is that the current and energy of the beams are independently controlled. In magnetron systems, there is no independent control of both energy and ion flux, making characterization of magnetron sputter deposition systems critically important. The ion beam deposition system can also vary the energy per incident atom over a much wider range by using a second ion beam directed at the growing film. This provides a range of bombardment energies from a few eV per atom to hundreds of eV per atom. The disadvantage for ITC's ion beam system is that the deposition rates are very low, on the order of tens of Angstroms per minute. Therefore, ITC proposed a combinatorial approach for TiN_x and Si_xN_y nanocrystalline compositional analysis. By depositing from a multicomponent target, several samples would provide a range of compositions for testing. Since a single deposition would take approximately 12 hours to deposit a micron of film, the combinatorial approach was very appealing.

Along with ion beam deposition, ITC undertook the building of a cathodic arc deposition system. As compared to ion beam sputter deposition, cathodic arc deposition has a higher deposition rate and is capable of very thick film deposition. Cathodic arc deposition is also capable of higher energy bombardment than ion beam deposition. The high energy deposition provides dense films with excellent adhesion from shallow implantation of the growing film at the substrate surface. The result is a method of growth which can cover higher ranges of bombardment energy than either magnetron or ion beam sputter deposition. The goal here was to expand the growth model to higher energies to see if further high hardness states could be reached and to contrast the two models. The cathodic arc deposition system does lend itself to a similar analysis of energy and flux during growth, however very few detailed models have been made for cathodic arc deposition in these terms [2,3].

The results to date have not been in the superhard category. The results have been dominated by two effects: film stress and oxygen impurity concentration. Most of the effort has been focused on reducing these difficulties so as to provide adequate hardness testing thickness and increased hardness during testing. The results to date will be shown in the following sections.

3.2 IBSD Methods, Procedures and Results

The ion beam system is an ultra-high vacuum system with a base pressure of ~$1x10^{-9}$ Torr. The system is capable of substrate heating to 600C. The uniformity of the deposition system is excellent due to the rotation capability of both the target and substrate. A general schematic of the system is shown in Figure 1.

Instead of using two targets as shown in Figure 3.2-1, ITC used a split target without target rotation in order to deposit enough different sample compositions for a combinatorial approach to deposition. The results of this deposition are shown in Figure 3.2-2. The target was repositioned several times in order to achieve a deposition maximum at the center of the 100mm wafer. However, using a non-uniform deposition pattern would allow ~20% composition range to be generated in a single deposition run. According to the literature, a 10-25% composition range should be more than adequate to determine a peak composition in superhard materials [6,7].

The deposition rate varied across the surface but the peak of the deposition was maintained in the center of the wafer as shown in Figure 3.2-3.

The second ion beam was added during the first year of this contract and was directed at the substrate. The second ion beam was to be used as an auxiliary source of nitrogen and a method of increasing the bombardment of the growing film to foster nanocrystalline growth. The ion beam uniformity and current was examined in the low energy
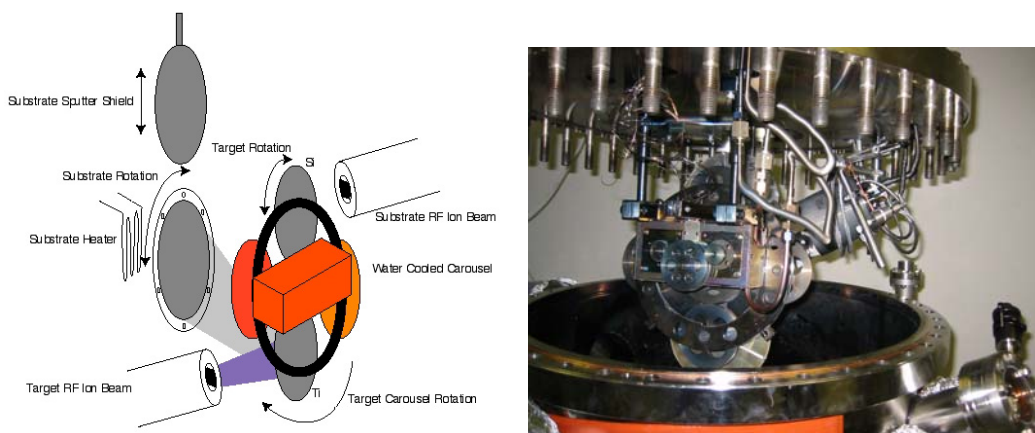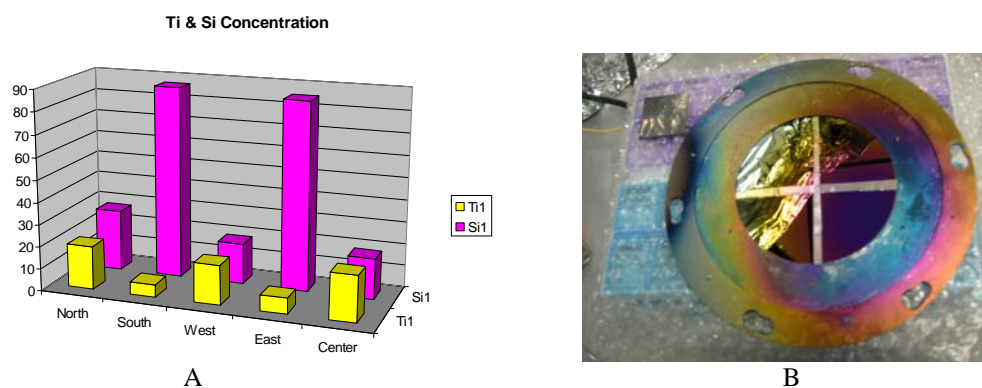

Figure 3.2-1. Schematic and photograph of IBSD system.

A

B

Figures 3.2-A and B. 2A. Composition of Ti and Si across a 100mm substrate from the primary ion beam using a split target of Ti and Si. 2B. Sample after deposition showing the deposition maximum in the southeast quadrant.
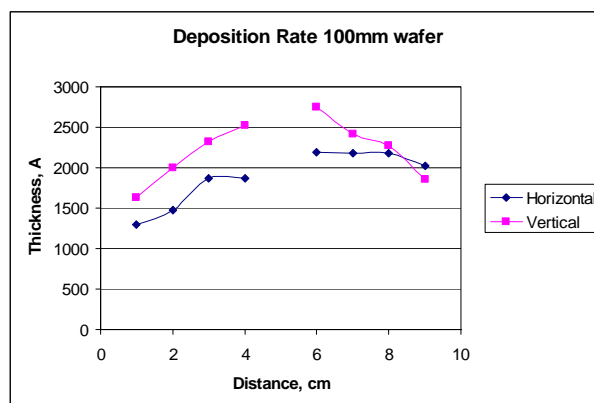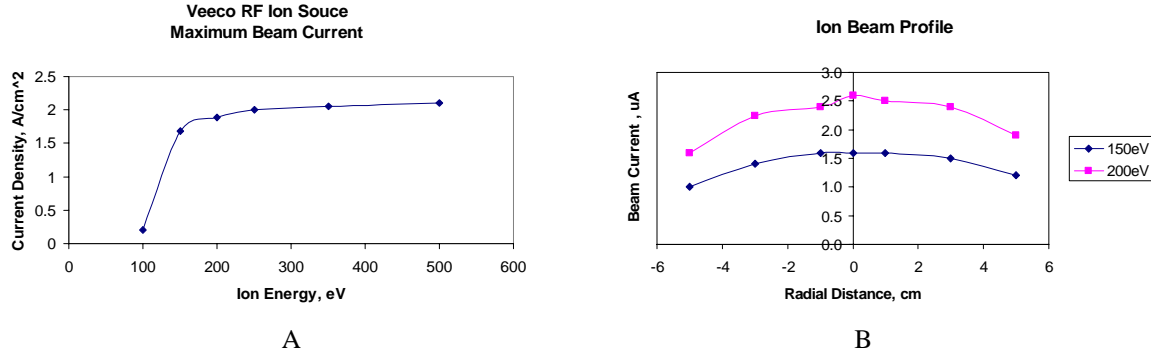

Figure 3.2-3. Deposition rate across 100mm wafer in the vertical and horizontal directions.

ranges and is shown below (Figure 3.2-4). The results indicate that the uniformity of the beam across the substrate area is uniform within several percent so that the beam will remain fixed rather than rastered across the substrate surface. The beam current must be

| A | B |

Figures 3.2-4 A and B. 4A: Maximum measured beam current from 3cm ion source as a function of beam energy, 4B: Measured ion beam profile of two beam energies across substrate region.

monitored closely however at low energy ranges as the maximum beam current shows. At low energies, it is very difficult to maintain beam stability and discharge conditions during long operation.

The data from the second ion beam, along with deposition rates from the first ion beam, will be used to determine the energy per atom at the surface during growth, which is a universal parameter for understanding the effects of ion bombardment on hard coatings [4,5]. The flux of ions, J, per atom, a, at the surface must be determined from the ion beam current and the deposition rate.

$$\frac{J}{a} = \frac{\text{ions/s cm}^2}{\text{atoms/s cm}^2}.$$

The energy, E, per atom is determined from the flux of ions at a particular energy, in this case the subscript, i, is used if more than one ion is present.

$$\frac{E}{a} = \sum_i E_i \times \frac{J_i}{a}.$$

The resulting universal parameter is easily transferable to most deposition environments, especially hard coatings where ion bombardment is a crucial element in film growth.

3.2.1 Depositional Methods and Parameter Characterization

Substrates most often used in the IBSD were 100mm Si wafers. These were for chemical composition and stress. Substrates for hardness testing were 1 in. square Ti_6Al_4V blanks. This is the material is used in fans and compressor blades for high performance aircraft.

Initial data on chemical composition was made using X-ray photoelectron spectroscopy (XPS) analysis of the sputter deposited thin films. Films were analyzed as received by subjecting the sample to ion bombardment until the adventitious carbon layer and native oxide layers were removed. The samples were again analyzed to determine the actual composition of the thin film with as little damage to this film as possible.

Stress measurements were also obtained using thin 200µm thick Si cut into one inch squares, labeled, and premeasured using a Flexus stress measurement tool. These films were then shipped to PSU and a two beam analysis of the curvature of the sample after deposition provided data to calculate the film stress. ITC has also measured residual film stress using profilometry as well as optically with the Flexus measurement system. The stress is determined from the change in the radius of curvature obtained from a flexible substrate after deposition

$$\sigma = \frac{E}{6(1-\nu)} \frac{t_s^2}{t_f} \left(\frac{1}{R} - \frac{1}{R_0} \right)$$

15

where σ is the residual stress, E is Young's modulus of the substrate, ν is Poisson's ratio, t_s and t_f are the thicknesses of the substrate and film respectively, and R and R_0 are the radii of curvature after and before deposition.

Constant monitoring and logging of deposition rates, gas flows, pressures, and ion beam parameters were also done to provide input into the energy deposition calculation. A Labview software package has been interfaced to the computer on the IBSD to log the data for each run when necessary. The power supplies that drive the ion beam are operated in constant current and constant voltage mode. Initial films were grown without the secondary ion beam in order to characterize the deposition and find the parameters necessary for high quality film growth. An RF ion source consists of a tuned inductor surrounding a quartz ionization chamber. The plasma then is extracted using a screen grid and an acceleration grid to accelerate the ions to the desired energy. A plasma beam neutralizer (PBN) sits near the ion beam exit to add electrons to the beam as it is accelerated. Very few of the ions are neutralized but the Coulomb beam spreading is greatly reduced. The ion beam parameters that must be followed are the emission current and beam energy. A 3cm ion source cannot produce much more than 50mA of beam current.

The system was baked at 120°C for several days to remove water from the chamber and to bring the base pressure down to ~1-3x10^{-9} Torr. A mixture of nitrogen and Kr were used to sputter the pure Ti and Si targets. Kr was chosen in order to remove any ambiguity that may arise from reflected neutral bombardment. However, the nitrogen will reflect with energies that are approximately 14% of the initial kinetic energy and reflects with an average energy per N atom of 120eV. Nitrogen concentrations varying from 25% to 100% in the Kr-N$_2$ gas mixture were examined. The films as measured by XPS showed that the concentrations were fairly stoichiometric in terms of Ti-Si-N and also included oxygen as a primary impurity. As the oxygen was reduced the nitrogen concentration increased bringing the concentration close to stoichiometry.

3.2.2 Deposited Film Characterization

Deposition began with deposition rate characterization from a Ti-Si target. The deposition is more sharply peaked for a 1200eV deposition than for 800eV as shown in Figure 3.2-5. The focusing efficiency of the ion source is greatly enhanced as a function of energy, which accounts for the peak in deposition rate [8]. The deposition rates were very low for the very hard materials.
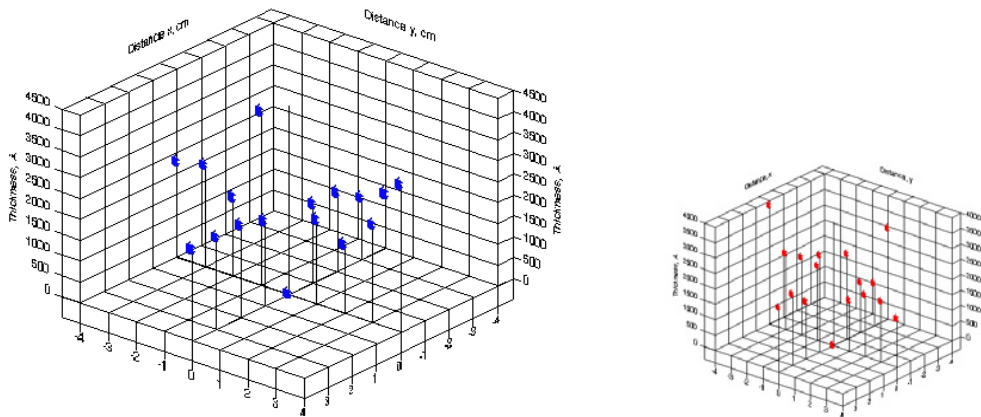
Figure 3.2-5. Deposition rates as a function of distance across a 100mm wafer from a Ti-Si target at 800eV (left) and 1200eV (right).

The deposition rate also varied as a function of gas composition. Figure 3.2-6 shows the reduction of rate as a function of increased nitrogen content in the Kr-N$_2$ mixture.

The most important data was the initial composition data. XPS analysis showed that the film concentrations were much to Si rich and much too high in oxygen concentration. Samples with high Si content (TiSiN with 40% Si)

Deposition Rate at 25mA Emission

Figure 3.2-6. Deposition rates as a function of nitrogen content and primary beam energy.

contained high concentrations of oxygen even when grown with a base pressure of 1×10^{-9} Torr. Figure 3.2-7 shows the compiled XPS concentration data as a function of deposition rate for with ~40% Si conten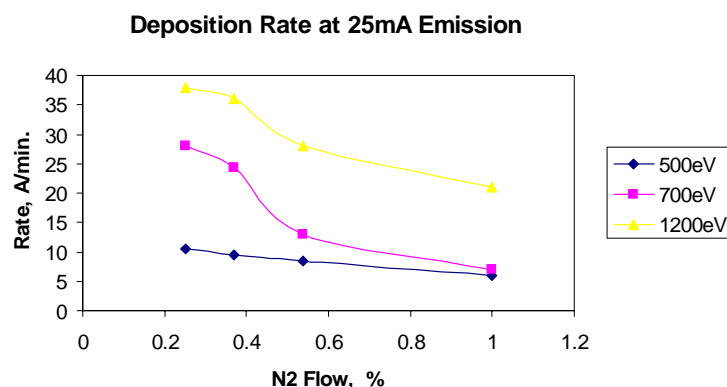t. The data shows that regardless of the quality of the vacuum, oxygen incorporation is still possible if the surface grows slowly enough.
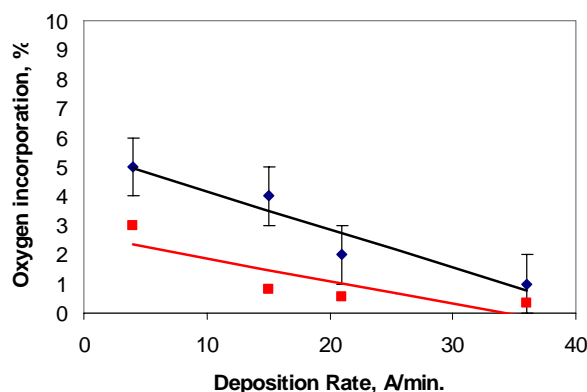

Figure 3.2-7. XPS oxygen concentrations, shown in blue with error bars, from TiSiN films deposited on Si substrates at room temperature. The deposition rate was varied from 4 – 36 Å/min. The red squares are model calculations of oxygen incorporation at ~4×10^{-9} Torr oxygen partial pressure assuming a unity sticking coefficient.

The hardness for these film compositions varied from 18-28GPa, as measured at PSU. Although the Si concentration was too high for superhard films, the hardness of this concentration was below what was in the literature. The oxygen concentration was believed to be the culprit.

While trying to remove the oxygen contamination from the films, another challenge arose in that high residual film stresses kept spalling thick films (~1.5 – 2μm) designed for hardness measurements. Films greater than 1.2μm thick would begin spalling at the edges of the sample. Films in the range of 1.2 – 1.6μm thick have a measured compressive residual stress of 3-4GPa, respectively. This stress was too high to maintain adhesion to the Si substrate. The stress increased as a function of ion beam energy and as a function of nitrogen content as shown in Figure 3.2-8A. Here the stress has been normalized to the thickness of the film. The increase as a function of nitrogen concentration in the working gas may reflect an increase in oxygen concentration in the films due to the lower sputter rate. However, the lowest sputter rates occur in low energy deposition, and this showed a decrease in the force per unit thickness. Also the force per unit thickness did not vary as much as a function of Si composition as shown in Figure 3.2-8B as it did as a function of nitrogen concentration. These films were all grown at 1200eV and a nitrogen concentration of 100%. There was a dip in the data in the Si composition range that is supposed to contain the superhard films, but we believe that may only be experimental error in obtaining the data. Still the results were confusing and merit further study.

17
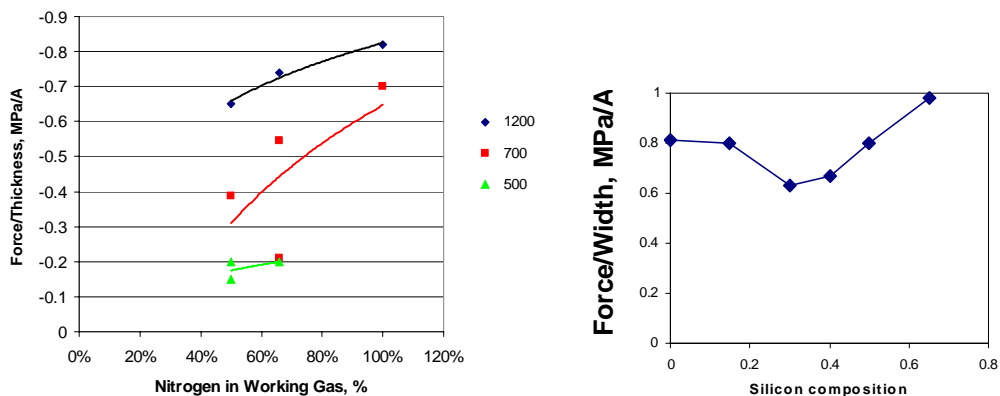
Figures 3.2-8A and B. Compressive residual film stress normalized to film thickness for TiSiN (40% Si) films as a function of ion beam energy and nitrogen concentration in the working gas. 8B. Compressive residual film stress normalized to film thickness for TiSiN grown at 1200eV in 100% N_2.

A solution to the film delamination was found by pre-stressing the substrate with an evaporated Cr film. A 2000Å Cr film had a tensile stress in the range of 1.2-1.5GPa. By adding a 2000Å Cr layer to the substrates, a 1.5 – 2μm film could be successfully grown on the Si substrates.

Pure TiN films were grown in an attempt to determine the best method of removing the oxygen during deposition. XPS data of pure TiN films were made at several N_2 – Kr working gas compositions. It was determined that for 25% N_2 in the gas mixture, the deposition rate was high while still providing good stoichiometry for the TiN films. A sample of the XPS spectra for 1200eV 25%N_2 TiN film is shown in Figure 3.2-9. The beam current for this deposition was 40mA. This spectrum was obtained after the sample was sputter etched for a period of time estimated to remove approximately 30-40Å of the surface with the goal of removing the adventitious carbon layer and native oxides. The result shows a 3% oxygen concentration in a film grown at room temperature.
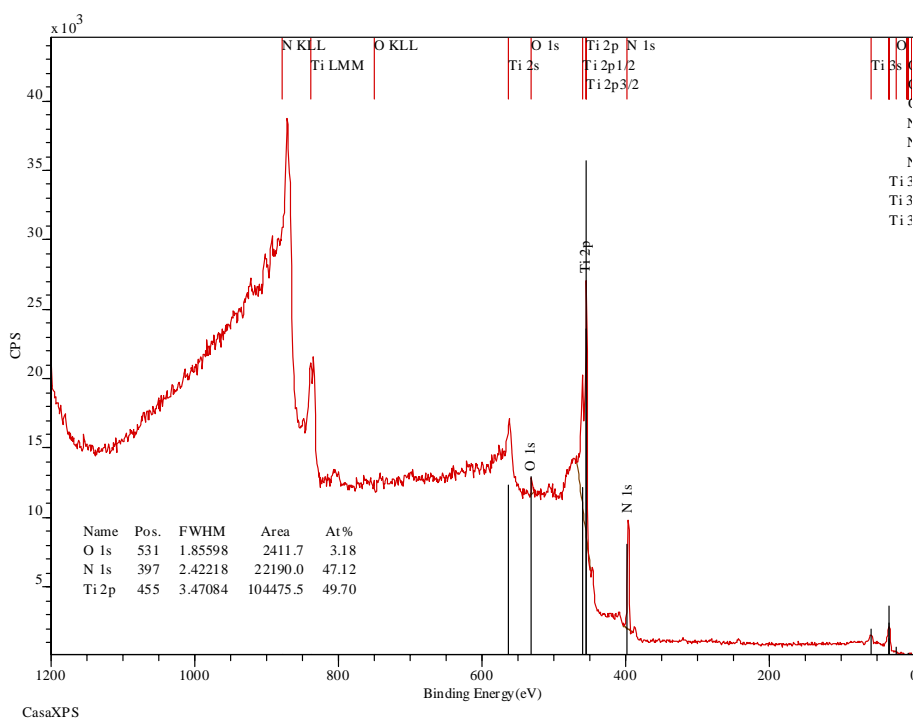

Figure 3.2-9. XPS spectrum of a TiN film grown at 1200eV and 40mA beam current. The working gas composition was 25% N_2 and 75% Kr. The oxygen concentration is calculated to be ~3%.

At 3% the oxygen peak is barely visible and marked as O 1s. A study was made at high beam currents and high deposition rates to determine the best parameters for deposition of pure TiN films without oxygen contamination. The results are shown in Figure 3.2-10.
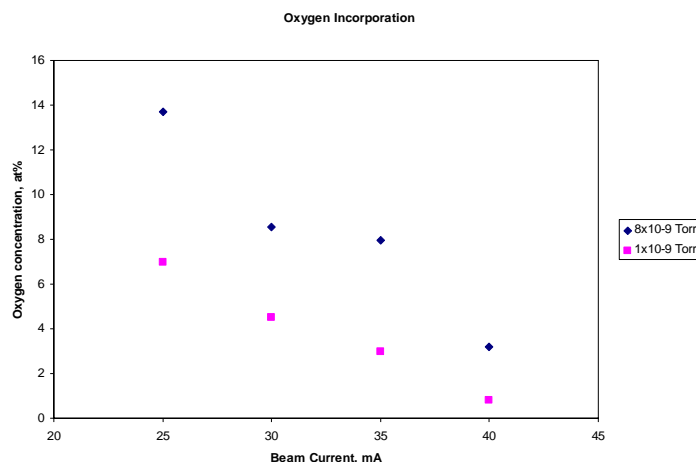
Oxygen Incorporation

Figure 3.2-10. Oxygen incorporation in TiN films as a function of ion beam current for two different base pressures.

For a normal $1x10^{-9}$ Torr base pressure it is possible to deposit films with a very low oxygen concentration. For a beam current of 50mA at 1200eV, the estimated oxygen concentration was 0.2% from XPS data. At very low concentrations XPS is not very quantitative. However, we have shown that the oxygen impurity concentration can be reduced if the deposition rate is high enough. At 50mA beam current, the source shorted the acceleration grid after 2 hours as a result of grid sputtering. The lifetime of the source will not be great at 50mA beam current.

3.3 Cathodic Arc Deposition

The cathodic arc system was proposed as an alternative deposition technique for this project. We began the project with only a cathode and a mass filter. At this time the system has been constructed and most of the components have been tested. The system itself is shown in Figure 3.3-1A. The system is cryo-pumped with turbo pump on board for use during deposition. The system was designed around a 45degree arc mass filter shown in Figure 3.3-1B. The rack to the left of the system holds the pump controllers and the ITC custom made pulse electronics, shown in Figure 3.3-2.

Figure 3.3-1A Cathodic arc deposition system.

Figure 3.3-1B. 45 degree mass filter.

Figure 3.3-2. Cathodic arc pulse electronic power supply.

The cathode uses a 1/4inch rod with alumina spacers. The sample substrate is a 100mm Si wafer attached to a rotating feedthrough. The feedthrough rod passes through a quartz lamp heater chamber which will heat the sample to ~500C. The feedthrough rod is ceramic to shield the feedthrough from the intense heat, and electrical contact is made on the back of the sample holder by graphite contacts. This allows sample biasing at 1-10kV at 125kHz during deposition, rotation for uniform deposition, and high temperature operation. The power supply emits a 5ms pulse with 200-600V and 400A of current. We have started with graphite rods for pulsing carbon arcs to test and evaluate the system. However, a two arc system with Titanium and Silicon arc rods and nitrogen base pressure should allow deposition of nano-composite materials. Composite Ti-Si cathodes have been used to make TiSiN by cathodic arc deposition [9]. However, no mention of multiple cathodes has been found for TiSiN films. The advantage here will be better control of stoichiometry and thicker films.

As time allows, we are attempting to run graphite arcs to determine the deposition characteristics of the system. This construction, especially the custom chamber and custom pulse electronics, were quite time consuming and limited the amount of time the system was available for testing.

3.4 Discussion

Superhard TiSiN coatings require high substrate growth temperatures to form the nanocrystalline structure, low oxygen concentrations, and low enough residual stress to maintain adhesion to the substrate surface. We now have the means to produce films with these qualities. The oxygen concentration has been reduced to levels of less than 0.5%. The IBSD system is capable of heating to $600^{o}C$, although until the oxygen was reduced there was no need to employ these temperatures. The residual stresses in the films have been mollified by the use of a pre-stressed Cr layer which will accommodate the high compressive film stress.

A simple model used for calculating the amount of oxygen incorporation (results shown in red in Figure 3.2-7) shows that for a base pressure of 4 x 10^{-9} Torr and assuming a unity sticking coefficients, a curve for oxygen incorporation could be obtained that closely parallels the experimental data. This curve mimics the one measured by XPS. An oxygen concentration of $4x10^{-9}$ Torr was the pressure that fit for our purposes. There seemed to be justification for this in that the system returned to a pressure in the range of $4-8x10^{-9}$ Torr ~1 hour after the deposition was complete and then moved slowly to the base pressure after another 10 hours. The use of a hot system might benefit this effort, as recommended by the program consultant Dr. Tucker. However, we have shown that low oxygen concentrations can be obtained for this system by using very high deposition rates.

The stress of the thin films was high, which is expected for most hard coatings. Cathodic arc deposition is attractive for the deposition of hard coatings by virtue of it's ability to produce films with good adhesion. However, the IBSD film stress was so high that it would be impractical for any turbine blade application which would require tens of microns of film thickness. Of the data obtained so far, the most interesting is the stress in the film as a function of primary-ion energy and N_2 – Kr mixture. If the oxygen concentration were the only consideration, then the worst stress would have occurred in the case of 500eV deposition, which had the highest oxygen concentration (15 – 25%). It seems more than likely that there are two influences in the residual film stress. The first is related to the ion bombardment that the deposited films experience and the second is the oxygen concentration. The films were grown without the use of the second ion source so that the only bombardment that the films experienced was from the

neutral nitrogen atoms reflected from the target. These species have average energies of 120eV, although they are only a small percentage of the events at the target (~14% of the incident beam). We continue to see interesting areas for study in reflected neutral bombardment, which occurs continuously in every sputter deposition system (see for example ref. 1). Modeling the effects of reflected neutral bombardment is accomplished using Monte Carlo simulations, such as TRIM, to determine the flux and energy of reflected neutrals. Results of reflected neutral modeling have shown that depositions conducted using a 1200eV primary ion beam can give an additional 35eV/atom at high nitrogen concentrations. Sputtered atoms have an energy of at least 5eV/atom as a result of the ejection process. The additional bombardment can be beneficial but could also be part of the reason for the change of stress of the film along with the oxygen contamination.

3.5 Conclusions and Recommendations

Our conclusion is that the nanocomposite coatings should have been grown using a 12cm ion source. This would have been considerably simpler if we could have had a 12cm RF ion beam which is capable of much higher sputter deposition rates. At the deposition rates we can reach with the existing equipment, it would take 8 hours to grow a single film 2µm thick. Although the problems of driving a system built for the deposition of films 1 – 10nm thick are great, we now have control over the film growth conditions necessary to grow hard coatings.

An ultra-high vacuum ion beam sputter deposition method that allows one to control the energy or momentum per atom arriving at the surface of a growing film is an excellent tool that allows one to independently analyze the deposition parameters that are not independently controllable for any other deposition technique. To date there has not been a similar analysis published in the open literature.

References Cited
[1] Lannon, J.M.; Pace, C.C.; Temple, D.; McGuire, G.E.; Hebard, A.F.; Ray, M.; "Ion Beam Deposited GMR Materials", Spintronics Symposium (Materials Research Society Symposium Proceedings Vol.690), 2002, p 157-62.

[2] Spaeth, C.; Kreissig, U.; Richter, F.; "Sputtering and chemical erosion during CN/sub x/ synthesis by ion beam assisted filtered cathodic arc evaporation", *Thin Solid Films*, v 355-356, Nov. 1999, p 64-72.

[3] Kutsay, O. ; Bello, I.; Lifshitz, Y.; Lam, C.W.; Luk, W.Y.; Lee, S.T.; Meng, X.; Kremnican, V.; "Nanostructuring of tetrahedral carbon films by carbon ion implantation", *Diamond and Related Materials*, v 12, n 10-11, Oct.-Nov. 2003, p 2051-6.

[4] Adibi, F.; Petrov, I.; Greene, J.E.; Hultman, L.; Sundgren, J.E.; "Effects of high-flux low-energy (20-100 eV) ion irradiation during deposition on the microstructure and preferred orientation of Ti/sub 0.5/Al/sub 0.5/N alloys grown by ultra-high-vacuum reactive magnetron sputtering", *Journal of Applied Physics*, v 73, n 12, 15 June 1993, p 8580-9.

[5] Kester, D.J.; Messier, R.; "Phase control of cubic boron nitride thin films", *Journal of Applied Physics*, v 72, n 2, 15 July 1992, p 504-13.

[6] Superhard nanocomposite Ti-Si-N coatings Vaz, F. (Phys. Dept., Univ. of Minho, Azurem, Portugal); Rebouta, L. Source: *Materials Science Forum*, v 383, 2001, p 143-9.

[7] Prochazka, Jan; Karvankova, Pavla; Veprek-Heijman, Maritza G.J.; Veprek, Stan; "Conditions required for achieving superhardness of greater than or equal 45 GPa in nc-TiN/a-Si$_3$N$_4$ nanocomposites"; *Materials Science and Engineering A*, v 384, n 1-2, Oct 25, 2004, p 102-116.

[8] Ray, M.A.; Barnett, S.A.; Greene, J.E.; "A multiaperture ion source with adjustable optics to provide well-collimated, high-current-density, low- to medium-energy ion beams", *Journal of Vacuum Science & Technology A (Vacuum, Surfaces, and Films)*, v 7, n 2, March-April 1989, p 125-31.

[9] Rother, B.; Mucha, A.; "Effects of plasma ion implantation from cathodic arc plasmas", *Surface & Coatings Technology*, v 142-144, July 2001, p 402-5.

4.0 NPC PROGRAM AT NORTH DAKOTA STATE UNIVERSITY

4.1 Introduction

The objective of the initial phase of the NPC program at NDSU was to establish at its new Center for Nanoscale Science and Engineering the capabilities for deposition, characterization, and optimization of nanostructured protective coatings, and to contribute to the research collaboration. NDSU would: (1) develop appropriate tribology characterization and testing of superhard coating samples prepared by Penn State and ITC; and, (2) transfer Nanostructured Protective Coatings deposition methodologies from Penn State (and ITC as applicable) to NDSU. Because the new facility (Research 2) became fully operational only in the summer of 2004, the bulk of NDSU's work was done during the last 15 months of the two-year program.

4.1.1 Tribology

Tribology might be defined as the study of the wear of materials. In practice, tribological characterizations give an indication of how a material degrades under the influence of external forces. These external stresses induce strain fatigue with subsequent formation of cracks. Cracking in coatings leads to materials failure observed physically as spallation or mechanically by a loss of performance (e.g., increased friction coefficient). Comparison of coating composition and microstructure with tribology characterizations offers the possibility of optimizing deposition/growth parameters in order to enhance coating performance – this is the goal of this portion of the project.

There are a number of tribology tests that are available to determine the wear of materials. As a first step in this project, a report compiling all pertinent tribology tests was produced to illustrate the options that might be considered when developing NDSU characterization facilities at CNSE. This report, entitled "Survey on Methods for Testing and Evaluation of Wear Resistant Coatings", is attached to this document as Appendix B. The next step in this project was to determine which of the numerous characterizations might be assembled at NDSU. As tribology is the study of the wear of materials, it would seem imperative that the facilities developed at NDSU match the wear of the materials in the field. In other words, a selection of the application needs to lead a selection of tribology tests. For this, we contacted our partners in the AFRL. The following list of applications was defined during an on-site visit to the AFRL labs in Dayton, OH as those that may be applicable to the needs of the U.S. Air Force:

- High-speed/high-temperature bearings
- Compressor's blades
- Substitutes for lubricant-free friction systems
- Tooling for metal, polymer, and composite materials manufacturing.

Follow-on discussion with Dr. Andrew Voevodin, Senior Materials Engineer, further confirmed Air Force interest in coatings that could applied to the following substrates: Ti6Al4V alloy (aka Ti-6Al-4V; $Ti_{0.90}Al_{0.06}V_{0.04}$) for compressor blades in jet engines; Inconel-based alloys for high-temperature roller bearings; and M50 or 440C bearings that are wetted with perfluorinated hydrocarbon-based lubricants. This information was discussed with program consultant Dr. Robert Tucker and the following tests were strongly suggested for deployment in the NDSU tribological characterization facility:

1. Residual stress testing (for both types of alloys);
2. Sand abrasion for erosive wear test (Ti-based alloys only); and,
3. Roller fatigue and oxidation resistance testing (Inconel alloys only).

Given the limited capital equipment budget ($50,000), it was decided that NDSU would develop a Gas Jet Erosion Test Facility for testing coatings on Ti6Al4V alloy substrates. Additionally, NDSU procured an Almen strip tester for measuring residual stress in coatings. As a part of a related project, a Hysitron TriboIndenter was undergoing qualification when the program ended.

4.1.2 Deposition Methodologies

Superhard materials in the form of coatings have a great potential for a number of applications. Over the last few years, a relationship between superhardness and nanostructured coatings has been demonstrated which has led to intensive research for bettering the understanding of this relation and for developing proper procedures for their synthesis. The hardness of a material is dependent on both the interatomic bonds, as well as its crystal lattice

structure. It is possible to achieve very high hardness, even up to 80 GPa by forming an optimal nanostructure in materials that have a much lower hardness in their coarse grained state. Nanocrystalline-Amorphous composite coatings which consist of nanocrystals of hard materials embedded into an amorphous matrix of relatively softer materials have shown great potential for achieving superhardness. The hardness of these coatings is much greater than the hardness of each phase taken separately. Veprek et al. [3] have shown that a nanocomposite material of TiN nanocrystals in an amorphous Si_3N_4 matrix is capable of reaching very high hardness of 50 GPa and elastic modulus of >500 GPa. The enhanced hardness of the nanocrystalline/amorphous composite is due to the inability of the dislocations to propagate through the sharp boundaries in the matrix. In order to ensure formation of sharp boundaries and to prevent interdiffusion, the preparation of the material should be done at low temperatures. This constraint led Veprek et al. [3] to choose Plasma enhanced Chemical Vapor Deposition as the most promising technique. In addition PECVD also provides the ability to adjust the crystallite size, and also the induced stress by providing a means to control the ion bombardment.

4.2 Methods and Procedures

Methods and procedures for both characterization of materials and deposition of thin film materials are now given.

4.2.1 Tribological Testing of NPC Materials

Given the scope of the application for this project (i.e., coatings for jet engine fan and compressor blades) and with consideration of the capital equipment budget for this project, three different characterization facilities were procured/developed with support from this project. An Almen strip tester was purchased to test for residual stress in thin films. A nanoindenter was procured (in a related program) in order to test the mechanical properties of the films. A gas jet erosion testing apparatus was designed and built in order to test the resistance of films produced at Penn State and ITC towards particle erosion. Each of these three systems is now described below.

4.2.1.1 Almen Strip Tester

The #2 Almen gage is a precision device used for used for measuring the deflection of a special 'Almen' metal test strip. The gage is fitted with a high accuracy digital indicator that is capable of measuring the stress induced curvature termed as "arc height" of the metal strip. This method is commonly employed in the shot peening industry to measure the stress developed in a peened part. To measure the residual stress induced in a metal strip, the change in radius of curvature of a substrate before and after it is coated is measured. Once the radius of curvature is determined, the strain in the specimen is calculated using Stoney's equation (eq. 1) [1] where, $1/E(1-v)$ is the biaxial modulus of the substrate, t_s is the thickness of the substrate, t_f is the thickness of the film, and R_0 is the inherent curvature in the uncoated substrate.

$$\sigma = \frac{1}{6E(1-v)} \frac{t_s^2}{t_f} \left(\frac{1}{R} - \frac{1}{R_0} \right) \tag{1}$$

The usual practice involves coating a single side of the Almen strip which is a thin strip of cold rolled spring steel and determining the radius of curvature induced by the applied coating. When a metal strip is coated, residual stresses are set up due to the difference in thermal expansions of the coating and substrate. This mismatch at the interface causes the specimen to bend either upwards or downwards, depending upon the type of stress induced. The residual stress induced by the coating is then determined indirectly using Stoney's equation [1] by measuring the deflection induced by the stress.

Figure 4.2-1. Picture of Almen gage at NDSU.

4.2.1.2   Nanoindenter

Nanoindentation is one of the most commonly used techniques for determining the mechanical properties of materials especially coatings. In this method, an indenter tip of known geometry is driven into the test material with increasing normal load. The load and displacement of the indenter are continuously recorded during the indentation process and this data is graphed to obtain a load – displacement curve of the test material. Established models are then used to obtain hardness, modulus and other mechanical properties from the load – displacement curve.

As a part of a related project, NDSU procured and was in the process of qualifying a Hysitron TriboIndenter® when the program ended.

4.2.1.3   Gas Jet Erosion Test (GJET)

The GJET system is a device that uses pressurized air to carry erodent particles through a nozzle to make them impinge on the test specimen. The test specimen is exposed to the erodent air stream for a period of time and the mass loss suffered by the test specimen is determined which is a measure of its erosion resistance. While there is an ASTM standard for testing erosion resistance of bulk materials (i.e., ATSM G-76), the method requires modification to be amenable to thin coatings such as those developed in this project. Two iterations were required in order to provide an accurate method of measuring fluid flow (i.e., double disc velocimeters #1 and #2) and two iterations were also required for the GJET system. Results of these studies are now presented.

4.2.1.3.1 Double Disc Velocimeter Version #1

Accurate measurement of abrasive impact velocity is very important for meaningful characterization of erosive loss in materials. A comparison of the various velocity measurement systems is given in Table 4.2-1. Given the costs associated with more sophisticated systems, a double disk velocimeter was selected for use. The design utilized by CNSE was previously reported by Ruff and Ives [2]. The velocimeter consists of two circular discs of diameter 60mm mounted on a common motor shaft. The outer disc has a slit cut into to allow abrasives to pass through it and strike the surface of the second disc. To measure the velocity of the abrasives, the double disc arrangement is positioned such that the slit on the first disc is inline with the blasting nozzle. As a first step, the abrasives are made to impinge against the discs while they are stationary with adequate exposure time to allow the formation of a visible scar on the second disc. In the next step, the abrasives are made to impinge against the discs while the discs are rotated at a constant velocity. The abrasives passing through the slit in the first disc get deflected and make a scar on the second disc at a distance away from the initial scar which is proportional to their velocity. The velocity of the abrasives are thereby estimated by measuring the distance between the two scars present on the disc,

Table 4.2-1. Comparison of Particle Velocimetry Systems.

	Laser Doppler Technique	Particle Image Technique	Optoelectronic Technique	Double Disc Technique
Measurement	Non-invasive	Non-invasive	Non-invasive	Invasive
Sampling volume size	Small	Large	Small	Small
Particle size	1μm – 1mm	0.2μm – 40μm	>70μm	N/A
Accuracy	0.1%	High	Medium	10%
Price – New	~ $100,000	~ $100,000	N/A	N/A
Price – Used	~ $50,000	~ $50,000	N/A	N/A
Price – Rent/Lease	N/A	N/A	N/A	N/A

N/A = Not Available

The first version of the CNSE double disk velocimeter used a 2000 rpm ac synchronous motor connected to a 2:1 gearbox to rotate two 40 mm diameter disks at 4000 rpm. This value was confirmed with an optical stroboscope. The upper end of velocity measurement for the DDV system is limited by the ability to deconvolute the two wear scars on the second disk. Evaluation of this phenomenon showed the CNSE double disc velocimeter was limited to particle velocities of 130 m/sec or less.
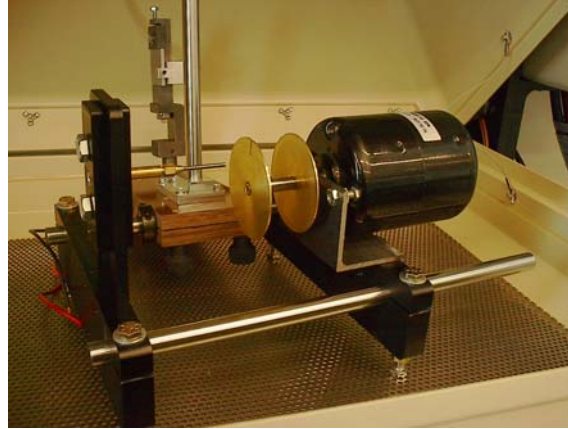
Figure 4.2-2. Picture of Double Disc Velocimeter – Initial Version.

4.2.1.3.2 Double Disc Velocimeter Version #2

Since the long term objective of the project is to set up a service center facility to allow erosive wear testing of a range of coatings, it was necessary to improve the measuring capabilities of the existing DDV set up. Towards this end, the NDSU DDV was revamped to provide resolution of velocities up to 600 m/s ($\pm$3.5% accuracy). The new DDV includes 10" diameter disks that can be rotated at speeds of up to 4500 rpm ($\pm$0.1%). Characterization of the system was realized using 10 and 50 μm Al_2O_3 erodent particles with the results of this study presented in the plots below.
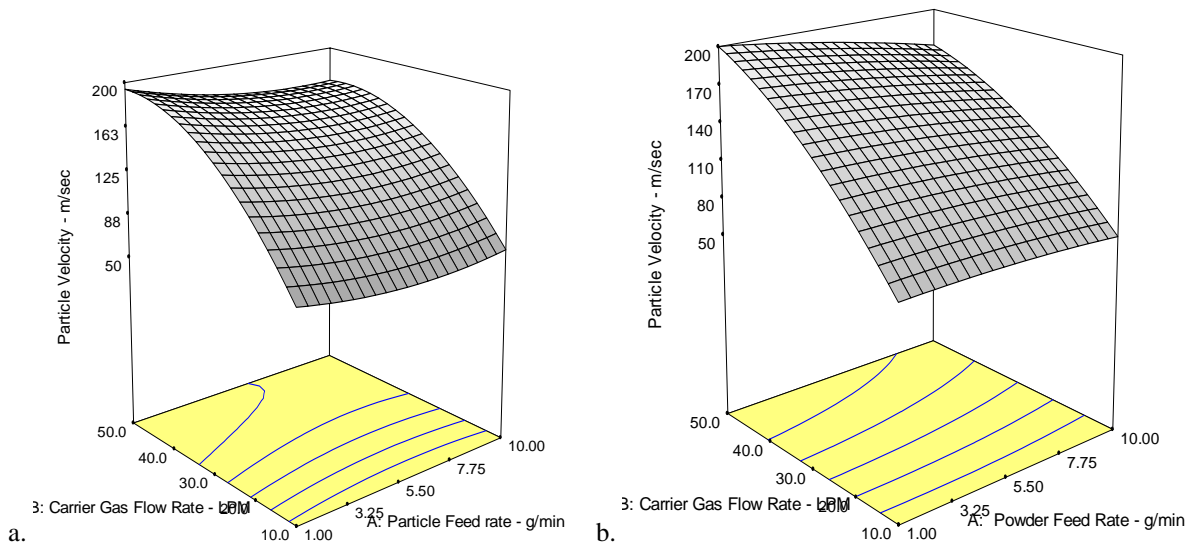

Figure 4.2-3. Erodent velocity vs. carrier gas flow rate/feed rate relationship for (a) 10μm and (b) 50μm Al_2O_3.

4.2.1.3.3 Gas Jet Erosion Tester Version #1

In an effort to establish a GJET facility at NDSU, various vendors were contacted to purchase a new commercially available GJET system. It was determined that available systems were too intensive to test thin coatings, and that modifications to the system would lead to a price exceeding $40,000. This was not an effective solution, as the total capital equipment budget for this project was $50,000. Attempts to locate a G76 system in used condition were unsuccessful. At that point, CNSE made contact with Bud Labs who offered to build a custom GJET system with the

Figure 4.2-4. Picture of Double Disc Velocimeter – Final Version.

following specifications: (1) a Tungsten Carbide (WC) micro abrasive blasting nozzle from Comco Inc. with an inner diameter of 1.5 ± 0.07mm and 50mm length; (2) a sample holder capable of varying the angle between the nozzle and specimen from 15° – 90° in steps of 15° while maintaining a stand off distance of 10 ± 1mm; and, (3) a used Jet Kote HVAF fluidized bed type powder feeder system. The sample holder and nozzle assembly is housed in a Micro-jet 200 blast cabinet with the powder feeder located adjacent to this arrangement.

Figure 4.2-5. Gas Jet Erosion Tester – Initial Version

After procurement of the GJET system was complete, calibration of the system was carried out before performing any actual characterization of the erosion resistant coatings. Calibration involves establishing the feed rate of the powder feeder at different line pressures, estimating the diameter of the wear scar at different pressures, and stand off distances, etc. For this purpose of calibration, an uncoated M-2 steel substrate was utilized as there is no concern of penetration depth and corresponding change in erosion resistance in case of bulk materials. The results of the calibration tests revealed the following problems:

1. The powder feeder was not capable of providing repeatable feeding rates due to the nature of its construction. Intermittent pulsed feeding was also observed when 10µm Aluminum Oxide powder was used as erodent. This made the existing system unsuitable for reliable wear testing.
2. The existing system used pressure differential to control the carrier gas velocity which in turn controls the erodent velocity. This method did not provide accurate means to vary the erodent velocity and also resulted in poor reproducibility of the test results.

26

The above mentioned reasons prevented the use of the current system for reliable characterization of the erosion resistance of the coatings.

4.2.1.3.4 Gas Jet Erosion Tester Version #2

In an effort to establish a controllable, reproducible erosion test protocol, procuring new components and redesigning the GJET system was required. In particular, issues related to the following were addressed:
1. Screw-type powder feeder to give accurate powder feed rates; and,
2. Flow control meters for accurate control of the carrier gas velocity.

A collage of components of the redesigned NDSU GJET system is shown in Figure 4.2-6.

The new GJET system features a Powder Feed Dynamic's Mark XV precision powder feeder that has a unique construction which allows it to overcome the shortcomings inherent to most other powder feeders: pulsation, erratic powder feed and poor repeatability and reproducibility of feed rate. The powder is stored in a vibratory hopper from which it is fed into a metering screw by means of a vibratory drive which prevents powder from segregating due to particle size and also facilitates easy metering by the feed screw. The powder is then carried by a pressurized gas stream through two cyclonic mixers which ensure proper fluidization of the particles to prevent pulsing and irregular feeding of the powder.

The feeder has the capability to vary the rotational speed of the metering screw to vary the feed rate and is also capable of using different sized screws to allow use of larger particles and also for obtaining larger feed rates. (Figure 4.2-7).

The NDSU GJET has the following features:
- Particle kinetic energies from 9.3e-10 to 0.0049 J/particle.
- 10" DDV to measure wide range of particle velocities (30 – 600 m/s)
- Flow meters to accurately control carrier gas velocity (30-850 m/sec)
- Powder feeder with interchangeable screws to feed different particle sizes (10 – 270um APS) and to obtain different feed rates (0.5 – 20 g/min)
- Indexed sample holder to study erosion at different incident angles (0 – 90 degrees).

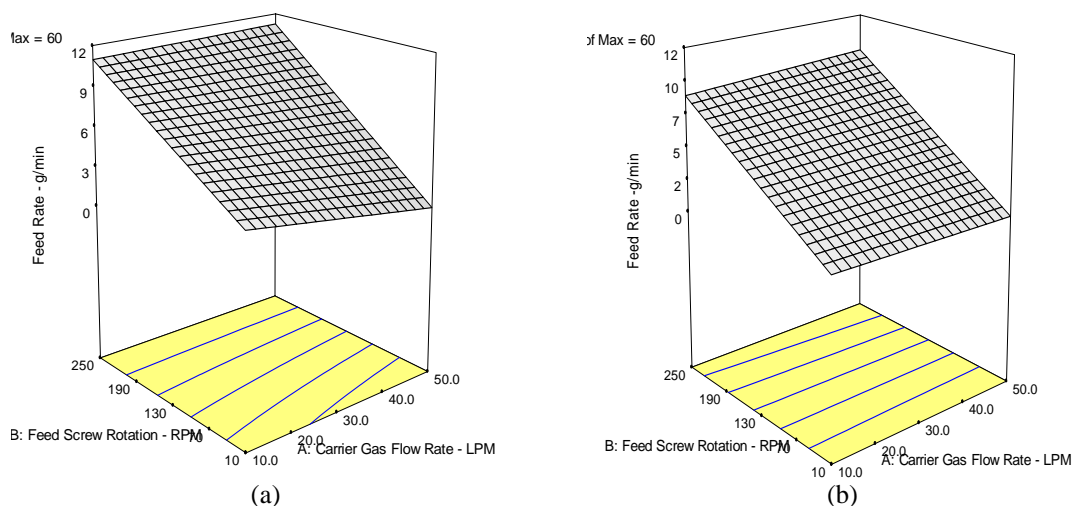Figure 4.2-6. Gas Jet Erosion Tester – Final Version

Figure 4.2-7. Feed rate vs rpm/flow rate relationship for (a) 10 μm and (b) 50 μm Al_2O_3 erodents

4.2.2 Deposition Methods Development

The goal of the Nanostructured Protective Coatings (NPC) program was to develop a fundamental understanding of the materials, deposition parameters, and resultant nanostructures that will lead to new superhard nanostructured protective coatings that meet military needs.

NDSU procured a magnetron sputtering system and a Plasma Enhanced Chemical Vapor Deposition system, both as parts of other programs, which will enable new programs in the synthesis of superhard nanostructured coatings.

4.2.2.1 Magnetron Sputtering System

Sputtering is the most commonly used technique for deposition of nanostructured coatings. In a magnetron sputtering system, ions are used to bombard the surface of the target materials. The impact of the ions causes sputtering of the target material which then deposit on the substrate placed in the chamber. A magnetron sputtering system can be used in different configurations such as direct current sputtering, alternating current sputtering, radio frequency sputtering, etc.

NDSU has procured and installed a Kurt Lesker CMS-18 thin film deposition system (Figure 4.2-8) that has the following configuration and capabilities: DC / RF / pulsed DC capable; three (3) Torus® magnetron sputtering targets; DC (x2) and RF (x1) power supplies; rotating platen allowing speeds of up to 40 rpm of 6 inch or smaller substrates; RF substrate biasing; heating substrates for up to 800°C; glancing angle deposition; in-situ thickness monitoring; spectroscopic ellipsometry upgradeable; load-lock with cassette indexer; compositional spread upgradeable for combinatorial growth techniques.

4.2.2.2 Plasma Enhanced Chemical Vapor Deposition System

Another frequently used technique for developing NPC is PECVD which uses plasma to accelerate the CVD reaction. The major advantage of a PECVD system is that it allows deposition at much lower temperatures than a conventional CVD process since the plasma produces chemically very reactive ions and radicals. NDSU has received an Oxford Instrument's PlasmaLab System 100 PECVD system (Figure 4.2-9), and was in the process of installing and qualifying this system at the end of the period of performance.

Figure 4.2-8. Kurt Lesker CMS-18 Thin Film Deposition System

Figure 4.2-9. Oxford Instruments PlasmaLab System 100 PECVD system

4.3 Results and Discussion

4.3.1 Gas Jet Erosion Test

The erosive wear resistance of a sample is characterized by determining the mass loss suffered by it after being exposed to a known quantity of erodents. The mass loss suffered by the sample is typically determined by weighing the sample before and after exposing it to the erodent stream. In case of NPC, the samples are coatings with thickness in the range of 2-5µm, which corresponds to expected mass loss around 0.3mg. Since a typical analytical balance in the laboratory has a resolution of ±0.15mg, it limits the use of the gravimetric method for accurate determination of wear loss.

An alternative solution is the use of profilometry to determine the volume loss. Two types of profilometers are available at NDSU and were tested for applicability to this research project. A VEECO Wyko 3300 optical profiler was first used to measure the wear scar volume loss but the control system was RAM memory-limited and the entire wear scar could not be mapped. Some results of smaller scars also showed features that were inconsistent with expected results. The manufacturer observed the same limitations for NDSU samples that were shipped to the

manufacturer and analyzed on-site at VEECO. While there is a literature report that suggest the applicability of the optical profilometry to determine erosive wear loss, such analysis requires "stitching" of the data and profiling the entire wear scar which is not reported. Since both the gravimetric method and the optical profiler could not be used, NDSU will be using a stylus type KLA-Tencor P11 long scan profiler for obtaining the wear loss. The 2D profile of the wear scar is obtained using the contact profiler and a curve is fit to the data using MS Excel to obtain a representative mathematical function. The volume of the wear scar is equal to the volume obtained by rotating about a vertical axis, the region under the curve which can be determined by way of triple integration. The volume loss is converted to wt. loss (via density) to give the erosion rate as follows and an example curve is shown in Figure 4.3-1 (see below) with initial results obtained by this method given below.
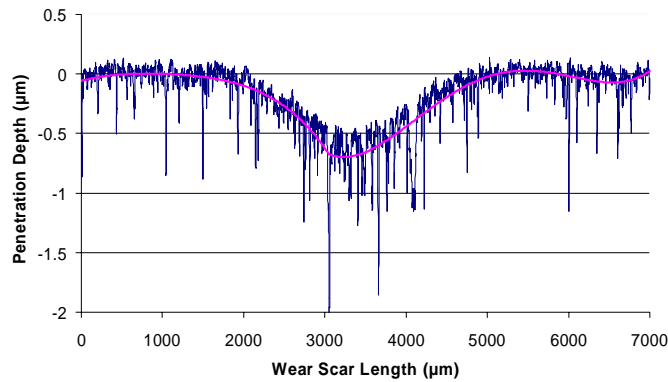

Figure 4.3-1. Profile data of a wear scar obtained using the Tencor P-11.

The samples used in the initial GJET characterizations were TiN coated M-2 tool steel. The samples were prepared by providing Goldstar Coatings Inc. with prepolished (R_a = 4 μin) M-2 tool steel samples 30x30 mm^2 in area. The appropriate erosion conditions were first determined iteratively using a sacrificial sample. The graphs shown below (Figure 4.3-2) show
the results from testing TiN samples with the following test conditions: erodent – Al_2O_3 (10 μm A.P.S.); feed rate = 1.5

a.

b.
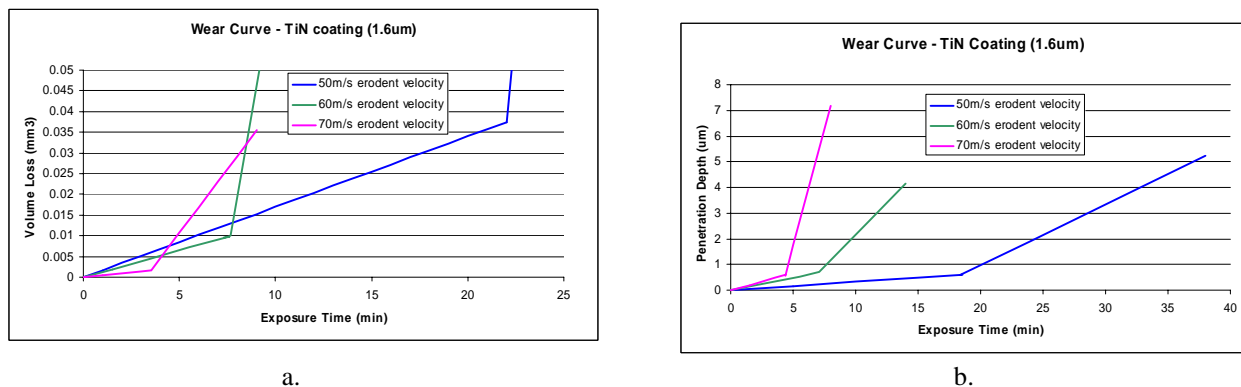
Figure 4.3-2. Wear data for a TiN/M-2 steel sample in terms of (a) volume loss (mm^3), and (b) penetration depth (μm).

g/min; erodent velocity = 50, 60, 70 m/s; impingement angle = 90º; and, nozzle-to-specimen distance = 43 mm. Figure 4.3-3 below is a photograph of one TiN/M-2 sample after this GJET testing.
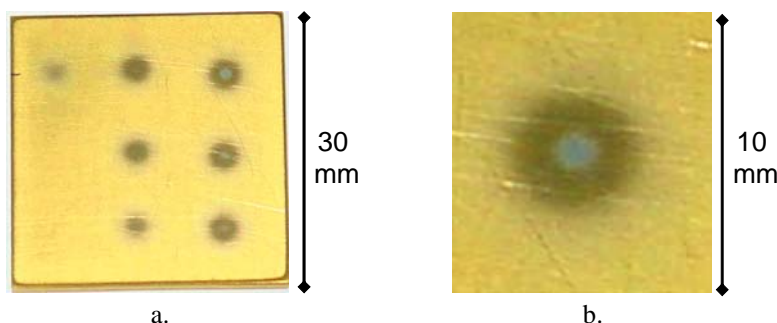
Figure 4.3-3. Photographs of the TiN-coated sample after GJET showing (a) the entire substrate, and (b) a single wear scar.

4.3.2 NDSU Sputtered Films

4.3.2.1 Deposition Procedure

In June 2005 Penn State's Paul Sunal visited NDSU CNSE and instructed CNSE personnel in their methodology for deposition of TiN and Ti-Si-N nanocomposite films on Silicon wafers and Ti6Al4V substrates, using the KJLC CMS-18 thin film deposition system. The experimental procedure is explained below.

The substrates (Si wafers and Ti6Al4V) were first thoroughly cleaned and dried before insertion into the deposition chamber. The substrates were heated to a temperature of 550°C and etched using Ar gas. The Ti and Si targets were then presputtered for 3 min using Ar at 100 sccm. Substrate rotation was engaged and prior to deposition of the Ti-Si-N films, a pure Ti adhesion layer was deposited to improve the adhesion of the film. The target power was set to 600 W for Ti and 100 W for Si and N_2 gas was introduced at 100 sccm. The substrate bias was set to 50 W and deposition was carried out at a temperature of 550°C, which as shown by Veprek [3] is the temperature at which TiN forms perfect nanocrystals and Si-N is in an amorphous state. A summary of all the main deposition parameter is given in Table 4.3-1.

Table 4.3-1. Deposition parameters employed during Ti-Si-N nanocomposite synthesis.

Chamber pressure	10mTorr
Gas flow rate (Nitrogen)	100 sccm
Substrate bias	50 W
Target power	600 W (Ti) 100 W (Si)
Temperature	550°C
Substrate rotation	20 rpm

After deposition, the Ti-Si-N film was subject to a number of characterization tests, the details of which are provided in the following sections.

4.3.2.2 SEM Analysis

The Ti-Si-N films prepared at NDSU were cross sectioned and examined under a SEM at Penn State to study their microstructure. Figures 4.3-4 (a) and (b) illustrate the microstructure of the films at 50X and 100X magnification. The SEM showed a columnar type structure for these films.

4.3.2.3 X-Ray Diffraction Analysis

An XRD analysis of the deposited films was carried out at NDSU using a new Bruker instrument in order to determine the composition and phase structure of the materials. The XRD pattern of Ti-Si-N films deposited on Ti6Al4V is shown in Figure 4.3-5. The results show that the NDSU Ti-Si-N coatings have a (200) preferred orientation, as was the case with the Penn State coatings. Only TiN phases were detected and the peaks are shallow and wide which indicate that TiN is in the nanocrystalline form, and SiN_x is amorphous. The XRD analysis was

carried out for Ti-Si-N films deposited at two different temperatures: 450°C and 550°C (insert in Figure 4.3-5). The XRD pattern of both these Ti-Si-N films was found to be very similar which indicated that there was not much effect of temperature.
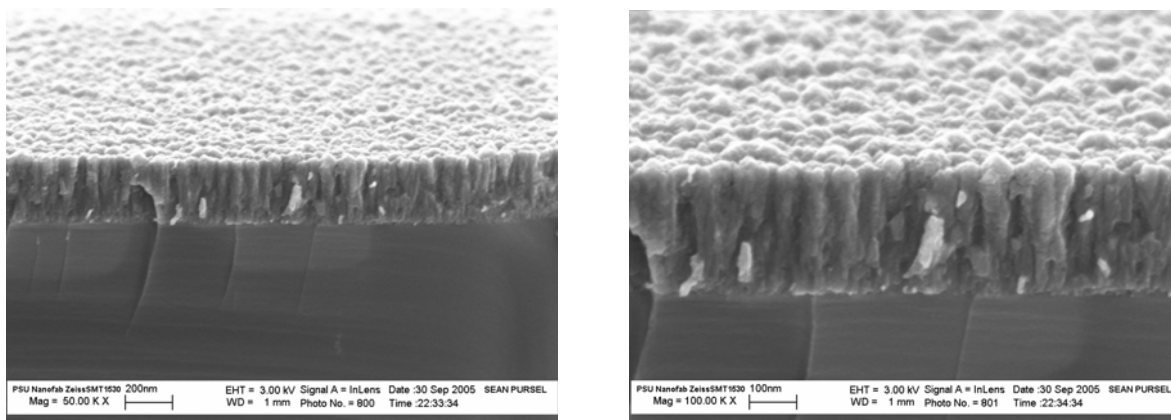
(a)

(b)

Figure 4.3-4. Micrographs (SEM) of cross sections of Ti-Si-N nanocomposite film deposited at 550°C at (a) 50X, (b) 100X. (Characterization performed by Penn State.)
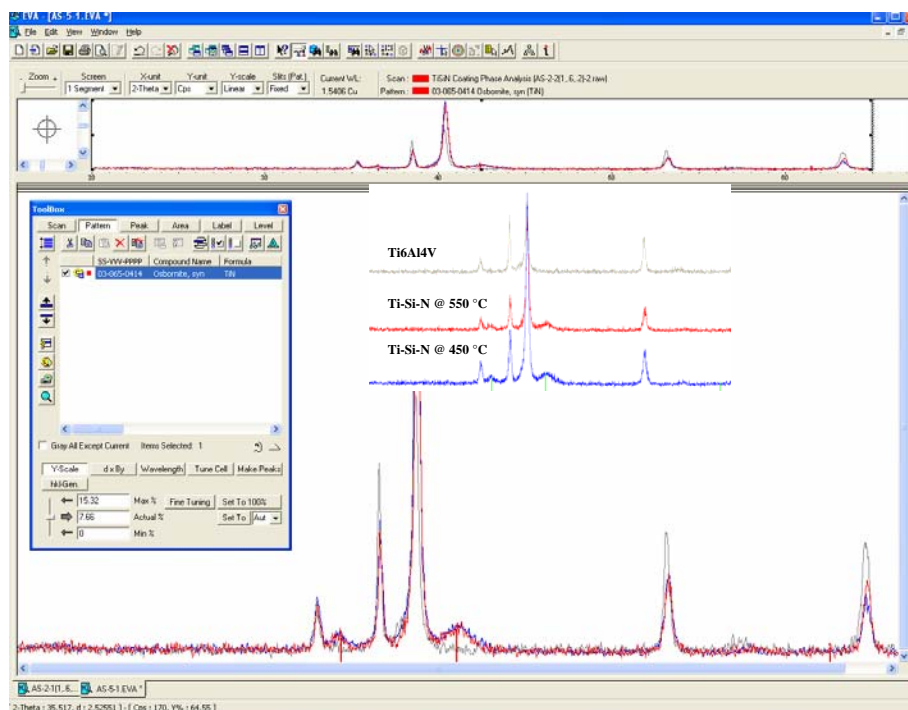

Figure 4.3-5. X-Ray diffraction pattern of Ti-Si-N films deposited on Ti6Al4V substrates at 450°C and 550°C.

4.4 Conclusions and Recommendations

The objective of the initial phase of the NPC program at NDSU was to establish at its new Center for Nanoscale Science and Engineering the capabilities for deposition, characterization, and optimization of nanostructured

protective coatings, and to contribute to the research collaboration. NDSU now possesses both sputtering and PECVD capabilities that can be used in the development of high performance coatings in the future. In addition, NDSU also has the capability to characterize the coatings for erosion/wear resistance, and will soon have the capability to characterize mechanical properties on the nanoscale.

References Cited

[1] Cremonaa M, Gazolaa L.M, Scavarda do Carmoa L.C, Castrob J.T.P, Achetec C.A, "In situ hard coatings strain measurement using a commercial strain-gage device," *Thin Solid Films* 377-378 (2000) 436-440.

[2] Ruff, A.W., and Ives, L.K., "Measurement of Solid Particle Velocity in Erosive Wear," *Wear,* 1975, 35, 195-199.

[3] Veprek, S., Reiprich, S., and Shizhi, L., "Superhard Nanocrystalline Composite Materials: The TiN/Si$_3$N$_4$ System," *Appl. Phys. Lett.*, 1995, 66(20), 2640-2642.

[4] Demyashev, G.M., Taube, A.L., and Siores, E., "Superhard Nanocomposite Coatings," *Handbook of Organic-Inorganic Hybrid Materials and Nanocomposites, Vol. 2:Nanocomposites*, American Scientific Publishers, 2003, 1-387.

Acknowledgements

Distribution List

Air Force Research Laboratory
    AFRL/MBTE: Dr. John Jones   Original and one copy
    2941 P. Street, Rm 136   1 e-mail copy; John.Jones@wpafb.af.mil
    Wright-Patterson Air Force Base, Ohio 45433-7750

    AFRL/MLOP: Lt. William Williams   One copy
    2977 P Street, Rm 406   1 e-mail copy; William.Williams@wpafb.af.mil
    Wright-Patterson Air Force Base, Ohio 45433-7750

    AFRL/MBTE: Dr. Jeffrey Sanders   1 e-mail copy; Jeffrey.Sanders@wpafb.af.mil
    AFRL/MBTE: Andrey Voevodin   1 e-mail copy; Andrey.Voevodin@wpafb.af.mil

Office of Naval Research – Administrative Grants Officer
    Sandra Thomson   One copy
    ONR Seattle Regional Office   1 e-mail copy; Sandra_Thomson@onr.navy.mil
    1107 NE45th Street, Suite 350
    Seattle WA 98105-4631

Pennsylvania State University
    Dr. Russell Messier   1 e-mail copy; rfm2@psu.edu
    Dr. Mark Horn   1 e-mail copy; mwh4@psu.edu
    Paul Sunal   1 e-mail copy; pds129@psu.edu

International Technology Corporation
    Dr. Gary McGuire   1 e-mail copy; gmcguire@itc-inc.org
    Dr. Mark Ray, Mark   1 e-mail copy; mray@itc-inc.org

University of Toledo
    Dr. Robert Collins   1 e-mail copy; rcollins@physics.utoledo.edu

North Dakota State University
    Dr. Douglas Schulz   1 e-mail copy: Doug.Schulz@ndsu.edu
    Dr. Douglas Chrisey   1 e-mail copy: Douglas.Chrisey@ndsu.edu
    Dr. Philip Boudjouk   1 e-mail copy: Philip.Boudjouk@ndsu.edu

Appendix A

Real Time Spectroscopic Ellipsometry of Nanocomposite Protective Coatings

Robert W. Collins
Department of Physics and Astronomy
University of Toledo
Toledo, OH 43606-3390

Appendix B

Survey on Methods for Testing and Evaluation of Wear Resistant Coatings

Valery Marinov
Department of Industrial & Manufacturing Engineering
Wayne Reitz
Department of Mechanical Engineering
North Dakota State University
Fargo ND 58105

Real Time Spectroscopic Ellipsometry of Nanocomposite Protective Coatings

A. Experimental Details

Figure 1 shows the instrumental apparatus used for real time analysis of the growth of TiN thin films on freshly deposited Ti thin films. The multichannel spectroscopic ellipsometer developed for this work includes a source consisting of a Xe-D_2 tandem lamp combination. This source provides a spectral range from 1.5 to 6.5 eV in a single detector readout. The broad-band incident light is linearly polarized before entering the chamber, and the light reflected from the growing sample is elliptically polarized such that each wavelength component exhibits a different ellipse shape. A rotating compensator followed by a fixed analyzer is used to characterize all the polarization states in parallel. The different wavelength components are dispersed by a grating spectrograph onto the surface of a photodiode array. Order-sorting filters are incorporated at the surface of the array to avoid higher order grating artifacts. A measurement of the time-dependence of the signal at each pixel of the photodiode array, in synchrony with the rotating compensator, provides the polarization ellipse shape as a function of wavelength. From these polarization characteristics, the properties of the growing sample in the chamber can be deduced based on an extensive software package developed at Penn State University.

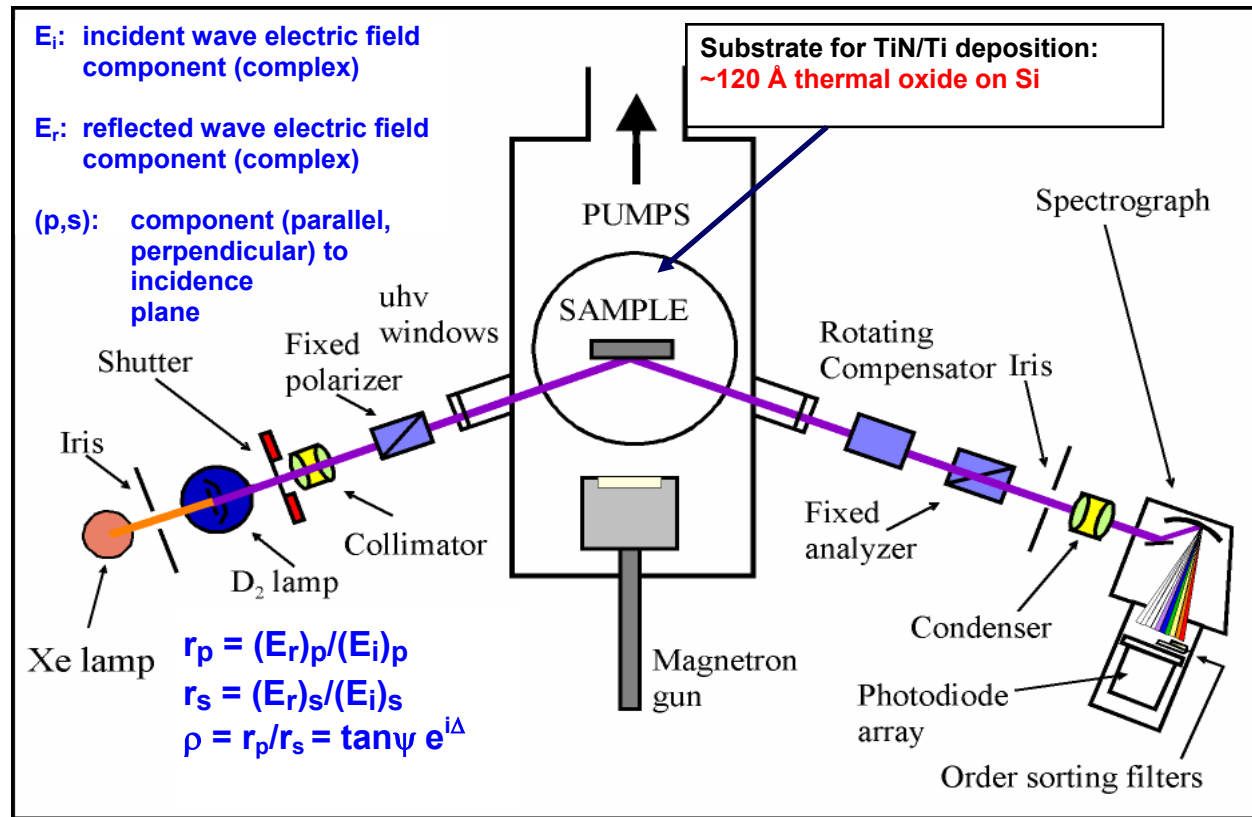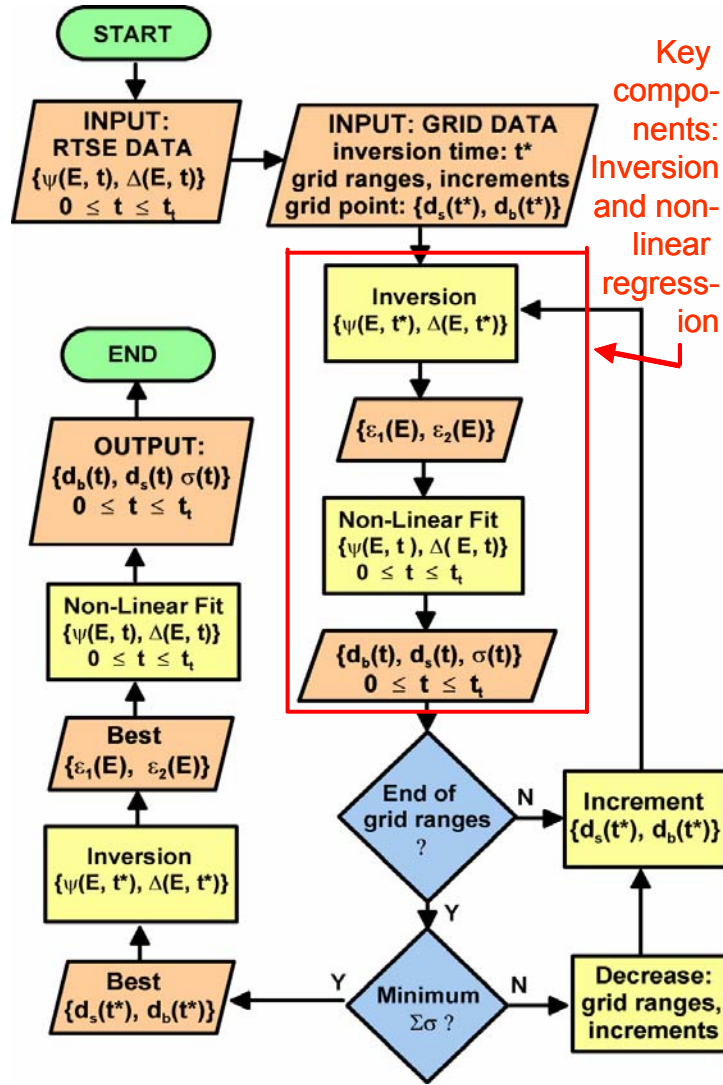Fig. 1: Instrumentation for real time spectroscopic ellipsometry of nanostructured protective coatings.

Fig. 2: Program developed to analyze real time spectroscopic ellipsometry data collected on nanostructured protective coatings.

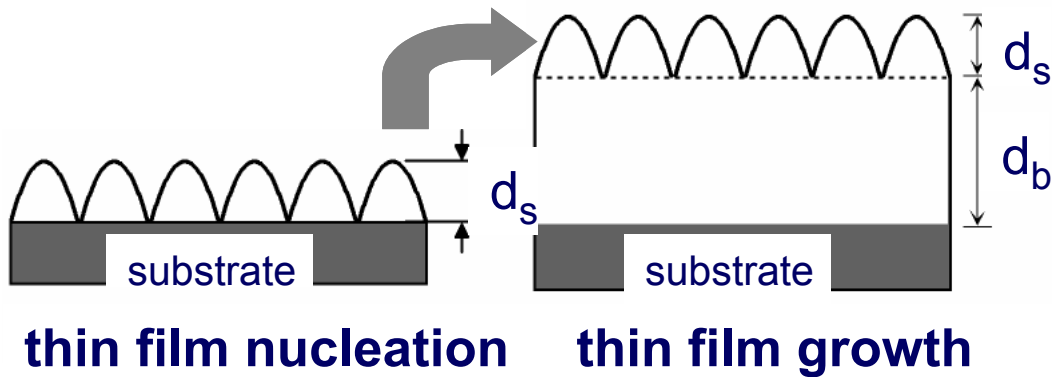thin film nucleation   thin film growth

Fig. 3: Optical model used for the analysis of real time spectroscopic ellipsometry data collected during Ti film growth.

Figure 2 shows a flow chart that describes the data analysis procedure used throughout this study. The key components of the analysis include mathematical inversion to extract the dielectric function of the growing film from the ellipsometric spectra and least-squares regression to extract the evolution of the sample structure, including surface roughness and bulk layer thicknesses. These two components are applied iteratively, as shown by the loop in the flow chart, in order to identify the best overall combination of dielectric function and structural evolution that minimizes the deviations between a model simulation and the experimental data.

As shown in Figure 3, the structural model used for Ti film growth starts with a single nucleating layer, modeled as a 0.5/0.5 volume fraction mixture of the bulk material of the growing film along with free space. This model is applied when the deduced bulk layer is less than a single monolayer. As time progresses, isolated nuclei make contact to form a discrete bulk layer having residual surface roughness. The resulting structure is modeled as two layers including bulk and surface roughness components. As in the case of the initial nucleating layer, the surface roughness layer is also modeled as a 0.5/0.5 volume fraction mixture of bulk material and voids. The optical properties of the nucleating and surface roughness layers are determined using the Bruggeman effective medium theory. Figure 4 shows the model used for the growth of the TiN on Ti. The approach is similar to that for the growth of Ti directly on SiO_2/Si with the exception that the Ti underlayer in TiN growth is rough and so the initial growth of the TiN must include an interface roughness filling process.

50% TiN + 50% Air

TiN

50% Ti + 50% TiN

Ti

SiO_2

c-Si

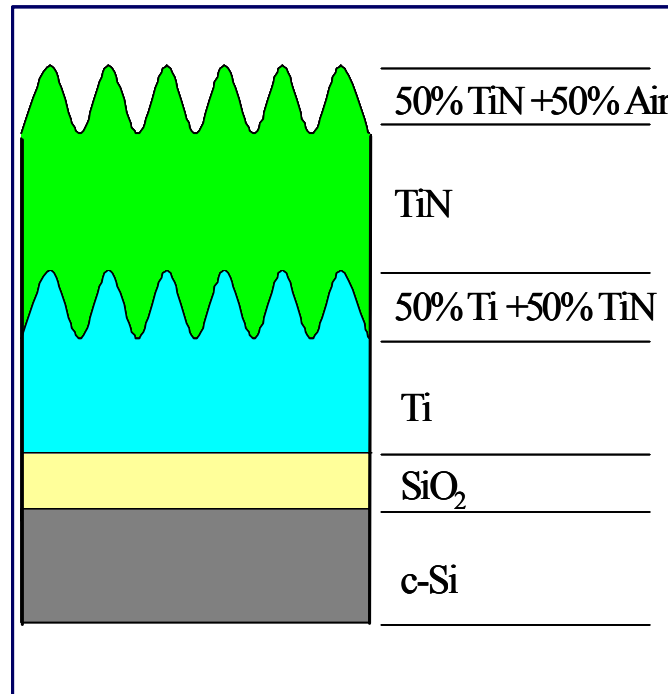Fig. 4: Structural model for the growth of TiN on Ti, applying the case in which the only non-idealities are due to surface roughness on the Ti (which leads to Ti/TiN interface roughness), and surface roughness on the final TiN film. In reality, additional Ti/TiN interface non-idealities occur due to contamination and microstructure associated with the gas switch-over from pure Ar to pure N_2, followed by Ti target nitridation.

The starting substrates used in this study were c-Si wafers thermally oxidized to a thickness of ~120 Å, as determined in an ellipsometric analysis of the initial substrate. The Ti and TiN films were deposited by magnetron sputtering on room temperature substrates. The details of this process appear elsewhere [Paul Sunal, Ph.D. Thesis, Department of Engineering Science and Mechanics, The Pennsylvania State University, University Park, PA 16802].

B. Overview of Deposition Process

Figures 5-9 present the results of real time spectroscopic ellipsometry analysis obtained in a full deposition sequence consisting of six steps labeled at the top of each figure. These steps
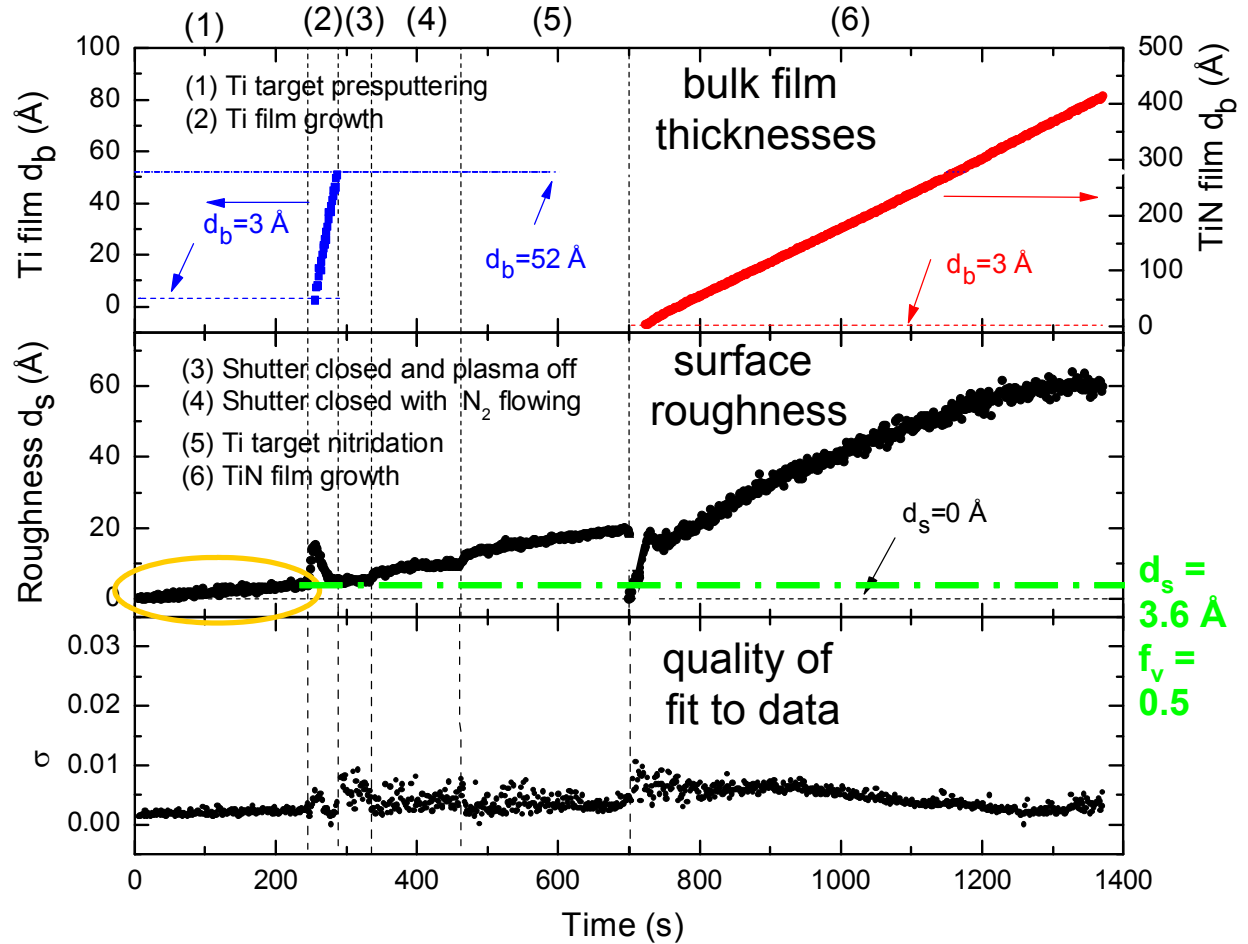
Fig. 5: The first step in the full Ti/TiN process characterization: Ti target presputtering (see oval). The presputtering conditions were as follows: Ar gas flow: 10 sccm, Ar pressure: 10 mTorr, presputtering power: 100 W. The film that forms during Ti target presputtering is modeled as a single layer of thickness d_s consisting of 0.5/0.5 volume fractions of Ti/void. The effective thickness or (volume/area) is given by $d_{eff} = 0.5\ d_s$. During the 4 min target presputtering time an effective thickness of ~ 1.8 Å of Ti, corresponding to a partial monolayer, forms on the SiO_2/Si substrate due to diffusion of presputtered species around the shutter which is in place during the presputtering step.

include: (1) Ti target presputtering before Ti film growth (Fig. 5); (2) Ti film growth (Fig. 6); (3)+(4) Ar gas removal and N_2 gas initiation (Fig. 7); (5) target nitridation before TiN growth (Fig. 8); and (6) TiN growth (Fig. 9). For the first step, shown in Fig. 5, the presputtering conditions were as follows: Ar gas flow: 10 sccm, Ar pressure: 10 mTorr, presputtering power: 100 W. The film that forms during Ti target presputtering can be modeled assuming a single layer of thickness d_s consisting of 0.5/0.5 volume fractions of Ti/void. During the 4 min target presputtering time an effective thickness of ~ 1.8 Å of Ti, corresponding to a partial monolayer, forms on the SiO_2/Si substrate due to the accumulation of presputtered species that arrive at the substrate via around the shutter which is in place during the presputtering process.
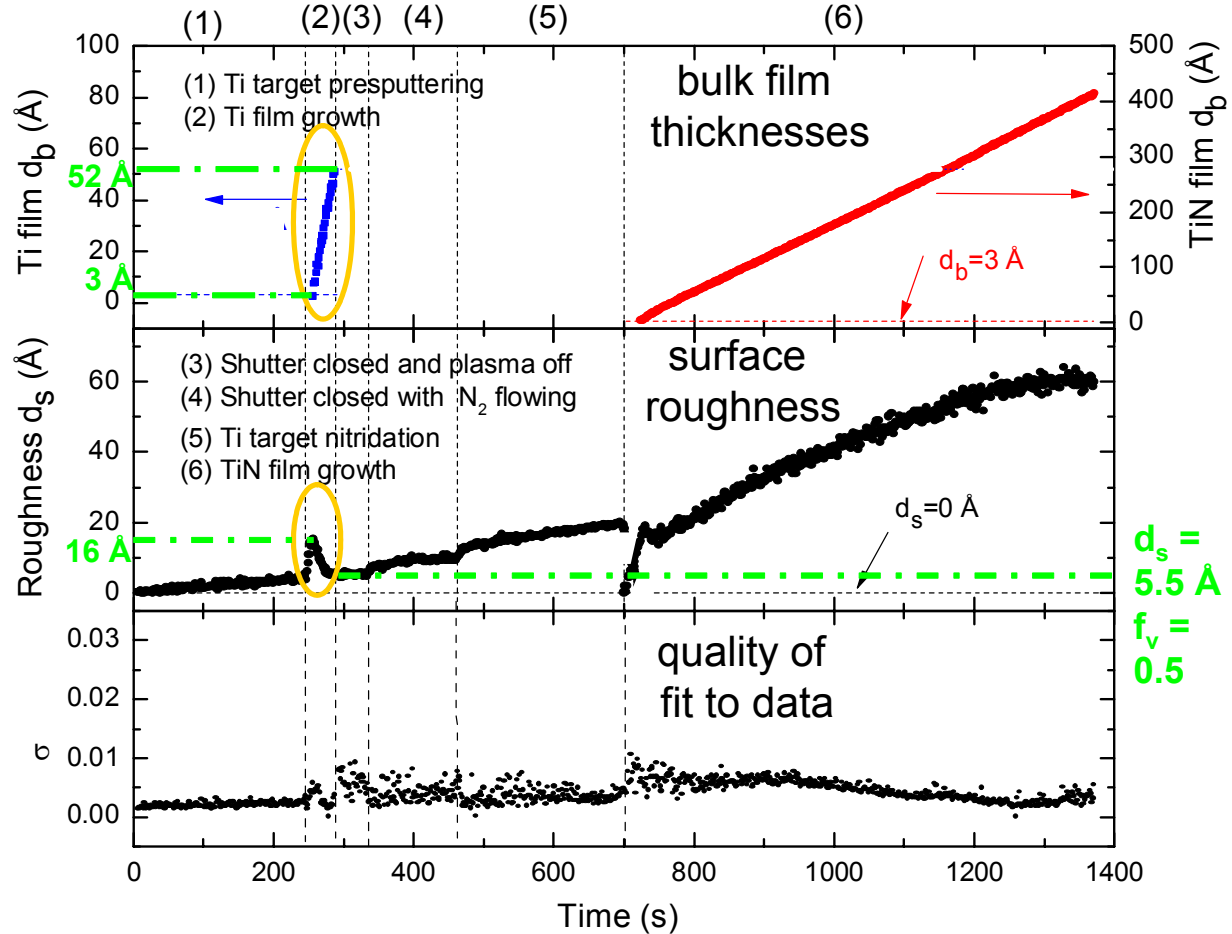
Fig. 6: The second step in the full Ti/TiN process characterization: smooth Ti film growth (see ovals). The Ti growth conditions were as follows: Ar gas flow: 10 sccm, Ar pressure: 10 mTorr, sputtering power: 100 W. The growing Ti film in this case is modeled as two layers, including a bulk layer of thickness d_b and a surface roughness layer of thickness d_s, the latter consisting of 0.5/0.5 volume fraction of Ti/void. The effective thickness or (volume/area) is given by $d_{eff} = d_b + 0.5\ d_s$. During the 50 s Ti deposition, the film nucleates with a cluster thickness of 16 Å (lower oval). Almost complete coalescence of clusters occurs within a bulk layer thickness of 52 Å (upper oval) leaving a residual surface roughness layer of thickness 5.5 Å (< 2 ML, lower oval). This purpose of this process step is to form a smooth, reproducible substrate for TiN deposition.

After 4 min of presputtering, the shutter blocking the substrate is partially opened to initiate Ti film growth on the substrate. The deposition conditions during growth were the same as those during presputtering. The growing Ti film is modeled assuming two layers, including bulk and surface roughness layers of thickness d_b and d_s, as shown in Fig. 6. During the 50 s Ti deposition, the film nucleates with a cluster thickness of 16 Å before the onset of bulk film growth, which is defined as the time at which d_b reaches ~3 Å. Almost complete coalescence of clusters occurs within a bulk layer thickness of 52 Å (upper oval in Fig. 6) leaving a residual surface roughness layer of thickness 5.5 Å (< 2 ML, lower oval in Fig. 6). This purpose of this process step is an attempt to form a smooth, reproducible substrate for the subsequent TiN depositions.
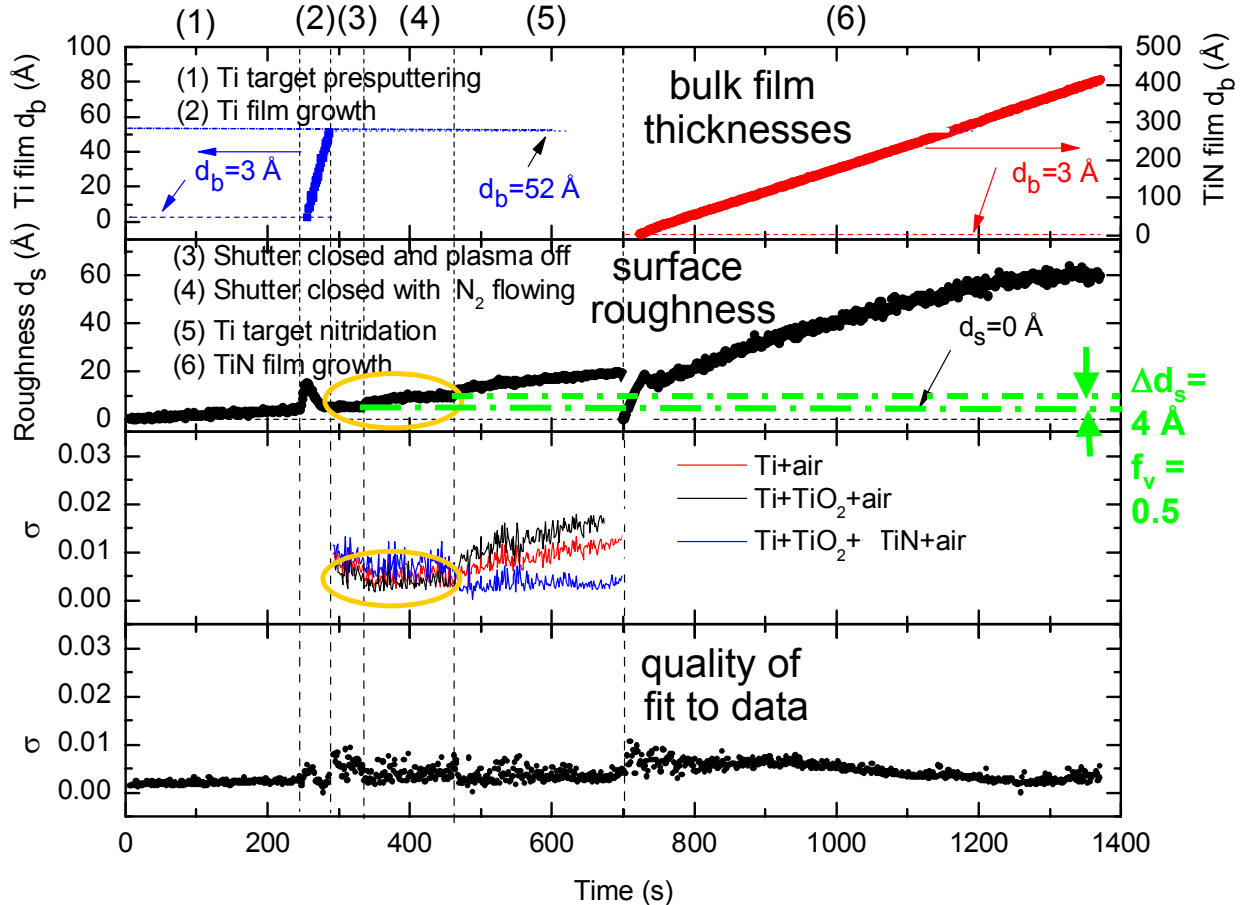
Fig. 7: The third and fourth steps in the full process characterization: pure Ar gas flow removal and pure N_2 gas flow initiation. The flow conditions are as follows: Ar gas flow: 10 sccm, Ar pressure: 10 mTorr, N_2 gas flow: 10 sccm, N_2 pressure: 10 mTorr. Different single layer models were applied in fits to the data. All models for the composition of this layer show relatively good fits during the two steps, including (Ti+void, Ti+TiO$_2$+void, Ti+TiO$_2$+TiN+void); the best fit is with Ti+TiO$_2$+void. Thus, the final model adopted for the film that forms during Ar gas removal and N_2 gas initiation includes a single layer of thickness d_s with a dielectric function calculated assuming a low density Ti-rich oxide of volume fraction composition given by 0.25/0.25/0.5 Ti/TiO$_2$/void. During the 3 min gas switch-over from Ar to N_2, a 4 Å thick layer develops on the surface. The thickness of this layer appears to saturate over time, unlike the layer that forms during presputtering.

In the third and fourth steps shown in Fig. 7, the pure Ar gas used for Ti deposition is removed from the chamber and replaced by pure N_2 in order to prepare for the TiN deposition process. The N_2 flow is 10 sccm and the N_2 pressure is 10 mTorr. Different single layer models were applied in fits to the real time spectroscopic ellipsometry data in this process regime. The final model adopted for the film that forms during both Ar gas removal and N_2 gas influx includes a single layer of thickness d_s with a dielectric function calculated from the three-component Bruggeman effective medium theory assuming a low density Ti-rich oxide. The best fit composition of this oxide is ~ 0.25/0.25/0.5 Ti/TiO$_2$/void. During the 3 min gas switch-over time, a 4 Å thick layer develops on the surface. The time evolution of this layer is different than that forming during the presputtering process of Fig. 6. The thickness of the layer in Fig.7 appears to saturate over time, as might be expected for a diffusion-limited oxidation process. Evidently contamination of the Ti surface occurs in this process and the contamination rate is higher during N_2 flow.
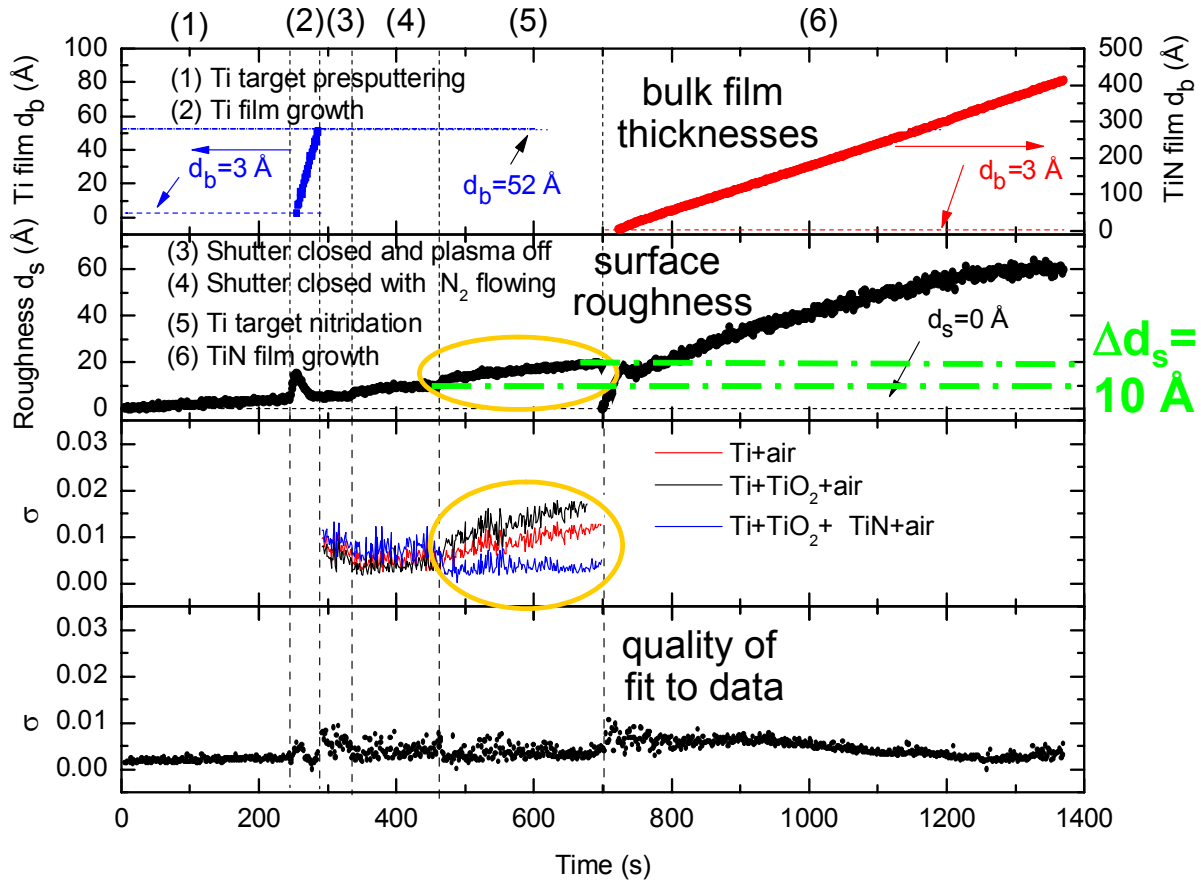
Fig. 8: The fifth step in the full Ti/TiN process characterization: Ti target nitridation (see ovals). The nitridation conditions are as follows: N_2 gas flow: 10 sccm, N_2 pressure: 10 mTorr, nitridation power: 200 W. The final model adopted for the film that forms during target nitridation includes a single layer of thickness d_s with a dielectric function calculated assuming a low density Ti oxynitride of volume fraction composition 0.25/0.25/0.15/0.35 Ti/TiO$_2$/TiN/void. During the 4 min Ti target nitridation, a 10 Å thick low-density layer of this material develops on the surface due to diffusion of sputtered species around the shutter. This layer also appears to include oxygen contaminants.

Once the N_2 gas flow is stable, the fifth process step of Ti target nitridation is initiated (see ovals in Fig. 8) using a nitridation power of 200 W. The final model that provides the best fit to data collected during target nitridation includes a single layer of thickness d_s with a dielectric function calculated assuming a low density Ti oxynitride of volume fraction composition 0.25/0.25/0.15/0.35 $Ti/TiO_2/TiN/void$. During the 4 min Ti target nitridation, a 10 Å thick layer of this material develops on the surface. This layer appears to build up linearly with time, as in the Ti target presputtering process, suggesting a source of Ti atoms due to diffusion of sputtered species around the shutter. The composition can be understood in terms of the build up of a surface roughness layer containing oxygen atoms due to contamination and N atoms due to interaction of the growing layer with excited N_2 that also manages to diffuse around the shutter.

Once target nitridation is complete, the shutter is opened to initiate TiN deposition. The model for the film that forms during TiN deposition includes 3 layers: (i) a bulk layer of thickness d_b, which by definition is > 3 Å thick, (ii) a surface roughness layer of thickness d_s, consisting of 0.5/0.5 volume fractions of TiN/void, and (iii) an interface roughness layer of thickness d_i, consisting of 0.25/0.25/0.5 volume fraction mixture of $Ti/TiO_2/TiN$. This latter layer derives from the 0.25/0.25/0.15/0.35 $Ti/TiO_2/TiN/void$ surface roughness layer from the fifth step
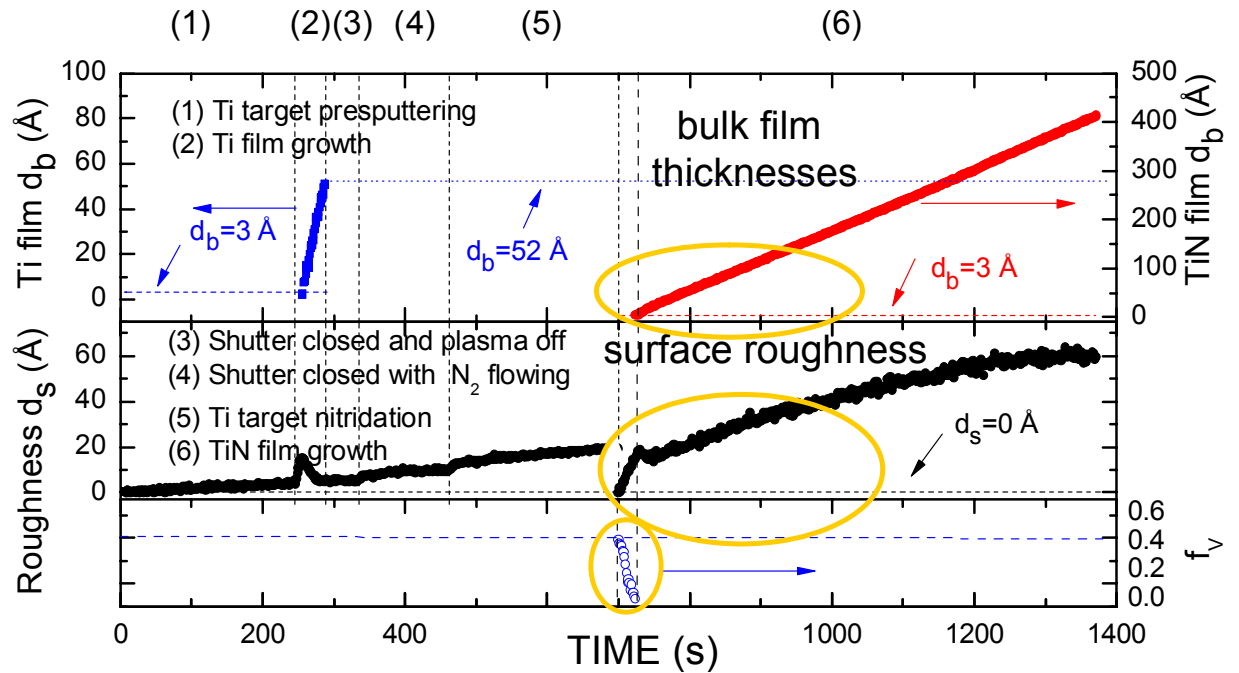
Fig. 9: The sixth step in the full process characterization: TiN film deposition. The deposition conditions are as follows: N_2 gas flow: 10 sccm, N_2 pressure: 10 mTorr, sputtering power: 200 W. Model for the film that forms during TiN deposition includes 3 layers: a bulk layer of thickness d_b, which by definition is > 3 Å, a surface roughness layer of thickness d_s, consisting of 0.5/0.5 volume fractions of TiN/void, and an interface roughness layer of thickness d_i, consisting of 0.25/0.25/0.5 volume fraction mixture of $Ti/TiO_2/TiN$. During the ~11 min TiN deposition, TiN fills in the underlying surface roughness layer, leading to a ~20 Å interface roughness layer. Weak coalescence is observed; however, the dominant effect is surface roughening in which 60 Å of roughness develops during 400 Å of bulk layer TiN growth.

when the void component representing surface connected void structures fills in with depositing TiN. During the ~11 min TiN deposition, TiN fills in the underlying surface roughness layer, leading to a ~20 Å interface roughness layer. Weak coalescence is observed by about a monolayer (i.e., the smoothening after the peak in the cluster thickness); however, the dominant effect during the growth process is surface roughening in which 60 Å of roughness develops during 400 Å of bulk layer TiN growth.

In the following Sections C through G, the processes (1), (2), (3)+(4), (5), and (6) will be treated in much greater detail in an attempt to understand the nature of these processes and their impacts on the resulting film structure and properties.
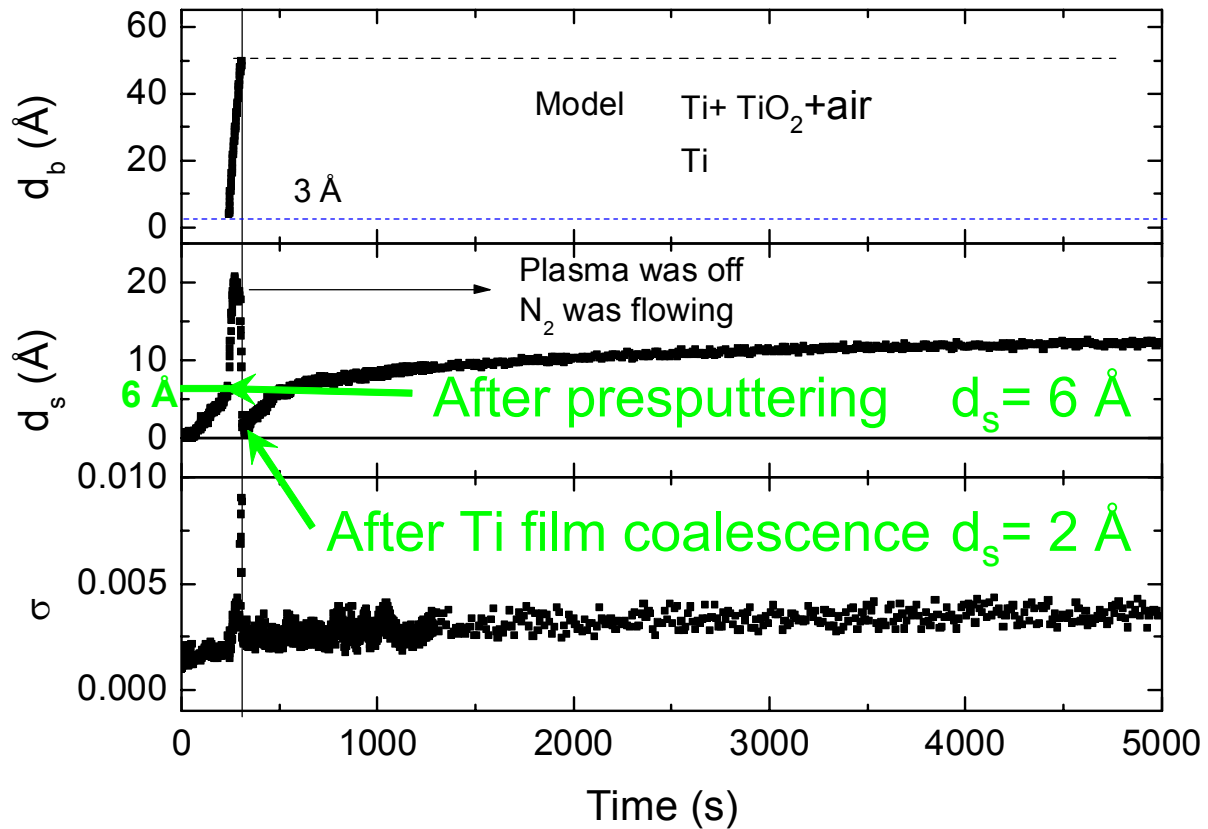
Fig. 10: Effect of the first process outcome, i.e., the film thickness after presputtering, on the second process, i.e., Ti film growth. The Ti target presputtering and film growth conditions include a pure Ar flow at 10 sccm, a plasma power of 100 W, and a pressure of 10 mTorr. In a 4 min presputtering time, a 2/3 thicker initial layer is obtained with $d_{eff} = (0.5)(6 \text{ Å}) = 3 \text{ Å}$ due to a difference in shutter blocking efficiency. In spite of this added thickness, however, improved coalescence is observed in this case with a minimum roughness of $d_s = 2 \text{ Å}$ at a bulk layer thickness of 50 Å. Studies such as this one show that the presputtering layer thickness does not adversely affect the coalescence and ultimate smoothness of the Ti substrate layer for TiN film growth.

C. Role of Target Presputtering Accumulation on Subsequent Ti Deposition

To explore the role of the target presputtering effect on the subsequent Ti substrate film deposition, the first two steps of the overall process (see Figs. 5 and 6) were studied in which the shutter was in a slightly different position during presputtering in comparison with the experiment of Fig. 5. This led to a larger accumulation during the 4 min presputtering time. Figure 10 shows results in which the presputtering thickness was 6 Å, rather than 3.6 Å as in Fig. 5. Thus, it is of interest to determine if this enhanced presputtering accumulation suppresses the usual nucleation and coalescence process that leads to an ultra-smooth Ti surface. In fact, Figure 10 shows that after 6 Å presputtering accumulation, the film nucleates and coalesces, achieving an ultra-smooth surface with roughness at the sub-monolayer level (~2 Å) after a bulk layer thickness of 50 Å. This is a desirable result indicating that one need not be concerned about the details of presputtering accumulation in order to develop a smooth, reproducible Ti film for use as a substrate. This result is reasonable because the presputtered layer likely forms as clusters of Ti that are then continuously integrated into the over-deposited film. It is possible, however, that the presputttered layer, because it forms at such a low rate, includes a higher level of contaminants compared to the over-deposited material obtained with the shutter open. Due to the thinness of the presputtered layer and its high void fraction, any contaminant effect is difficult to assess by the optical probe.

D. Growth of Ti Substrate Films

The goal of the Ti film deposition process is to establish a technologically-relevant substrate material that is reproducibly prepared, free of process-dependent contamination, and presents a relatively smooth surface that enables easy analysis of spectroscopic ellipsometry data when TiN is over-deposited on the surface. In this study, we explored the effect of deposition parameters on the growth process of Ti, seeking conditions that lead to the smoothest possible surface. The effect of gas pressure and plasma power, factors that controls ion bombardment energies and the deposition rate, will be discussed in detail here.

In Fig. 11, the microstructural evolution is shown for a series of Ti depositions at different pressures. The results include the bulk layer thickness d_b and the cluster and surface roughness thickness d_s during Ti cluster formation, contact, and coalescence on (120 Å SiO_2)/Si substrates held at room temperature. For the series of films in Fig. 11, the plasma power was fixed at 100 W, the pure Ar flow was fixed at 10 sccm, and the Ar pressure was varied over the range from 2.5 to 15 mTorr. The results of this study reveal a narrow regime of pressure near 10 mTorr over which clustering and complete coalescence occurs to an ultra-smooth surface. At pressures above this range there is a weak coalescence effect after which significant roughening occurs. This finding suggests that at the high pressure, surface diffusion due to ion bombardment is reduced and this weakens the coalescence effect. At lower pressures, clustering and coalescence are suppressed presumably due to excess bombardment that leads to penetration of incident ions below the top monolayer. Among the characteristics of growth at a pressure of 10 mTorr include: (i) a cluster thickness maximized at $d_s = 17$ Å at the onset of bulk layer growth, (ii) a surface roughness layer thickness minimized at $d_s = 3.7$ Å when the bulk layer thickness is $d_b = 50$ Å, and (iii) an effective deposition rate of $d(d_{eff})/dt = 1.27$ Å/s , where $d_{eff} = d_b + 0.5d_s$.
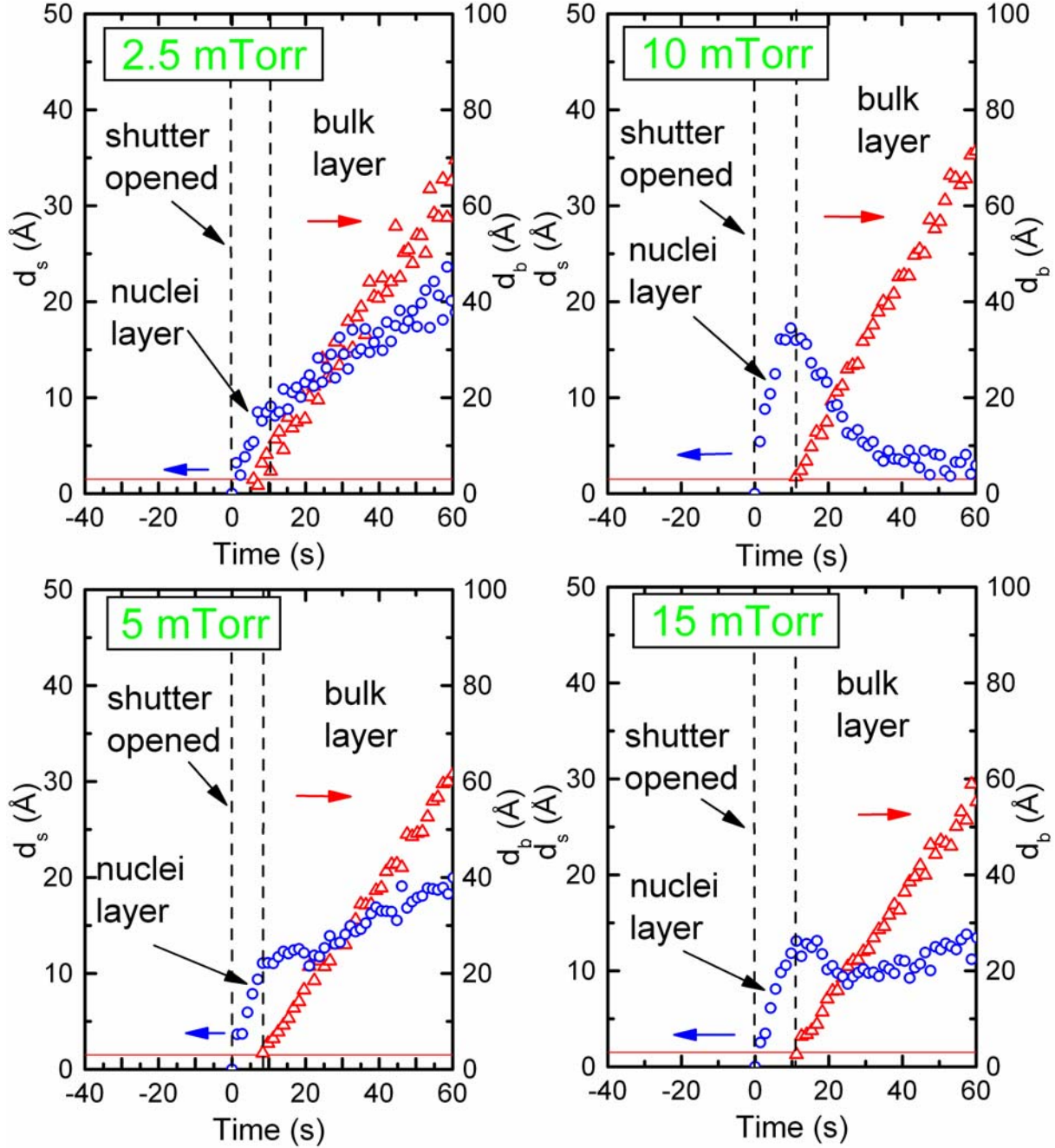
Fig. 11: Evolution of the bulk layer thickness d_b, and the cluster and surface roughness thickness d_s during Ti cluster formation, contact, and coalescence on (120 Å SiO$_2$)/Si substrates. The plasma power was fixed at 100 W, the pure Ar flow was fixed at 10 sccm, and the Ar pressure was varied over the range 2.5 - 15 mTorr. The results of this study reveal a narrow regime of pressure near 10 mTorr over which clustering and complete coalescence to a smooth surface occurs. Among the characteristics of growth at 10 mTorr include: (i) a cluster thickness of d_s = 17 Å at the onset of bulk layer growth, a surface roughness layer thickness of d_s = 3.7 Å when the bulk layer thickness is d_b = 50 Å, and an effective deposition rate of $d(d_{eff})/dt$ = 1.27 Å/s , where $d_{eff} = d_b + 0.50 d_s$.

Fig. 12: (Left) cluster thickness at the onset of bulk layer growth versus Ar pressure; (lower right) effective thickness versus time; and (lower left) roughness layer thickness versus effective thickness, all for Ti films prepared at different Ar pressures. These results suggest optimum surface diffusion at 10 mTorr. At higher pressures bombardment effects are moderated, reducing surface diffusion. At lower pressures enhanced bombardment leads to subsurface implantation -- hence the stable surface roughness layers at low pressures.

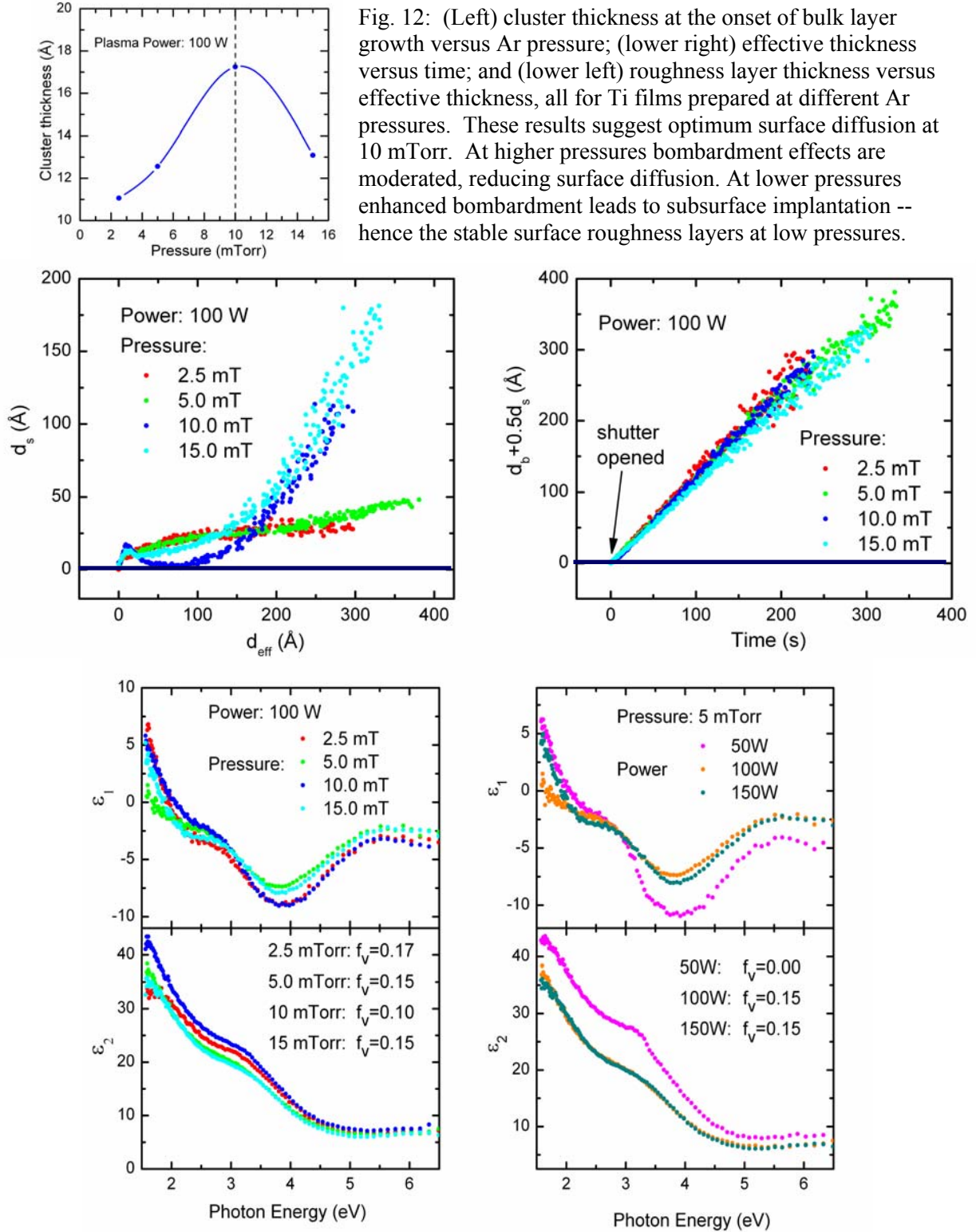Fig. 13: Two Ti deposition series including Ar pressure variation (2.5 - 15 mTorr) at fixed plasma power (100 W) (left), and power variation (50 - 150 W) at fixed pressure (5 mTorr) (right). Two approaches are apparent for film densification. (i) At elevated power (100 W) and rates (~1.2 Å/s) surface diffusion must be optimized; (ii) under ion bombardment conditions the deposition rate must be reduced (to 0.5 Å/s).

Figure 12 demonstrates the clear maximum at 10 mTorr in the cluster thickness at the onset of bulk layer growth as described in the previous paragraph. Also shown in Fig. 12 is the effective thickness versus time as well as the roughness layer thickness versus effective thickness, all for Ti films prepared at different Ar pressures. The full set of results support the concept of optimum surface diffusion at 10 mTorr. As has been suggested from Fig. 11, higher pressures moderate bombardment, thus reduce surface diffusion. At lower pressures, enhanced bombardment leads to sub-surface implantation -- hence the stable surface roughness layers at low pressures (Fig. 12, lower left).

Figure 13 shows the dielectric functions deduced from the same data analysis procedure that provides the microstructural evolution of Figs. 11 and 12. Here results are given for two Ti deposition series including: (i) the same Ar pressure variation of Figs. 11 and 12, (2.5 - 15 mTorr) at fixed plasma power (100 W), as well as (ii) a power variation (50 - 150 W) at fixed pressure (5 mTorr). Two approaches are proposed for film densification. (i) At elevated power (100 W) and rates (~1.2 Å/s) surface diffusion must be optimized through pressure optimization; (ii) under the high ion bombardment conditions achieved at low pressure, the deposition rate (i.e., the plasma power) must be reduced (to 0.5 Å/s) in order to assure a high density.

Ti Film Growth Summary

A narrow range of sputtering pressure (~10 mTorr) is found to promote surface diffusion without bombardment damage. This leads to (i) the largest clusters in the nucleation stage of growth (d_s = 17 Å at d_b= 0 Å); (ii) the strongest coalescence effect (Δd_s = 14 Å for d_b = 3 $\rightarrow$ 50 Å); and (iii) the smoothest surface after coalescence (d_s = 3 Å at d_b = 55 Å). To obtain a stable surface during bulk film growth and the smoothest surface in a thick film, a low pressure is best (optimum case at 2.5 mTorr: d_s = 30 Å at d_b = 300 Å). To obtain the highest density film during bulk growth, a low pressure and a low power are best (optimum case at 5 mTorr and 50 W).

E. Contamination of Ti Surface during N_2 Gas Flow

Although a reproducible Ti film surface is sought for over-deposition of TiN, well defined changes in the near-surface Ti film have been observed in three steps, starting with Ar gas removal, following by N_2 gas flow initiation, and concluding with Ti target nitridation. In this section the focus will be on the surface processes occurring during Ar and N_2 gas flow. The experiment of Fig. 14 has been designed to determine whether the layer forming during the N_2 flow is due to N_2 reaction with the surface or to vacuum residuals. In this experiment, the contamination rate of Ti substrates is measured first under a vacuum of 10^{-6} Torr. The following models have been applied to the data collecting during vacuum exposure: (i) a low-density inhomogeneous oxide layer (0.25/0.25/0.5 Ti/TiO$_2$/void) with no loss of the underlying Ti material; (ii) dense inhomogeneous oxide (0.5/0.5 Ti/TiO$_2$) with simultaneous Ti bulk layer thickness reduction; (iii) low-density inhomogeneous oxide (0.25/0.25/0.5 Ti/TiO$_2$/void) with simultaneous Ti thickness reduction. Figure 15 shows the general model used here that covers the three possibilities explored in Fig. 14: (i) d_s variable, d_b fixed, and d_i = 0 Å; (ii) d_s fixed, d_b variable, and d_b+d_i fixed; (iii) d_s variable, d_b variable, and d_i = 0 Å. Note that the first model is unphysical as it does not conserve Ti atoms, and in fact this model provides the poorest fit. The best fit is provided by model (iii) and provides information on the rate of contamination of the Ti

film from vacuum residuals. Specifically, the best fit results of Fig. 14 suggest that during ~ 2 hr under vacuum, 5 Å bulk Ti converts to 9 Å of the low-density, inhomogeneous Ti oxide.

In Fig. 16, the contamination rates are compared for Ti films under vacuum as in Fig. 14 and under N_2 flow as in Fig. 7. Under vacuum, the surface layer develops more gradually in the initial stages and consumes underlying Ti. This suggests that the contaminant layer is associated with the usual oxidation of Ti due to residual gases in the vacuum. Under N_2 flow, the surface layer develops more quickly. This suggests that the layer -- in the form of TiN, TiO_2, or hydrocarbons -- derives from the N_2 source (rather than from the residual gases). The best fitting result is obtained with a low-density Ti-rich oxide (0.25/0.25/0.5 TiO_2/Ti/voids) as in Fig. 14.
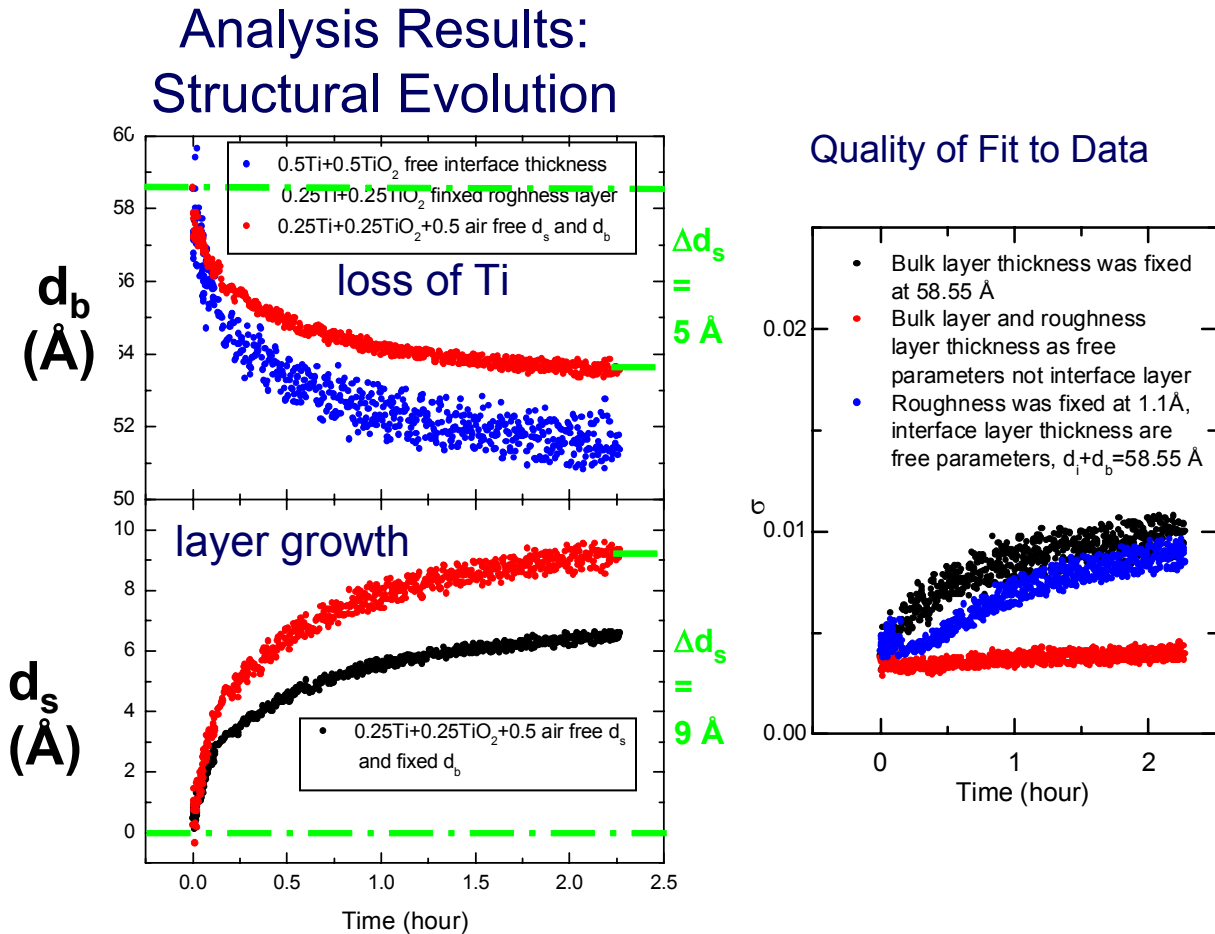
Fig. 14: First step in the assessment of the layer that forms during N_2 flow in advance of target nitridation. This experiment has been designed to determine whether the layer forming during N_2 flow is due to N_2 reaction with the surface or to vacuum residuals. In this experiment, the contamination rate of Ti substrates is measured under a vacuum of 10^{-6} Torr. The following model results are shown: black (lowest data set for d_s, uppermost data set for σ) low-density inhomogeneous oxide with no loss of underlying material (unphysical: does not conserve Ti atoms); blue (lower data set for d_b and center data set for σ) dense inhomogeneous oxide with simultaneous Ti thickness reduction; red (upper data sets for d_b and d_s and lowest data set for σ) low-density inhomogeneous oxide with simultaneous Ti thickness reduction.
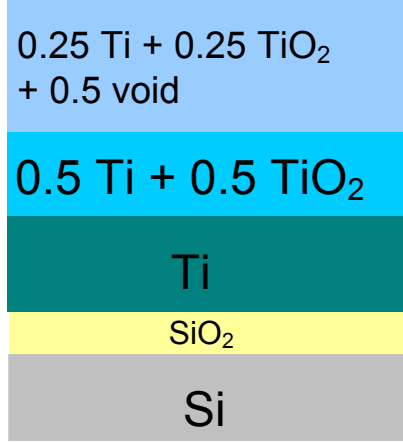
Fig. 15: General model used that covers the three possibilities explored in Fig. 14: (i) (black, in Fig. 14) d_s variable, and $d_i = 0$ Å; (ii) (blue, in Fig. 14) d_s fixed, d_b variable, and d_b+d_i fixed; (iii) (red, in Fig. 14) d_s variable, d_b variable, and $d_i = 0$ Å. The results of Fig. 14 suggest that during ~ 2 hr under vacuum, 5 Å bulk Ti converts to 9 Å low-density, inhomogeneous Ti oxide.
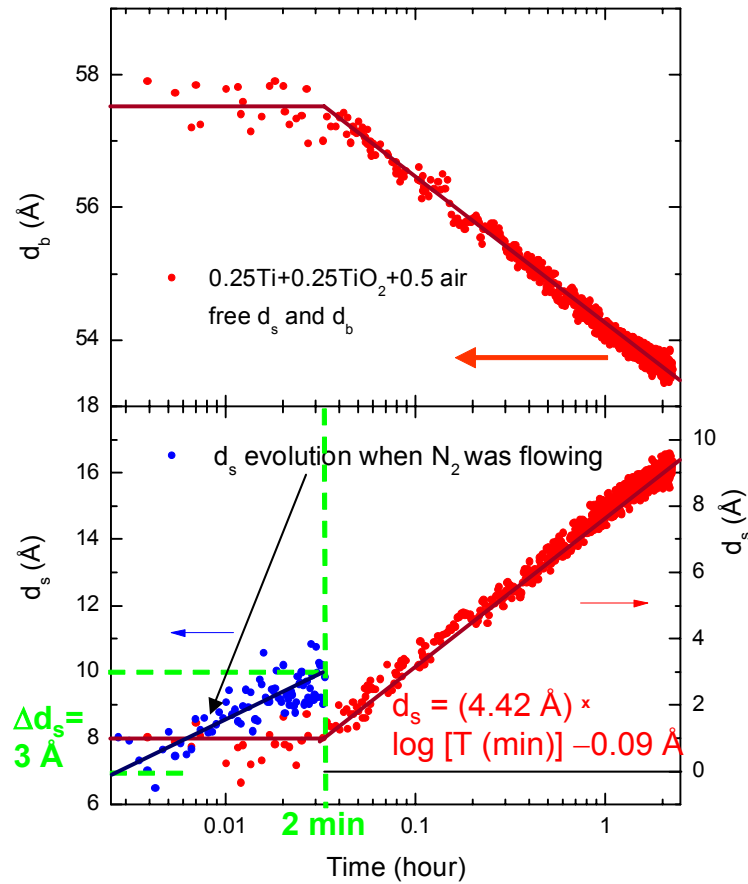
Fig. 16: Here contamination rates of Ti substrates under vacuum (10^{-6} Torr; red -- two hr data set) and under N_2 (10 mTorr, 10 sccm; blue -- 2 min data set at left) are shown. Under vacuum, the surface layer develops more gradually in the initial stages and consumes underlying Ti. This suggests that the contaminant layer is associated with the usual oxidation of Ti. Under N_2 flow, the surface layer develops more quickly. This suggests that the layer derives from the N_2 source (rather than from the residual gas), in the form of TiN, TiO_2, or hydrocarbons. The best fitting result is obtained with a low-density Ti-rich oxide (0.25/0.25/0.5 TiO_2/Ti/voids). (See Figs. 14 and 15.)

Figure 17 shows results of the analysis of data collected during an extended exposure of the Ti surface to N_2. The following growth models have been assessed: (i) a low-density inhomogeneous oxide with no loss of underlying Ti; (ii) a dense inhomogeneous oxide with Ti thickness loss; (iii) a low-density inhomogeneous oxide with Ti thickness loss; and (iv) a low-density inhomogeneous mixture of Ti oxide and nitride with Ti thickness loss. Figure 18 shows a schematic model that covers the four possibilities explored in Fig. 17: (i) d_s variable with TiO_2 as the third surface layer component, d_b fixed, and $d_i = 0$ Å; (ii) d_s fixed with TiO_2 as the third surface layer component, d_b variable, and d_b+d_i fixed; (iii) d_s variable with TiO_2 as the third surface layer component, d_b variable, and $d_i = 0$ Å; (iv) same as in (iii) but with TiN as the third surface layer component. The poorest fits result from the unphysical model (i) as well as from model (ii) for a dense oxide. The best fit is obtained using the same model as was applied to
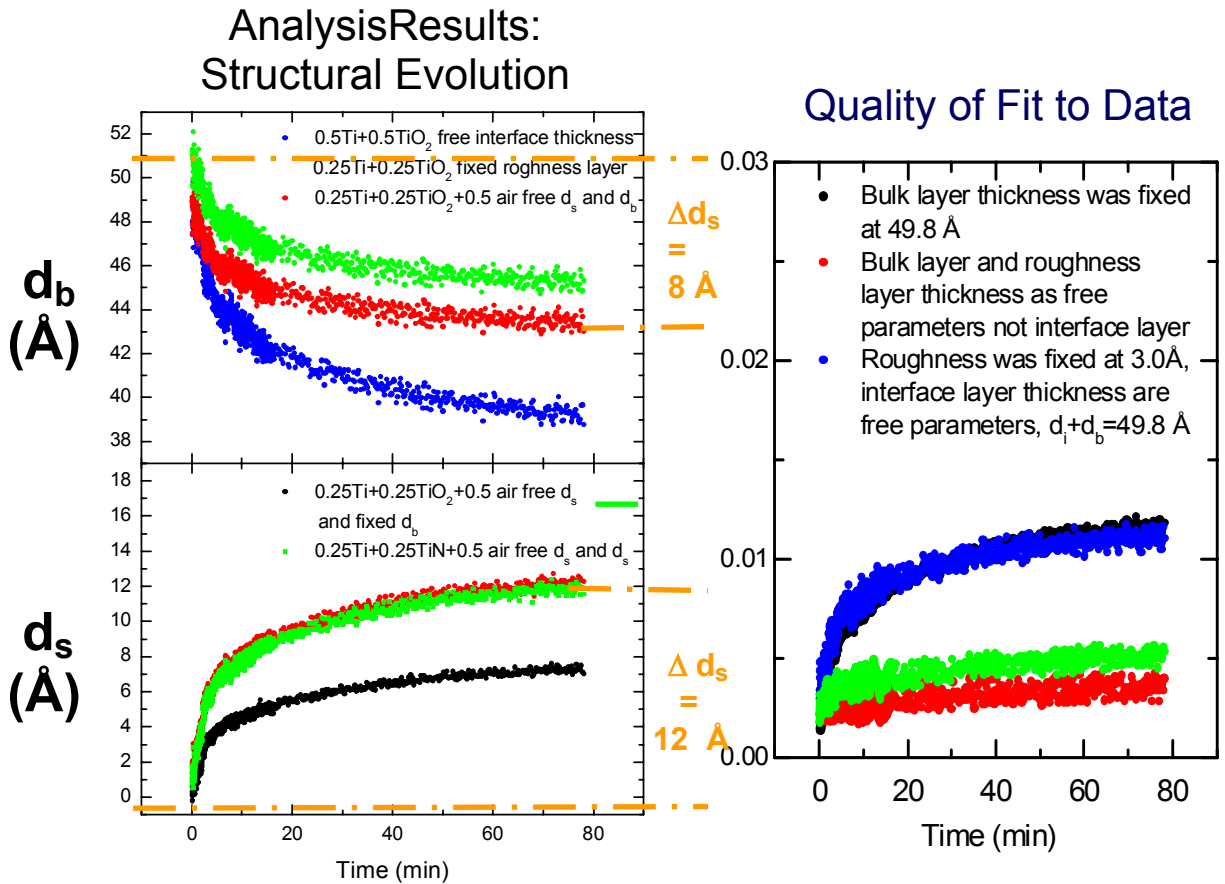
Fig. 17: Results of the analysis of data collected during extended exposure of the Ti surface to N_2. This experiment was conducted in order to achieve improved compositional sensitivity to layer development. The following model results are shown: black (lowest data set for d_s and uppermost data set for σ at 75 min) -- low-density inhomogeneous oxide with no loss of underlying Ti (unphysical); blue (lowest data set for d_b and second highest data set for σ at 75 min) -- dense inhomogeneous oxide with Ti thickness loss; red (center data set for d_b, uppermost data set for d_s, and lowest data set for σ) low-density inhomogeneous oxide with Ti thickness loss; green (uppermost data set for d_b, center data set for d_s, and second lowest data set for σ) -- low-density inhomogeneous mixture of Ti oxide and nitride with Ti thickness loss.

Fig. 18: General model used that covers the four possibilities explored in Fig. 17: (i) (black, in Fig. 17) d_s variable with TiO_2 as the third surface layer component, d_b fixed, and $d_i = 0$ Å; (ii) (blue, in Fig. 17) d_s fixed with TiO_2 as the third surface layer component, d_b variable, and d_b+d_i fixed; (iii) (red, in Fig. 17) d_s variable with TiO_2 as the third surface layer component, d_b variable, and $d_i = 0$ Å; (iv) (green, in Fig. 17) same as in (iii) but with TiN as the third surface layer component. The results of Fig. 17 suggest that during ~ 75 min under N_2 flow, 8 Å of bulk Ti converts to 12 Å of low-density, inhomogeneous oxide.

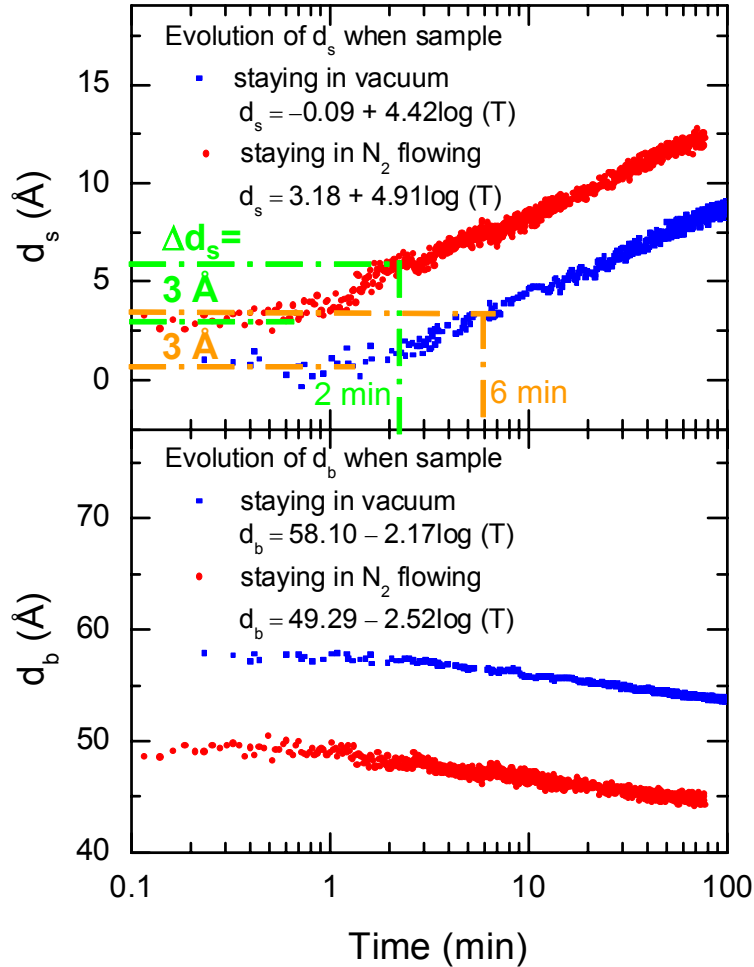Fig. 19: Comparison of contamination rates of Ti thin film substrates under vacuum (10^{-6} Torr) and under extended N_2 flow (10 mTorr, 10 sccm) for ~75 min. Under vacuum, the surface layer acquires 1 ML in a time of ~ 6 min. Under N_2 flow, the surface layer acquires 1 ML in a time of ~ 2 min. Thus, the N_2 is a source of additional contamination (H_2O, O_2, hydrocarbons).

interpret the results of Fig. 14 with the freshly-deposited Ti film under vacuum. The best fit analysis of Fig. 17 suggest that during ~ 75 min under N_2 flow, 8 Å of bulk Ti converts to 12 Å low-density, inhomogeneous oxide. Figure 19 shows results similar to those of Fig. 16 comparing contamination rates of Ti thin films under vacuum (10^{-6} Torr) and under extended N_2 flow (10 mTorr, 10 sccm) for ~75 min. Under vacuum, the surface layer develops to 1 ML in a time of ~ 6 min. Under N_2 flow, the surface layer develops to 1 ML in a time of ~2 min. These results demonstrate that the N_2 is a source of contamination in the form of H_2O, O_2, or hydrocarbons beyond that occurring under vacuum.

F. Target Nitridation in Advance of TiN Film Growth

Figure 20 shows the quality of the fit to the real time spectroscopic ellipsometry data for the Ti surface under vacuum after film growth (first ~ 5 min), and then for the N_2 flow initiation and stabilization (5 − 8 min), and finally for target nitridation (times greater than ~8 min). Extended target nitridation (~ 10 min duration) is performed for improved compositional sensitivity to the surface layer that evolves in this process. In the analysis of the data collected during extended nitridation of the target, the interpretation of Fig. 8 is supported, namely, that the layer formed on the Ti surface is a low density, inhomogeneous mixture of an oxide and nitride.

Figure 21 highlights the models used to describe the extended target nitridation data set of Fig. 20. The model on the left uses a low density inhomogeneous oxide with Ti thickness variation. This is the same model that has been successful in characterizing the contamination that occurs when freshly-deposited Ti is exposed either to vacuum or to a N_2 flow. The best fitting model on the right uses a low density mixture of inhomogeneous oxide and nitride coupled with Ti thickness variation. Figure 22 completes the picture, showing a comparison of contamination rates of Ti under vacuum (10^{-6} Torr) and under extended target nitridation (10 mTorr, 10 sccm, 200 W). Under vacuum, the surface layer develops to 1 ML in a time of ~ 6 min. During target nitridation, the surface layer develops to 1 ML in a time of ~1 min, and only a single monolayer of the underlying film is converted in the entire nitridation time. In this case, the film grows due to a deposition process, as in the case of Ti target presputtering. The successful incorporation of a TiN component for the first time in the analysis of the Ti/TiN process is a result of the fact that N_2 gas is excited in the process and most likely the excited species makes their way to the film surface.

G. TiN Film Growth

The final process step to be studied in detail is TiN film growth itself. In the fabrication of all TiN films, the underlying Ti films were deposited under identical conditions to identical thicknesses in order to ensure monolayer-level roughness on the Ti surface before switch-over to TiN growth. The identical conditions include a pressure of 10 mTorr, a plasma power of 100 W, and a pure Ar flow of 10 sccm. The target thickness of the Ti is in the range of 50-55 Å, which is the thickness at which coalescence to an ultra-smooth surface is possible (see Fig. 6). The ultimate situation is not quite ideal, however, because of the presence of the contaminant layers that develops at the Ti surface during the switch-over to TiN growth. In fact, Figs. 7-8 demonstrate that the monolayer level roughness region increases to a thickness of 20 Å

Quality of Fit to Data
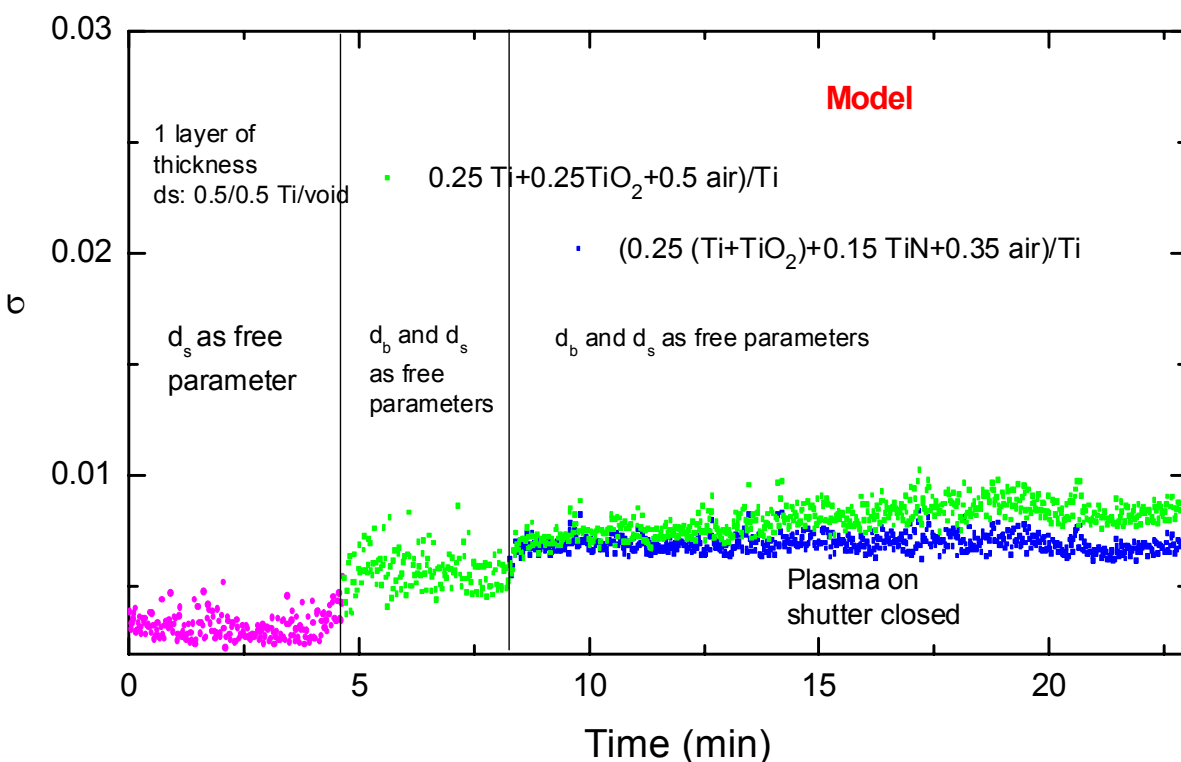
Fig. 20: Extended target nitridation is performed for improved compositional sensitivity to the surface layer that evolves. During an extended nitridation of the target, the interpretation of Fig. 8 is supported, namely, that the layer forming on the Ti surface is a low density, inhomogeneous mixture of an oxide and nitride.
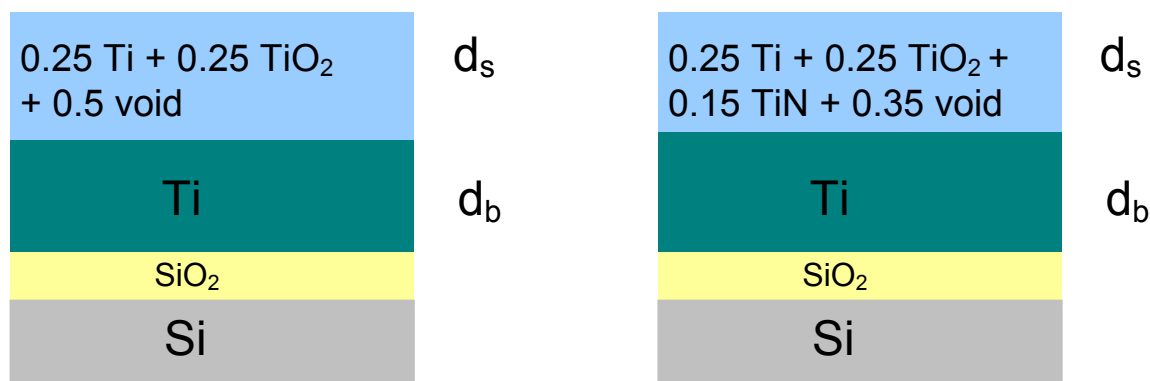
Fig. 21: Models used to describe the extended target nitridation data set of Fig. 20. (Left) low density inhomogeneous oxide with Ti thickness variation [quality of fit given by green (upper) points at right in Fig. 20]; (right) low density mixture of inhomogeneous oxide and nitride with Ti thickness variation [quality of fit given by blue (lower) points at right in Fig. 20].

during the switch-over from Ti film growth to TiN film growth. This problem is to be addressed in future research.

Figure 23 exhibits the evolution of the bulk layer thickness d_b, and the cluster and surface roughness thickness d_s during TiN growth on Ti/(120 Å SiO$_2$)/Si substrates, covering the mechanisms of TiN cluster formation, contact, and coalescence. For the series shown in Fig. 23, the sputtering plasma power was fixed at 300 W and the N$_2$ flow rate was fixed at 10 sccm. A variable N$_2$ pressure ranging from 5 to 15 mTorr was explored. The highest pressure of 15 mTorr led to smoothening of roughness originating from the substrate and complete coalescence to the smoothest surface among the three depositions. In fact, for the lowest pressure deposition, the surface roughness in the initial stage of growth builds up so that it becomes greater than that
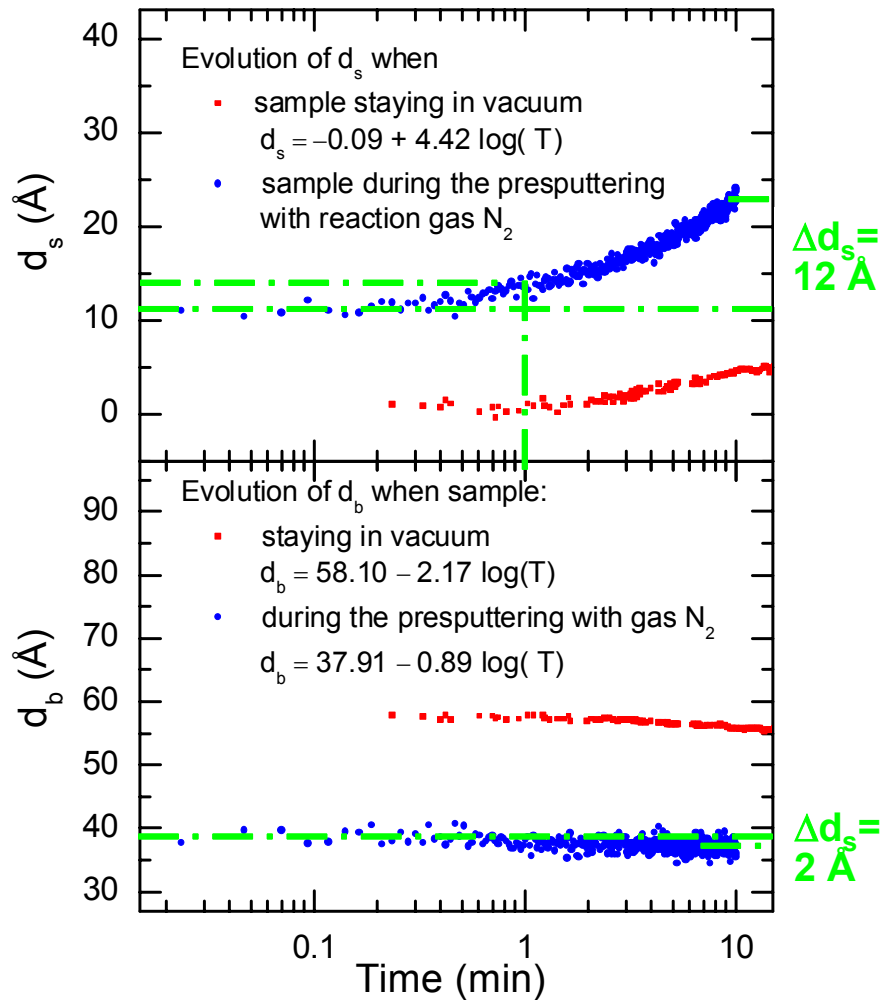
Fig. 22: Comparison of contamination rates of Ti under vacuum (10^{-6} Torr) and under extended target nitridation (10 mTorr, 10 sccm, 200 W). Under vacuum, the surface layer develops to 1 ML in a time of ~ 6 min. During target nitridation, the surface layer develops to 1 ML in a time of ~1 min. During target nitridation only a single monolayer of the underlying film is converted. In this case, the film grows through a deposition process as in the case of Ti target presputtering.
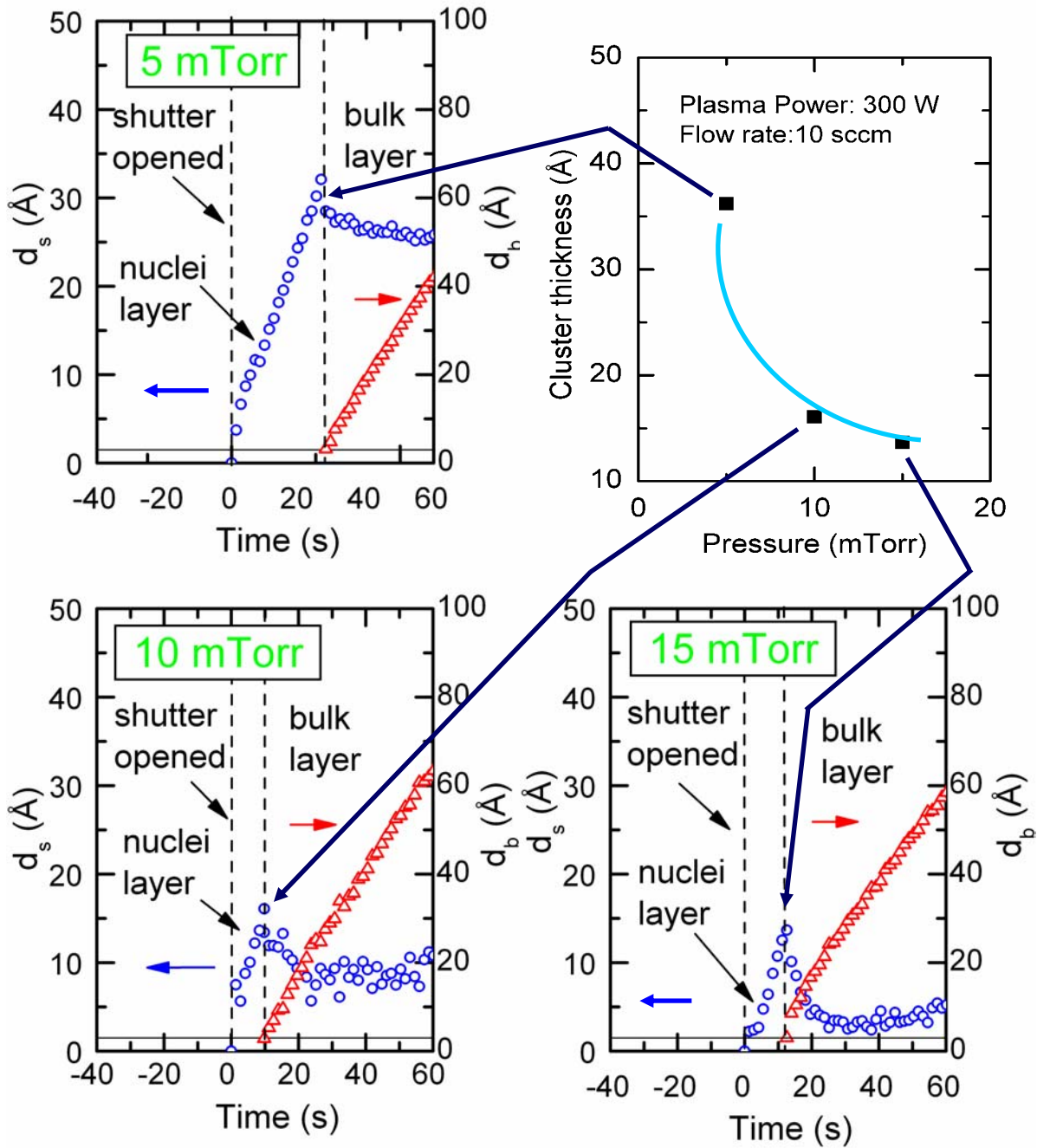
Fig. 23: Evolution of the bulk layer thickness d_b, and the cluster and surface roughness thickness d_s during TiN growth on Ti/(120 Å SiO$_2$)/Si substrates, focusing on TiN cluster formation, contact, and coalescence. The sputtering plasma power was fixed at 300 W and the N$_2$ flow rate was fixed at 10 sccm. A variable N$_2$ pressure ranging from 5 to 15 mTorr was explored. The highest pressure of 15 mTorr led to smoothening of substrate-induced roughness and complete coalescence to the smoothest surface among the three depositions.

Fig. 24: (Left) cluster thickness at the onset of bulk layer growth versus N_2 pressure; (lower right) effective thickness versus time; and (lower left) roughness layer thickness versus effective thickness, all for TiN films prepared at different N_2 pressures. Among the three films, maximum surface diffusion occurs at 15 mTorr. The TiN roughness that develops during target nitridation can be smoothened in a coalescence process. At lower pressures this roughness propagates due to the enhanced bombardment that leads to subsurface implantation. This bombardment leads to stable surface roughness layers, however.

on the starting substrate (~20 Å). Apparently the thick roughness layer is a substrate-induced effect, and growth under these conditions almost conformally covers the substrate, and even enhances the substrate roughness. In Figure 24, the following data sets are shown: (i) cluster thickness at the onset of bulk layer growth versus N_2 pressure; (ii) effective thickness versus time; and (iii) roughness layer thickness versus effective thickness, all for the TiN film series prepared at different N_2 pressures. Enhanced surface diffusion occurs as the pressure is increased to 15 mTorr and possibly beyond. As a result, roughness associated with the low density layer, consisting of a mixture of inhomogeneous oxide and nitride that develops during target nitridation, can be smoothened in a coalescence process. At lower pressures this roughness propagates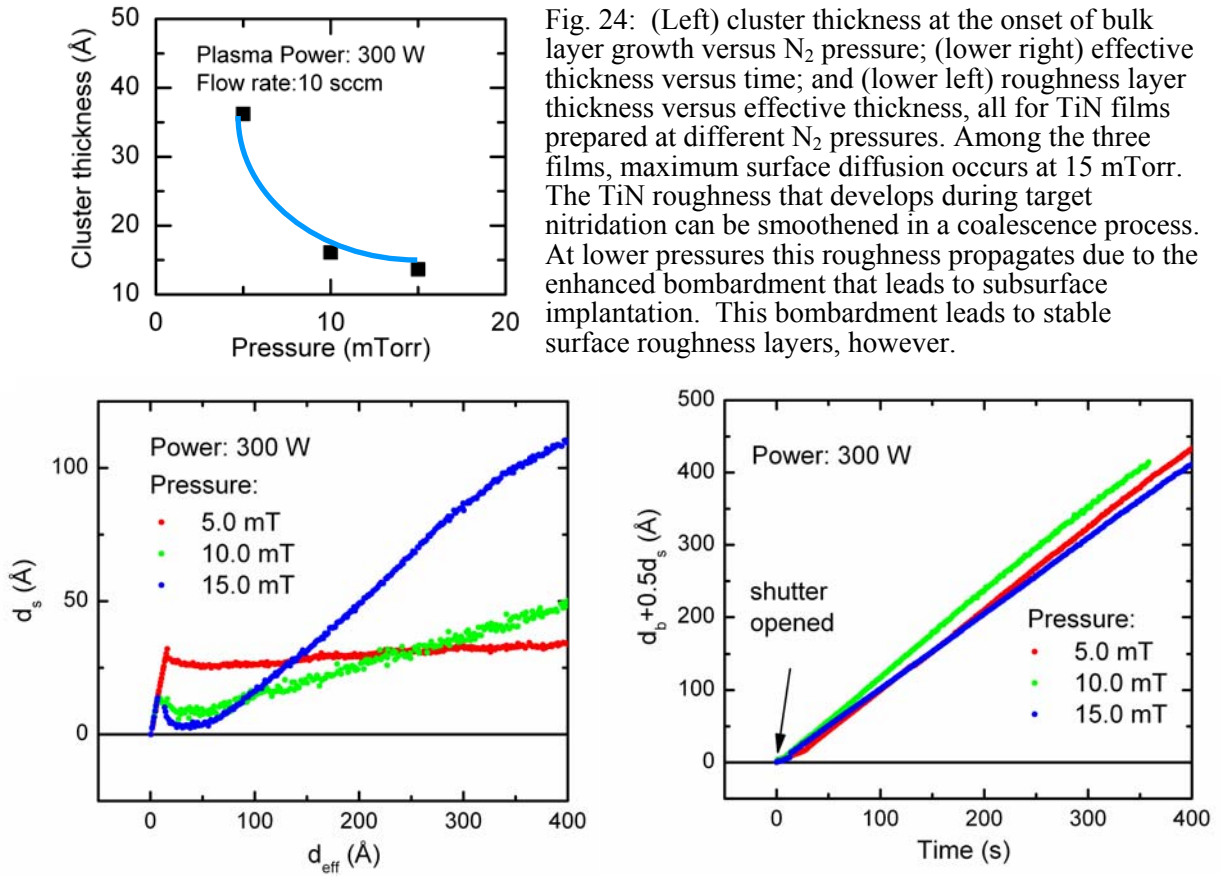 due to the enhanced bombardment that leads to subsurface implantation. This bombardment can be advantageous in the long run in that it leads to stable surface roughness layers in the later stages of film growth.

Figure 25 shows the dielectric functions for the three films of the TiN deposition series in which the N_2 pressure was varied from 5 to 15 mTorr at fixed plasma power (300 W) and N_2 flow rate (10 sccm). In general, the overall amplitude of ε_2 decreases when the void volume fraction increases, and this fact allows one to estimate the relative void fractions of deposited films simply by inspection. These results show that the TiN film density decreases monotonically with increasing pressure so that the highest density film is obtained at the lowest pressure. In fact, the void densities are quite high, 020 and 0.25, for the two higher pressure films relative to that of

the two low pressure ones. The interband absorption feature (~3.6 eV) that leads to preferential absorption toward the blue side of the spectrum (and hence a "gold" film in reflection) is broadened at the lowest pressure indicating a reduction in grain size, due to effects of ion bombardment.
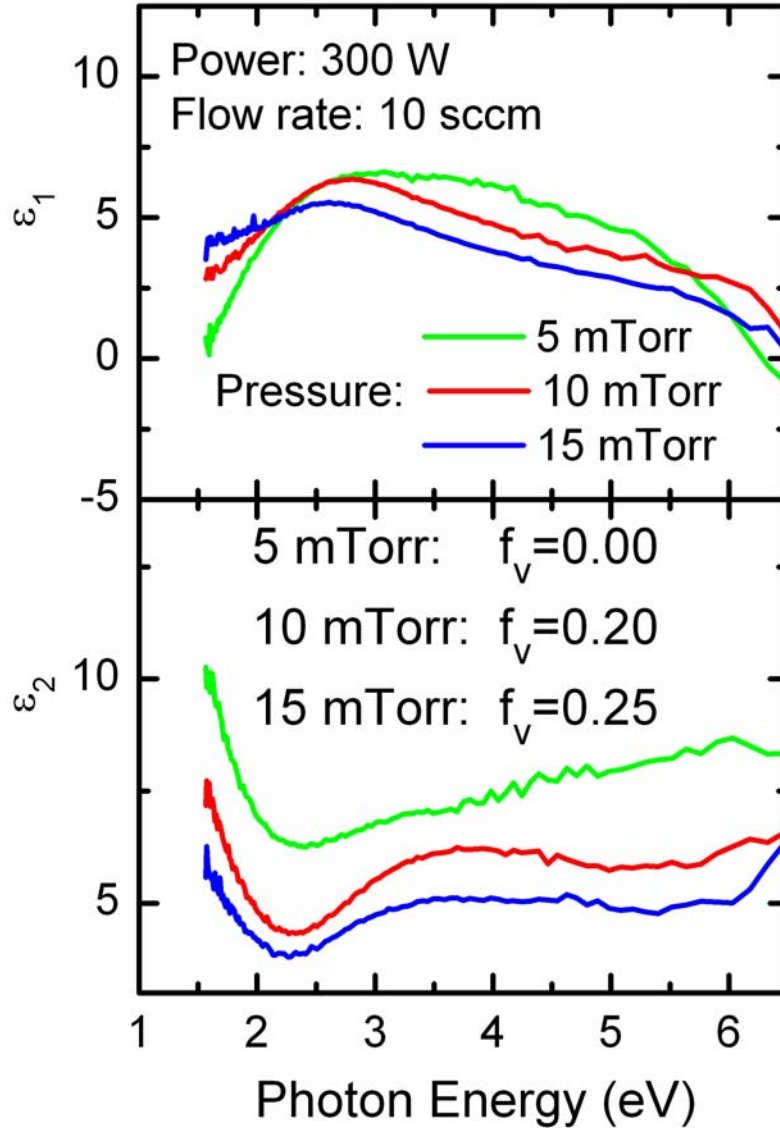
Fig. 25: Dielectric functions for the TiN deposition series in which the N_2 pressure was varied from 5 to 15 mTorr at fixed plasma power (300 W) and N_2 flow rate (10 sccm). These results show that the TiN film density decreases monotonically with increasing pressure so that the highest density film is obtained at the lowest pressure. The interband absorption feature (~3.6 eV) is broadened at the lowest pressure indicating a reduction in grain size due to effects of ion bombardment.

TiN depositions

Fig. 26: Evolution of the bulk layer thickness d_b, and the cluster and surface roughness thickness d_s during TiN growth on Ti/(120 Å SiO$_2$)/Si substrates, including TiN cluster formation, contact, and coalescence. The N$_2$ pressure was fixed at 10 mTorr and the N$_2$ flow rate was fixed at 10 sccm. A variable sputtering plasma power ranging from 200 to 400 W was explored. There is an optimum power associated with an optimum smoothening of the substrate-induced roughness as well as coalescence of the TiN film structure.
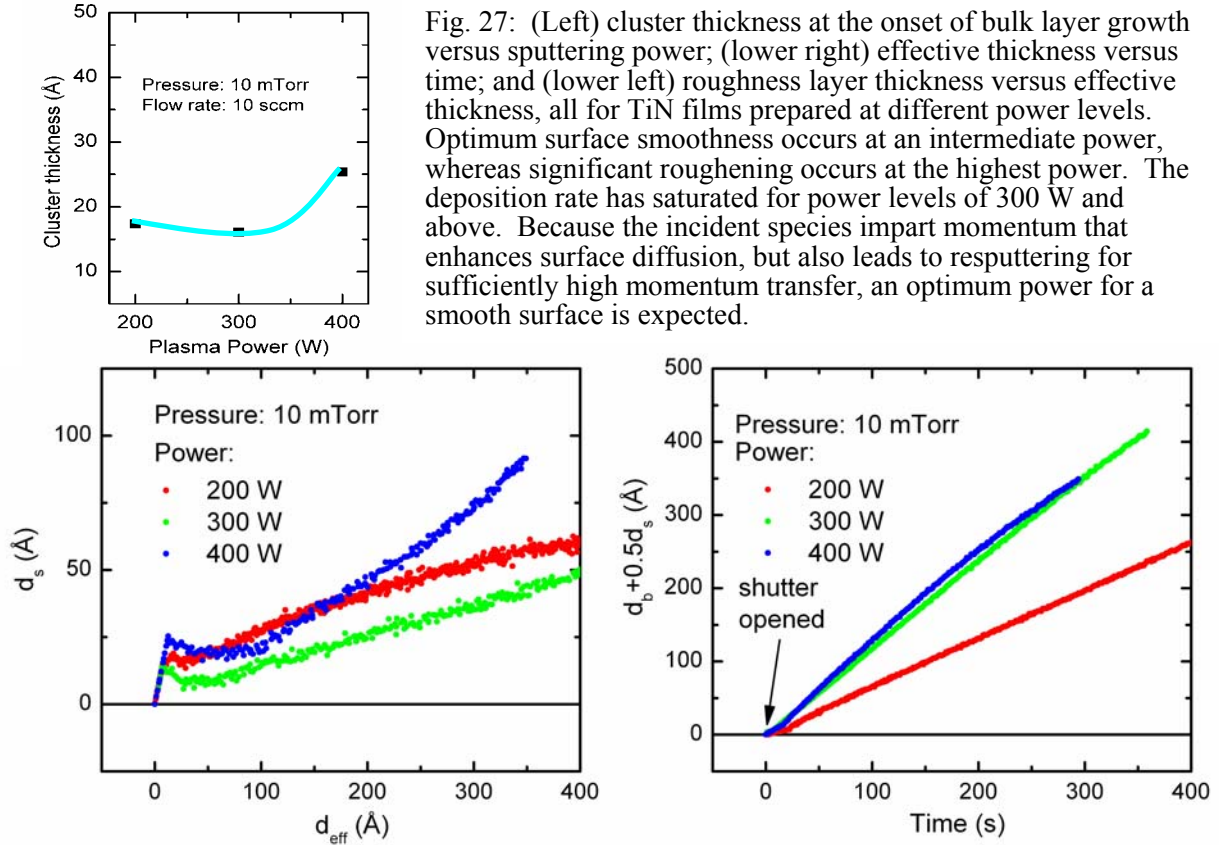
Fig. 27: (Left) cluster thickness at the onset of bulk layer growth versus sputtering power; (lower right) effective thickness versus time; and (lower left) roughness layer thickness versus effective thickness, all for TiN films prepared at different power levels. Optimum surface smoothness occurs at an intermediate power, whereas significant roughening occurs at the highest power. The deposition rate has saturated for power levels of 300 W and above. Because the incident species impart momentum that enhances surface diffusion, but also leads to resputtering for sufficiently high momentum transfer, an optimum power for a smooth surface is expected.
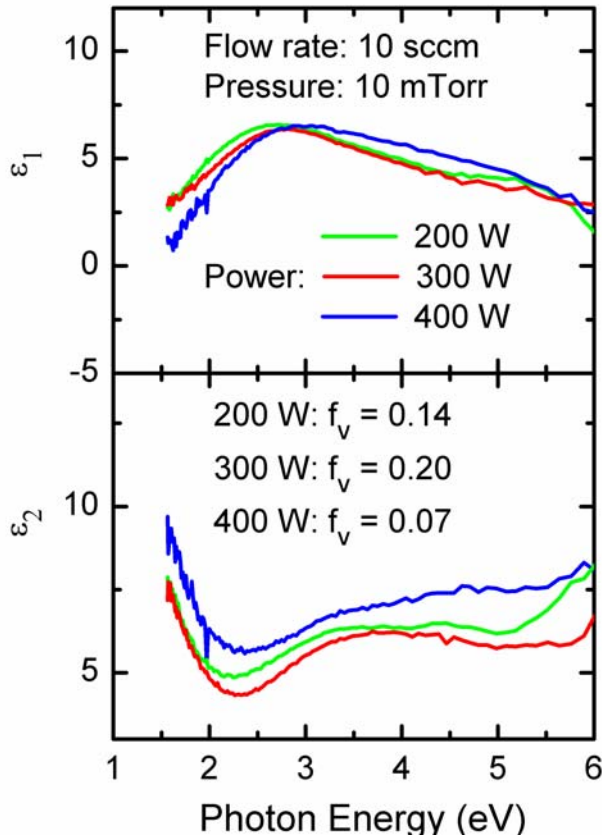
Fig. 28: Dielectric functions for the TiN deposition series in which the sputtering power was varied from 200 to 400 W at fixed N_2 pressure (10 mTorr) and fixed N_2 flow rate (10 sccm). These results show that the film deposited with the highest power has the highest bulk layer density (highest ε_2 amplitude). The film deposited with the highest power shows the highest degree of disorder due to the broader feature in ε_2 near 3.6 eV. This film also shows the most extensive roughening after coalescence (see Fig. 27).

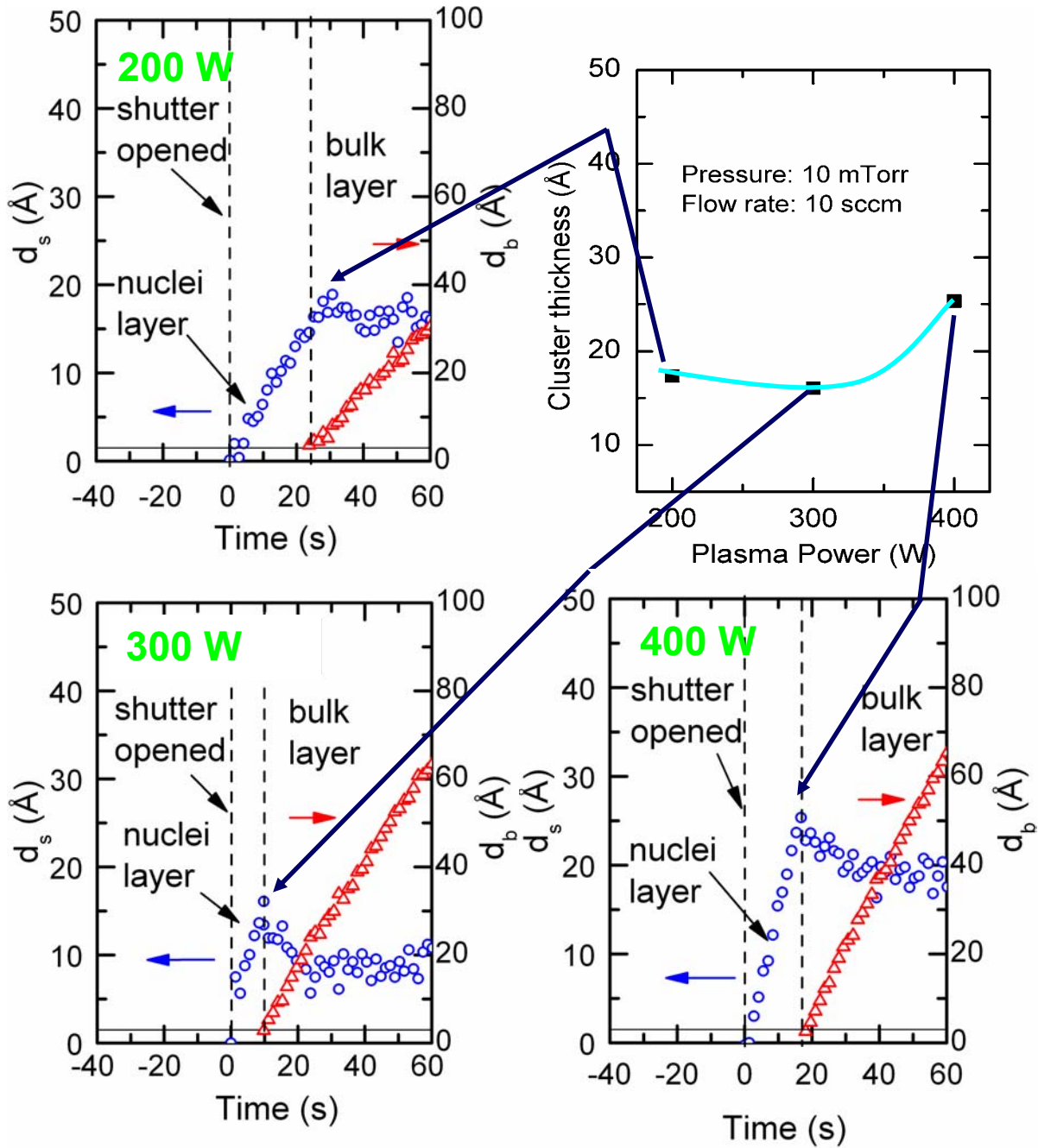Figure 26 exhibits the evolution of the bulk layer thickness d_b, and the cluster and surface roughness thickness d_s during TiN growth on Ti/(120 Å SiO$_2$)/Si substrates, depicting the mechanisms of TiN cluster formation, contact, and coalescence. For the series shown in Fig. 26, a variable sputtering plasma power ranging from 200 to 400 W was explored while the N$_2$ pressure was fixed at 10 mTorr and the N$_2$ flow rate was fixed at 10 sccm. The intermediate power level of 300 W led to an optimum smoothening of the substrate roughness as well as coalescence of the TiN film structure. The surface roughness after coalescence, at a bulk layer thickness of 50 Å amounts to ~9 Å.

In Figure 27, the following data sets are shown for TiN deposition: (i) cluster thickness at the onset of bulk layer growth; (ii) effective thickness versus time; and (iii) roughness layer thickness versus effective thickness, all for the TiN film series prepared at the different plasma power levels. Enhanced surface diffusion appears to occur as the power is increased from 200 to 300 W; however, above 300W it is clear that such an effect is reversed. The underlying low density layer on the Ti surface, consisting of a mixture of inhomogeneous oxide and nitride that develops during target nitridation, induces roughness on the nucleating TiN film that can be smoothened in a coalescence process. The magnitude of this effect, which is evident by the peak height in d_s in the initial stages of growth, correlates well with the smoothening effect achieved through coalescence at times just greater than that at which the peak occurs. This correlation is evidence that surface diffusion drives the smoothening of substrate and nucleation induced roughness, and that surface diffusion is optimized at the intermediate power level. Because the incident species impart momentum that enhances surface diffusion, but may also lead to resputtering for sufficiently high momentum transfer, an optimum power for a smooth surface is expected. This concept is supported by the observation in Fig. 27 that the deposition rate has saturated for power levels of 300 W and above.

Figure 28 shows dielectric functions of the TiN depositions in which the sputtering power was varied from 200 to 400 W at fixed N$_2$ pressure (10 mTorr) and fixed N$_2$ flow rate (10 sccm). These results show that the film deposited with the highest power has the highest bulk layer density (highest ε_2 amplitude). This film also shows the highest degree of disorder as noted by the broader feature in ε_2 near 3.6 eV, and also shows the most extensive roughening after coalescence (see Fig. 27). In contrast, the 300 W film that shows the largest surface diffusion characteristic and smoothest surface also leads to the lowest bulk density. Possibly a larger grain size in these films is associated with a larger grain boundary void component.

Figure 29 show the results of best fits to the real and imaginary parts of the dielectric functions of the TiN films of the pressure series using intraband (Drude) and interband components. The Drude term in the complex dielectric function gives rise to the decrease in ε_1 and the increase in ε_2 with decreasing energy. Fitting this term, given by $\varepsilon(E) = A_D^2/[E^2 - i\Gamma_D E]$, can provide a measure of connectivity for the TiN, even for ultrathin films. In fact, the dc resistivity of the TiN is given by the expression $\rho = (1/\varepsilon_{fs}^2)(\Gamma_D/A_D^2)$, where ε_{fs} is the dielectric permittivity of free space, Γ_D is the broadening parameter, and A_D is the amplitude factor. Figure 30 depicts the parameters that describe the interband transitions for three films of TiN prepared at different pressures. These parameters define a single Tauc-Lorentz oscillator and include (from top to bottom) the (i) amplitude factor or oscillator strength A, (ii) broadening parameter Γ, (iii)
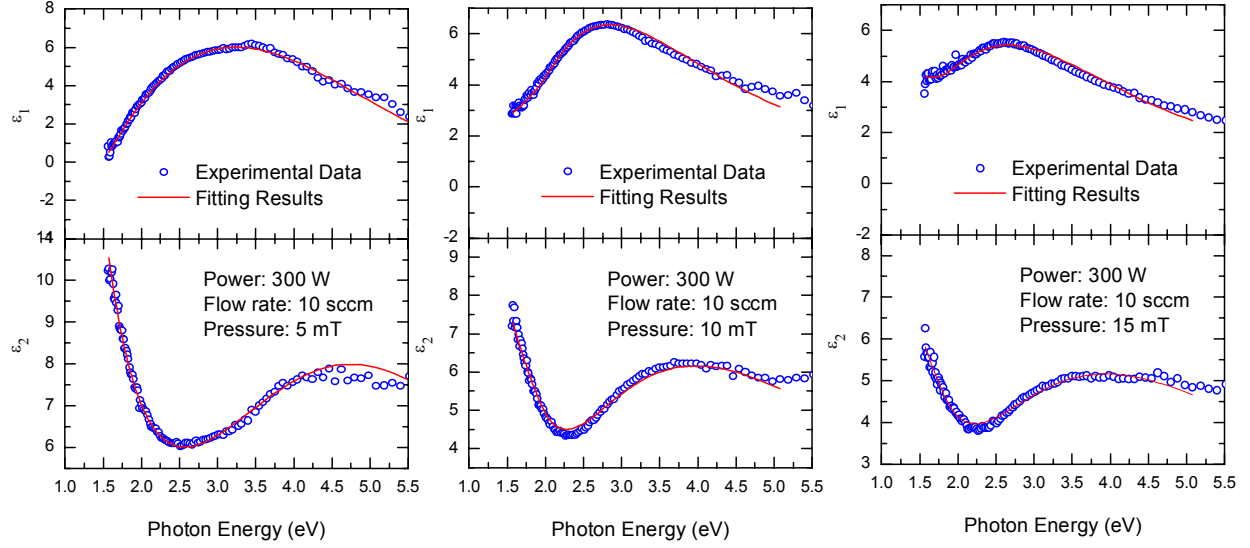
Fig. 29: Analysis of real and imaginary parts of the dielectric function using Drude and interband components. The Drude term in the complex dielectric function gives rise to the decrease in ε_1 and the increase in ε_2 with decreasing energy. Fitting the Drude term $\varepsilon(E) = A_D^2/[\omega^2 - i\Gamma_D\omega]$ can provide the dc resistivity of the TiN according to the expression $\rho = (1/\varepsilon_{fs}^2)(\Gamma_D/A_D^2)$.
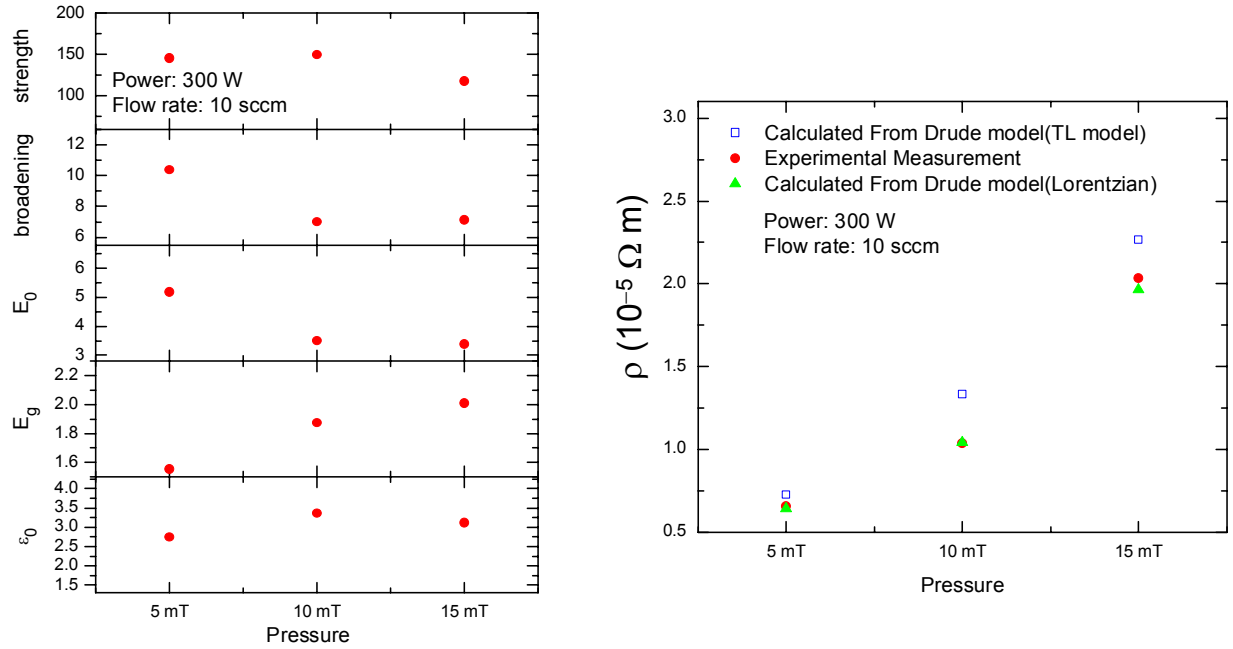
Fig. 30: (Left) parameters that describe the interband transition for three samples of TiN prepared at different pressures, including (top to bottom) the (i) oscillator strength A, (ii) broadening parameter Γ, (iii) resonance energy E_0, (iv) absorption onset E_g, and (v) dielectric constant ε_0. The first four parameters are in units of eV. (Right) resistivity for the same three films measured optically using the fits of Fig. 29 (blue squares), measured optically using similar fits with a different interband model (green triangles), and measured directly using electrical probes (red circles).
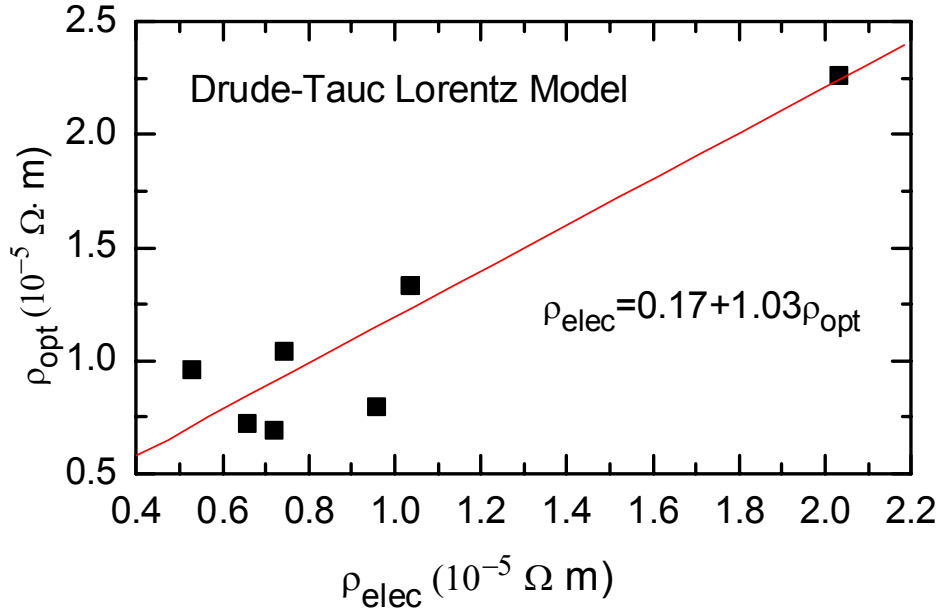
Fig. 31: Correlation of the TiN electrical resistivity measured optically with that measured electrically. Although there is considerable scatter between the optical result (ρ_{opt}) and the electrical result (ρ_{elec}), the correlation between the two shows a near unity slope and a near zero intercept.
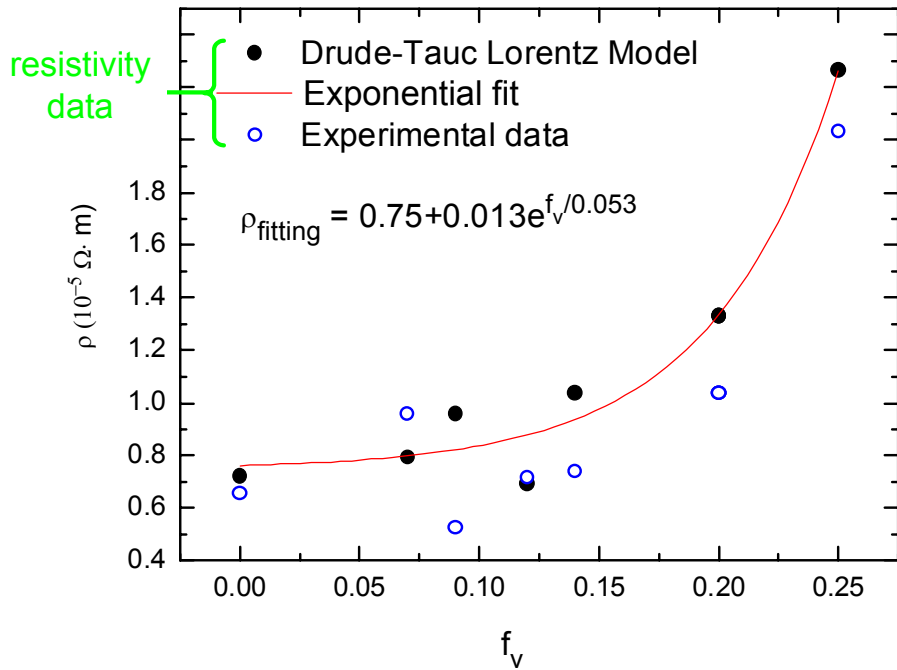
Fig. 32: Correlation of resistivity with void volume fraction, both determined optically (solid circles), and with resistivity determined electrically (open circles). Apparently voids have a detrimental effect on the electrical conductivity possibly through scattering centers or through columnar structure that disrupts in-plane carrier transport. These results show that in-plane conductivity can be used as a tool to optimize film microstructure for TiN.

resonance energy E_0, (iv) absorption onset E_g, and (v) dielectric constant ε_0. The first four parameters are in units of eV. Also shown in Fig. 30 is the resistivity for the same three films calculated from optical parameters using the best fits of Fig. 29 and also using similar fits, but with a different interband model consisting of two Lorentz oscillators. Finally, the results of direct electrical measurements of resistivity are also included in Fig. 30, and these are in good agreement with the optical measurements.

Figure 31 shows the final correlation of the TiN electrical resistivity measured optically with that measured electrically. The TiN sample set includes the pressure and power series described above, along with a N_2 gas flow series in which pressure and power were fixed at 10 mTorr and 300 W, and the flows were set at 10, 30, and 40 sccm. In all cases, the single Tauc-Lorentz oscillator is used to describe the interband transition, as this provides the best overall fits. Although there is considerable scatter between the optical result (ρ_{opt}) and the electrical result (ρ_{elec}), the correlation between the two shows a near unity slope and a near zero intercept.

Fig. 33: Results for the evolution of the surface roughness layer thickness d_s versus the bulk layer thickness d_b during multistep processing. The deposition is initiated using 300 W plasma power, 15 mTorr N_2 pressure, and 10 sccm N_2 flow. At the first vertical line, the N_2 pressure is reduced to 5 mTorr for long term surface smoothness. Finally, the pressure is increased to 7 mTorr for increased plasma stability. The results of this study include (i) the smoothest surface yet observed for a 475 Å thick film, specifically a surface having 18 Å of roughness, and (ii) the largest cluster size yet observed 51 Å, which is close to that desired for TiN/SiN_x nanocomposites.

Thus, these results suggest that it is promising to be able to extract the electrical characteristics of the TiN in a contactless manner from in situ measurements. Another interesting correlation is shown in Figure 32 between void volume fraction and resistivity, the latter determined either optically or electrically. The fact that the correlation is best for the all-optical analysis suggests that the electrical measurement may have random scatter related to the nature of the contacts. Figure 32 suggests that voids have a detrimental effect on the electrical conductivity possibly through scattering centers or through columnar structure that disrupts in-plane carrier transport. These results also suggest that in-plane conductivity can be used as a tool to optimize film microstructure for TiN.

A final study explores the possibility of using two-step processes to control the cluster size and the final TiN surface roughness. The largest initial TiN cluster size achieved to date in a single step process is ~ 30 Å, and the smoothest final surface after 400 Å of bulk layer thickness is ~30-35 Å. As an example of control that can be achieved in multistep processing,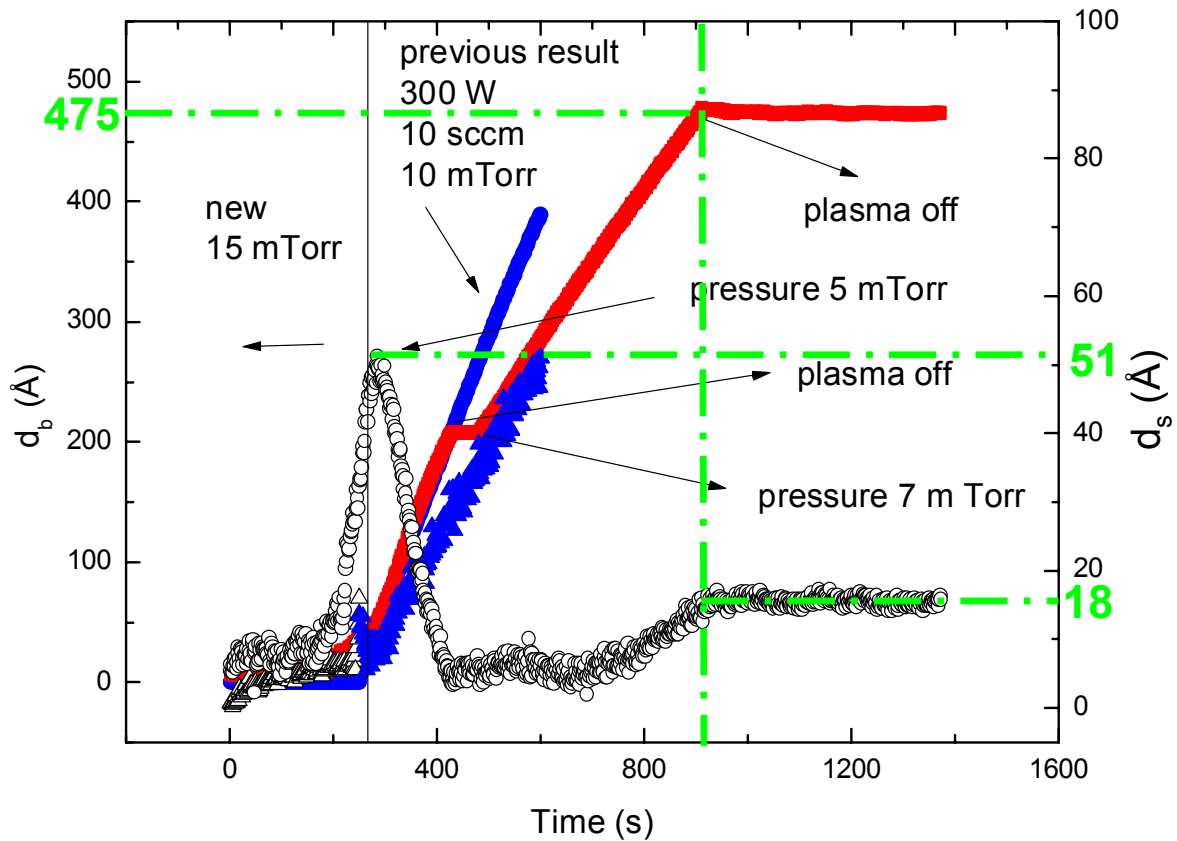 Fig. 33 shows results for the evolution of the surface roughness layer thickness d_s versus the bulk layer thickness d_b during a process that is initiated using 300 W plasma power, 15 mTorr N_2 pressure, and 10 sccm N_2 flow. This process smoothens out the substrate roughness in the initial stages. During the nucleation, however, the N_2 pressure is reduced to 5 mTorr for enhancement of clustering and for long term surface smoothness. Finally, the pressure is increased to 7 mTorr for increased plasma stability. The TiN film fabricated in this study exhibits (i) the smoothest surface yet observed for a 400 Å thick film, specifically having 8 Å roughness (and for a 475 Å thick film, 18 Å surface roughness), and (ii) the largest cluster size yet observed 51 Å, which is close to that desired for TiN/SiN$_x$ nanocomposites.

<u>TiN Film Growth Summary</u>

The observations made during the growth of TiN films show features common to those made during Ti growth. First, immediate roughness development and evolution is observed at the lowest pressures, whereas nucleation and coalescence to smooth surfaces are observed under conditions of moderated ion bombardment. In addition, long term stability of surfaces at low pressures is noted, whereas significant instability occurs at high pressures. TiN clusters ~15-50 Å in size can be obtained in one and two step processes, and these may be suitable for formation of controlled nanocomposite structures. Finally, atomically smooth TiN films having thicknesses in the range of ~ 20 - 50 Å can be obtained at elevated pressures for incorporation into coherent multilayer structures.

H. Comparisons with Atomic Force Microscopy

Throughout the Ti/TiN deposition process in Figs. 5-9, the surface roughness evolution has been tracked. In fact, there is a general increase in roughness from the SiO$_2$/Si substrate starting with Ti target presputtering, and proceeding with Ti film growth, Ar to N_2 gas switching, target nitridation, and ending with TiN film growth. It is of interest to compare the roughness values obtained optically at the end of various steps with those obtained by atomic force microscopy after removing the same sample from the chamber. This provides additional insight into what the real time spectroscopic ellipsometry (RTSE) is actually measuring.

Figure 34 (top) provides an atomic force microscopy (AFM) image after the third and fourth steps, namely Ar gas removal and N_2 gas initiation, but with an extended N_2 gas flow period to enhance the roughness. After these steps, RTSE yields a roughness thickness of d_s = 12 Å, and
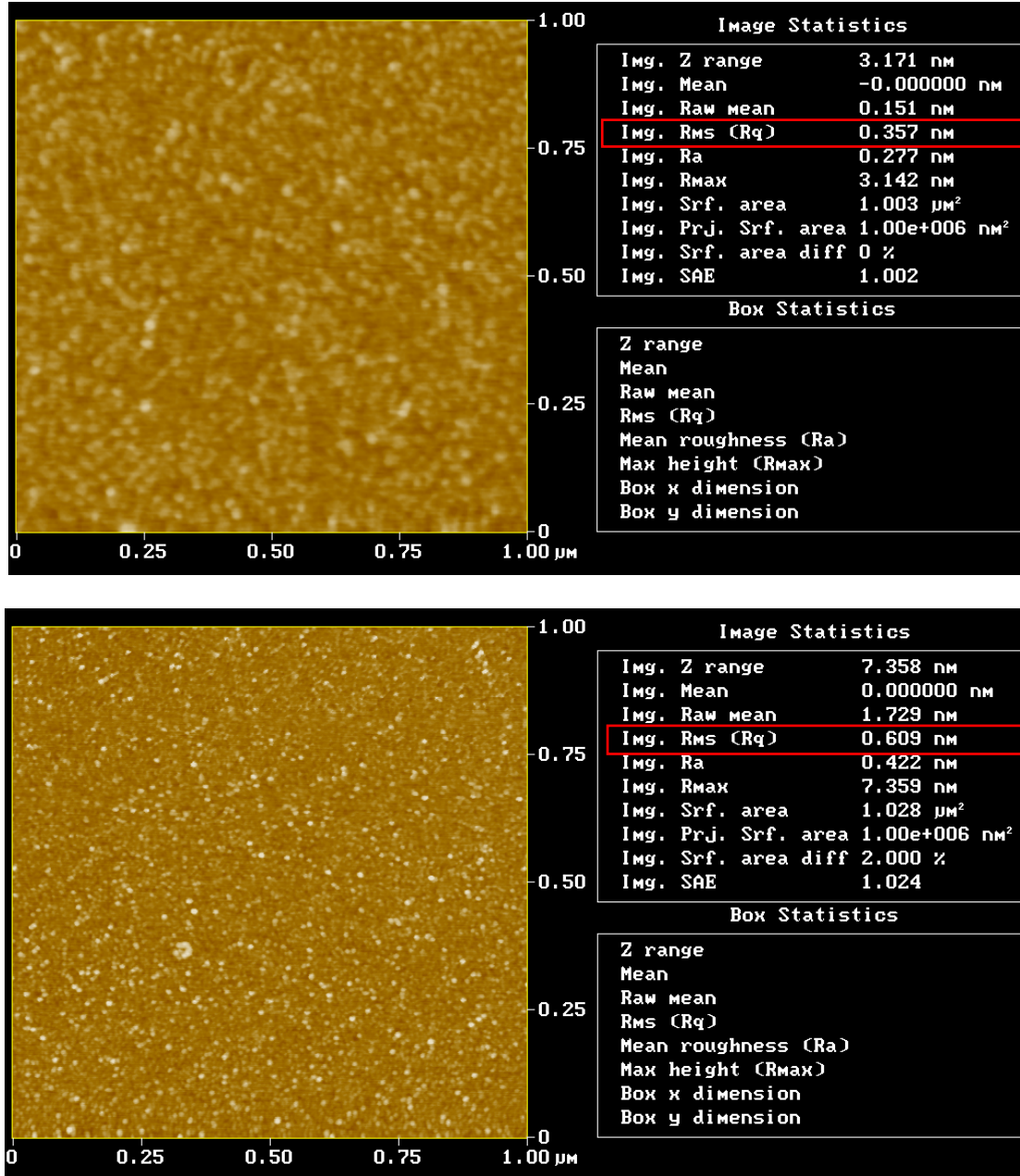
Fig. 34: (Top) atomic force microscopy image after the third and fourth steps, namely Ar gas removal and N_2 gas initiation, but with an extended N_2 gas flow period. After these steps, RTSE yields a roughness thickness of d_s = 12 Å, and the AFM root-mean-square roughness is given by d_{rms} = 3.6 Å. (Bottom) atomic force microscopy image after the fifth step, namely target nitridation. After this step, RTSE yields a roughness thickness of d_s = 23 Å, and the AFM root-mean-square roughness is given by d_{rms} = 6 Å.

the AFM root-mean-square roughness is given by $d_{rms} = 3.6$ Å. Figure 34 (bottom) presents an AFM image after the fifth step, namely target nitridation. After this step, RTSE yields a roughness thickness of $d_s = 23$ Å, and the AFM root-mean-square roughness is given by $d_{rms} = 6$ Å. Figure 35 provides an AFM image after the sixth step, TiN growth. The top image is
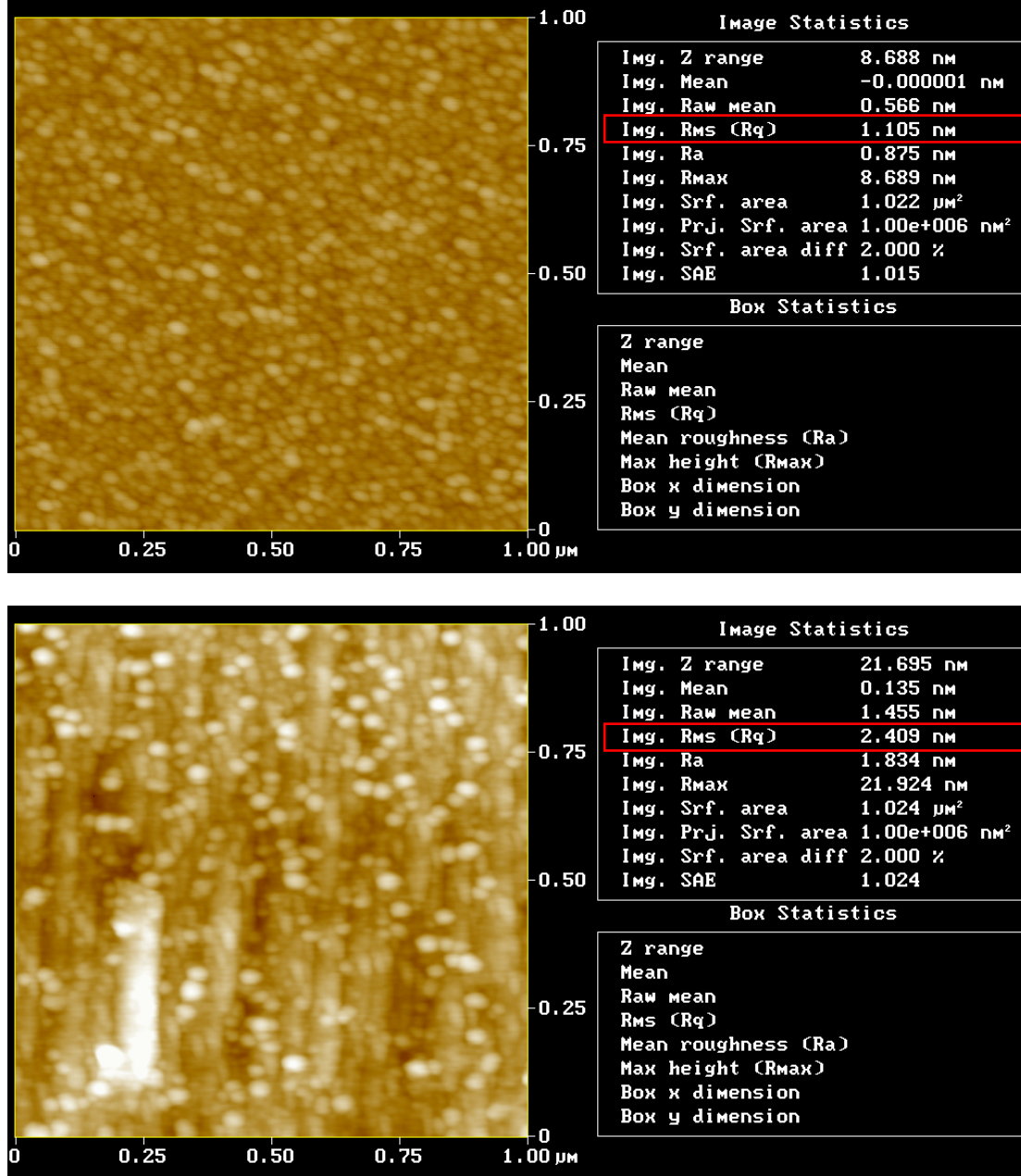
Fig. 35: Atomic force microscopy image after the sixth step, TiN growth. The top image is obtained just after nuclei coalescence in which case RTSE yields a roughness thickness of $d_s = 16$ Å, and the AFM root-mean-square roughness is given by $d_{rms} = 11$ Å. The bottom image is obtained after the growth of a thick TiN film in which case RTSE yields a roughness thickness of $d_s = 41$ Å, and the AFM root-mean-square roughness is given by $d_{rms} = 24$ Å.

obtained just after nuclei coalescence, in which case RTSE yields a roughness thickness of $d_s =$ 16 Å, and the AFM root-mean-square roughness is given by $d_{rms} = 11$ Å. The bottom image is obtained after the growth of a thick TiN film in which case RTSE yields a roughness thickness of $d_s = 41$ Å, and the AFM root-mean-square roughness is given by $d_{rms} = 24$ Å.

Figure 36 presents the correlation between ellipsometry and AFM obtained from results shown in Figs. 34 and 35. The two points on the curve indicated by $d_s = 1.66\ d_{rms}$ correspond to roughness on the actual TiN thin films. A similar relationship of $d_s = 1.5\ d_{rms}$ has been observed previously for a large set of amorphous silicon films. Both such relationships arise from the fact that the surface roughness deduced optically is approximately midway between rms and peak-to-peak AFM values when the AFM is obtained from images on the order of a micron square. The two points at the left of Fig. 36 exhibit different behavior. These were taken on the inhomogeneous surfaces that form during N_2 flow and target nitridation. In this case, the voids detected optically and considered as part of roughness may actually be embedded in a bulk-like film, and this may account for an apparent overestimate of the surface roughness by ellipsometry. In contrast, for the homogeneous TiN thin films there will be a clear distinction between surface roughness and bulk. As an alternative explanation, the roughness on the inhomogeneous surfaces that form during N_2 flow and target nitridation may have an in-plane scale below the AFM resolution. This is reasonable because the layers that generate this roughness are so thin. Thus, the AFM provides an underestimate of the true roughness. The AFM does not underestimate the roughness after the TiN deposition because these films are thicker and have established a larger in-plane scale due to the structural coarsening with thickness.
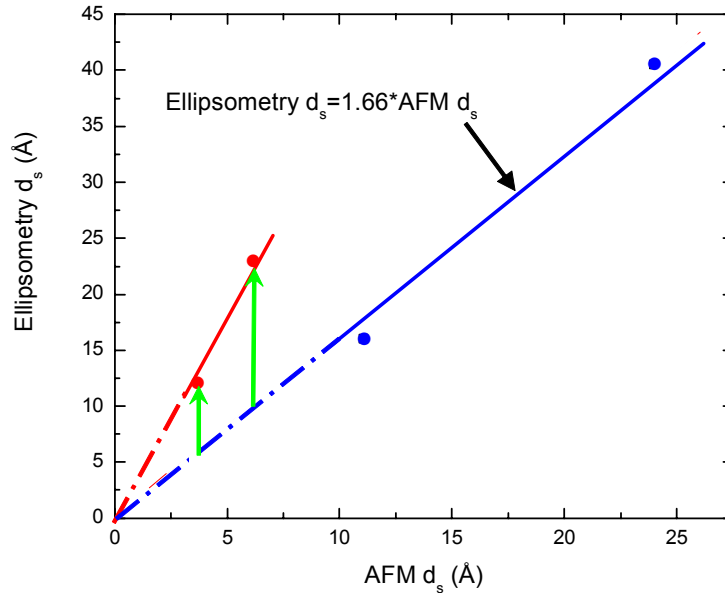
Fig. 36:   The correlation between ellipsometry and AFM obtained from results shown in Figs. 34 and 35. The two blue points on the curve indicated by $d_s = 1.66\ d_{rms}$ were obtained on TiN thin films in which there is a clear distinction between surface roughness and bulk. The two red points at the left were taken on inhomogeneous surfaces formed during N_2 flow and target nitridation. In this case, the voids detected and considered as part of roughness may actually be embedded in a bulk-like film, and this may account for an apparent overestimate of the surface roughness by ellipsometry.

**NORTH DAKOTA STATE UNIVERSITY
CENTER FOR NANOSCALE SCIENCE AND TECHNOLOGY**

NANOSTRUCTURED PROTECTIVE COATINGS PROGRAM – PHASE I

INTERNAL REPORT

TASK 2: SURVEY ON METHODS FOR TESTING AND
EVALUATION OF WEAR RESISTANT COATINGS

Team members:
      Dr. Valery Marinov — Industrial & Manufacturing Engineering
      Dr. Wayne Reitz — Mechanical Engineering
      Arun Shankaran (GRA) — Industrial & Manufacturing Engineering
      Crystal Barr (UGRA) — Mechanical Engineering

Submitted by:
      Dr. Valery Marinov – Lead researcher

December 2003

Contents

Background

This team has been tasked to survey the currently used industrial and military methods for testing and evaluation of tribological coatings. The scope of this study constitutes Task 2 from the Research Plan for Phase I of the Nanostructured Protective Coatings (NPC) Program recently launched in the NDSU Center for Nanoscale Science and Engineering (CNSE). Details about the NPC program, including program description, objectives, timeline and budget are available elsewhere[1].

To achieve the objectives of this effort (for the research objectives see *Section 1.3*), the team agreed on the following three-step procedure,
  (i)   identification of the research subject
 (ii)   information compilation
(iii)   information processing and recommendations

The first step included selection and definition of the coating attributes of interest for this study, and is described in *Section 1.2*. The methodology for information compilation and the processing procedures are outlined in *Section 2*. The recommended methods and procedures are included in *Section 3*. In this document, there is no list of references at the end of the text, instead, the list of the standards, research papers, reference books and all other relevant sources of information used in the preparation of this report has been included in a number of sectional *Reference* sections, as explained in *Section 3.1* below.

1.1   Scope

The scope of this study has been restricted by definition only to the measurement, testing and evaluation of coatings attributes. Two of the more important factors that will limit the scope of the survey need to be also considered, *viz.*, the coatings type and structure, and the application areas for the coatings. The types of coatings that will be a subject of the NPC program are explained in the project proposal[1] and in some other relevant documents. For the application area, the list of applications in which the team believes that the U.S. Air Force will be mostly interested would include tribological coatings for...
- High-speed/high-temperature bearings
- Compressor blades
- Substitutes for lubricant-free friction systems
- Tooling for metal, polymer, and composite materials manufacturing

Another important consideration is the coating thickness. Thin-film and thick-film coatings differ not only in their properties, behavior and deposition techniques; they also require different characterization methods. This study considers coatings with thickness within the range of 5 to 25 μm. For some coating systems and deposition methods, the lower limit might be 1 μm whereas

---

[1] Nanostructured Protective Coatings. Proposal to the United States Air Force Research Laboratory – Materials and Manufacturing Directorate. Submitted by G.J. McCarthy, Program Manager and Director CNSE, NDSU, 2003.

4

for some other systems such as the multilayer coatings or the nanocomposite systems the maximum thickness could be up to 50 μm and more.

1.2 Coating attributes

At the beginning of this research effort, the team selected a number of characteristics and properties (referred here to as *coating attributes*) which were used as a starting point in the survey of the testing and evaluation procedures. It was agreed that the list might be extended to include many more attributes of the thin-film and thick-film coatings and that it would be much more extensive if the substrate parameters, which affect directly or indirectly the characteristics and behavior of the coating, were also included. The most important coating attributes are broadly classified into three general areas (*Table 1*),

(i) physical
(ii) mechanical
(iii) tribological

Table 1. Coating Attributes

Physical	Mechanical	Tribological
Surface finish	Hardness	Resistance to abrasive wear
Thickness	Residual stress	Resistance to particle erosion
Coating/substrate adhesion	Intrinsic mechanical properties: modulus of elasticity fracture resistance	Resistance to sliding (adhesive) wear
	Dynamic properties: fatigue	Coefficient of friction

In this study, this is considered a generic list of coatings attributes that is not application dependent. Since different applications put different demands on the coatings, the most decisive parameters will vary from one situation to another. Various applications may or may not add or remove attributes from the list of attributes. Therefore, for a more in-depth application-oriented tribological research, a different subset of the coatings attributes needs to be generated. It is also acknowledged that both the application list in *Section 1.1* and the coatings attributes list in *Table 1* may and most probably will be modified throughout this project to accommodate the current needs and capabilities.

1.3 Objectives

The objective of this study is to analyze the currently used methods for measurement, testing and evaluation of wear resistant (tribological) coatings, and to recommend the most appropriate for a particular application (see *Section 1.1*) suite of methods for testing and evaluation of a selected set of coating attributes (listed in *Table 1*).

5

2 Methodology

2.1   Data compilation

The procedures for compiling and processing the relevant information followed the methods of the traditional literature survey study. Various sources of information were used for the information compilation, including but not limited to ...

Journals
       Advanced Materials and Processes
       Journal of Adhesion Science and Technology
       Journal of Coatings Technology
       Journal of Engineering Materials and Technology
       Journal of Material Science
       Journal of Tribology
       Materials and Manufacturing Processes
       Surface Coatings Technology
       Surface Engineering
       Thin Solid Films
       Tribology International
       Tribology Letters
       Wear

Reference Books:
       ASTM Handbook – Volume 02.05: Metallic and Inorganic Coatings; Metal Powders, Sintered P/M Structural Parts
       ASTM Handbook – Volume 03.01: Metals – Mechanical Testing, Elevated and Low-Temperature Tests; Metallography
       ASTM Handbook – Volume 03.02: Wear and Erosion; Metal Corrosion
       ASTM Handbook – Volume 03.03: Nondestructive Testing
       ASTM Handbook – Volume 05.01: Petroleum Products and Lubricants (I)
       ASTM Handbook – Volume 05.02: Petroleum Products and Lubricants (II)
       ASM Handbook – Surface Engineering (Vol. 5)
       ASM Handbook – Mechanical Testing and Evaluation (Vol. 8)
       ASM Handbook – Friction, Lubrication and Wear Technology (Vol. 18)

Databases
       Compendex

Some of the keywords that were used for search in the *Compendex* database included:
- Protective coatings : 70 matches
- Engineered Coatings: 2 matches
- Industrial standards: 1 result
- Fracture: 158 matches

6

- Abrasion resistance: 143 matches

More keywords were later added to extend the search area, some of them were...

- Scratch
- Adhesion/adhesive wear
- Erosive wear
- Corrosion
- Thickness

- Nanostructured
- Nanoindentation

- PVD
- CVD
- Thin films

2.2 Data processing

The numerous publications and standards were refined at the end of this stage to better represent the research focus. The objective was to reduce the numerous methods currently applied in the academic and governmental laboratories and industry to a list of few most appropriate methods to measure, test and evaluate the coating attributes listed in *Table 1* under the limits and for the applications explained in *Section 1.1*. These recommendations will serve as a starting point in making decisions on tribological equipment acquisition during *Task 3* of the current project phase. The final results of this task are included in the next section of this document.

3   Recommended Methods and Procedures

3.1 Summary

Table 2 contains a brief summary of the recommended methods and procedures as well as the type of the equipment required. The same table is included also in *Appendix I*.

Table 2. Recommended methods and equipment

Parameter	Method		Equipment		Page
	Near-term	**Long-term**	**Near-term**	**Long-term**	
Abrasive wear	Micro-abrasive test		Ball Crater Apparatus		9
Adhesion	Scratch test		Micro-scratch tester		13
Erosive wear	ASTM G76-02		Gas blast apparatus		16
Fatigue	Spherical rolling test		Spherical rolling tester		19
Fracture strength	Four-point bend test		Four-point bend tester		22
Coefficient of friction	Tribometry	Scanning probe microscopy	Pin-on-disk Tribometer	Scanning probe microscope	24
Hardness	Micro-hardness test		Nanoindenter		26
Modulus of elasticity		Micro-indentation test		Nanoindenter	29
Residual stress	Deflection test	ASTM E2245-02	*Almen* strips & gauge	Optical interferometer	32
Sliding wear	Ball crater test		Ball Crater Apparatus		36

7

Surface finish	Optical profilometry		Optical profilometer		38
Thickness	Ball crater test	ASTM B 487-85	Ball Crater Apparatus	SEM	41

3.2   Introduction

The parts of this section were arranged alphabetically to represent the coating parameters in *Table 1*, and were structured in the following order,

- Definition of the coating parameter
- Available standard methods for testing and evaluation
- Other methods. This includes methods which are not formally standardized but have been successfully implemented and, in most cases, widely adopted by the research community and practitioners
- Recommended method for testing and evaluation. The recommended method section has been divided into two parts, the first one specifying the near-term, low-cost solution, which would require limited resources and would be available for an immediate implementation, whereas the second one, referred here to as a "long-term" solution, represents the state-of-art in this particular method. Note that for most coating attributes both methods coincide. APPENDIX II includes full text copies of the recommended standards.
- References. Includes the list of all relevant reference materials used in the preparation of the above sections.

3.3   Abrasive wear

3.3.1   Definition

Abrasive wear, as defined by ASTM, "*is due to hard particles or hard protuberances that are forced against and move along a solid surface*". Wear, in turn, is defined as "damage to a solid surface that generally involves progressive loss of material and is due to relative motion between that surface and a contacting substance or substances" [1].

3.3.2   Standard methods

The current standard methods for evaluating abrasive wear are too coarse to be useful for generating the intrinsic wear resistance in case of relatively thin coating films. Thus, the conclusion is that the current standard methods do not satisfactorily meet the required application area of thin film tribological coatings.

3.3.3   Other methods

The important elements of a wear test are *simulation*, *acceleration* and *measurement*. The *simulation* must ensure that the specimen is subjected to the same behavior in the test as in its intended application and *acceleration* is employed to increase the intensity of testing to reduce the duration and cost of testing. The *measurement*, which refers to the method of reporting wear, can be direct or indirect. Weight loss, volume loss, depth etc. are direct measures while the time required to wear through a coating, the load required, etc., are examples of indirect measures of wear. Many methods for evaluating the abrasive wear of

hard coatings are available. But only a few of them are the most routinely employed ones in the field of thin hard coatings.

The *Micro-abrasive test* [2, 3] employs a spherical counter body to cause wear on the specimen surface. During the test, a ball is rotated against the specimen in the presence of abrasive slurry. The abrasive action of the rotating ball results in the formation of a spherical crater which is assumed to reproduce the geometry of the ball. The abrasion resistance of the coating is expressed in terms of a wear coefficient that is calculated from the dimensions of the wear crater. A calibrated optical microscope is usually employed for measuring the diameter of the crater. The dimensions can also be obtained by 3D optical profilometry.

A variation of the micro-abrasive test is the *Dimple grinder test* [4]. This technique uses a commercially available dimple grinder for evaluating the wear resistance of coatings. The grinding wheel is in the shape of a disc cut out from the center of a sphere and is made to rotate about a horizontal axis. The test specimen is placed below the grinding wheel, with its rotational axis perpendicular to that of the grinding wheel. This arrangement ensures that the combined motion of both the grinder and the specimen results in a hemispherical shaped wear crater. During the test, the interface between the grinder and the specimen is immersed in abrasive slurry to simulate an abrasive environment. The dimensions of the wear crater are measured by interrupting the test at periodic intervals and the wear constants of both the substrate and the coating are calculated from the resulting series of crater diameter readings. For accurate wear rate determination, the deviations from the ideal test conditions should be kept to a minimum: e.g., the wheel should have perfectly spherical contact geometry; the rotational axis of the wheel should be perfectly horizontal, etc. Any error in the slope of the wheel axis will lead to uneven contact with the specimen leading to deviation from the spherical geometry of the wear scar.

The *Dry sand/rubber wheel test* [5] simulates a low stress, three body abrasive environment. The specimen is loaded against a rotating rubber rimmed steel wheel. The wheel is coated with rubber to maintain a constant contact pressure on the specimen as it wears away during the course of the test. A dry abrasive, usually sand, is introduced in the interface between the sample surface and the rubber wheel. The action of the sand particles causes material loss by abrasion. The total amount of material removed by a given amount of abrasive can be calculated at the end of the test. From the mass loss and density of the material, the volume loss can be determined and given as an indirect measure of abrasion resistance. Since the material loss involved is very low, accuracy of the weighing device plays an important role in the test. If during the test the coating is penetrated, the mass loss will involve both the coating and the specimen. In such a case interpretation of the test result will be difficult as the contribution of the coating and the substrate to the mass loss cannot be separated unless the distribution of contact pressure or wear rate between the coating and substrate is known. A safe and cautious approach would be to avoid using the data from tests in which the coating was penetrated.

9

3.3.4   Recommended method for testing and evaluation

Near-term solution

Same as the long-term solution explained in the next section.

Long-term solution: The Micro-abrasive (Ball Crater) Test

The *micro-abrasive test* or the *ball crater test* as it is commonly known is one of the widely used tests for evaluating abrasion resistance (see also *Sections 3.11.4 & 3.13.4*). During the test, a sphere of hardened steel is made to rotate under load against the surface of the specimen in the presence of slurry of abrasives (Fig. 1). The load in the test can either be provided by the weight of the sphere or the specimen can be mounted on a pivoted arrangement to provide the load. A constant tangential rotational velocity is imparted to the ball through contact with a rotating shaft. The driving shaft is usually coated with rubber to increase the friction between the ball and the shaft to reduce the possibility of slip in the drive. The slurry is usually a suspension of silicon carbide particles in distilled water.
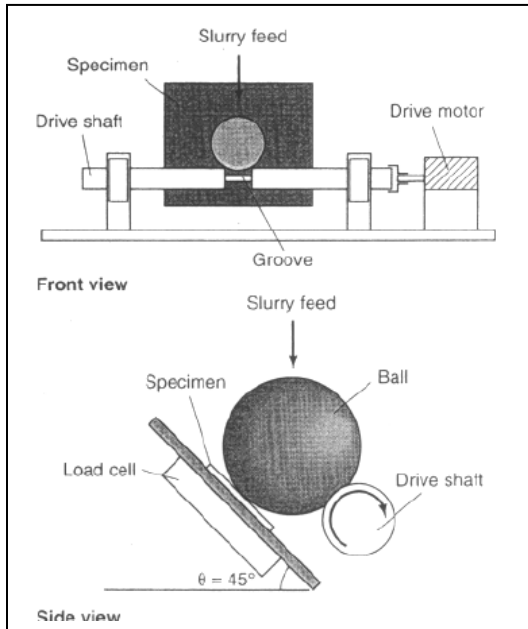
Fig. 1. Schematic representation of the micro-abrasive wear test apparatus [1].
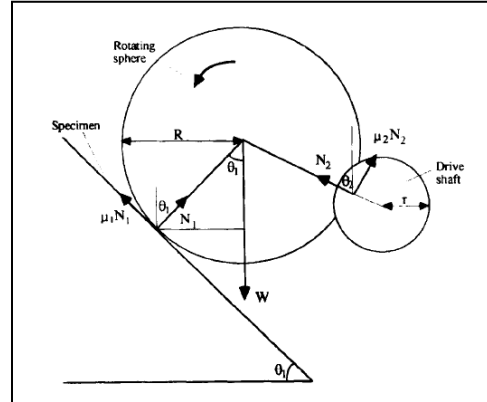
Fig. 2. Force diagram for the micro-abrasive wear test [2].

As the test proceeds, the abrasive action of the rotating sphere generates a crater on the specimen surface. The diameter of the crater is measured at periodic intervals during the test using a calibrated optical microscope. The intervals correspond to a fixed sliding distance of the sphere. The microscope is so mounted such that the diameters can be measured without moving the specimen, although the sphere must be removed and relocated in an identical position following each measurement. The sliding distance is calculated by recording the time taken by the sphere for a set number of revolutions of the sphere and extrapolating it to the duration of the test. Any variation in the sliding distance

10

can be reduced by ensuring a non-slip condition between the sphere and the driving shaft.

The crater diameter readings obtained from the test are used to calculate the wear constant which is essentially a measure of the abrasive wear rate, i.e., the lower the wear constant, the better the resistance to abrasive wear. The wear constants can be determined from the following wear model [2],

$$\frac{SN_1}{b^4} = \left(\frac{K_s - K_c}{K_s K_c}\right)\left(\frac{\pi t}{4b^2} - \frac{\pi R t^2}{b^4}\right) + \left(\frac{1}{K_s}\right)\left(\frac{\pi}{64R}\right), \tag{1}$$

where S is the distance slid by the sphere; N_1- normal force on the sample; R-radius of the sphere; b - external diameter of the crater; K_s, K_c - wear coefficient of the substrate and coating, respectively. A plot of $\frac{SN_1}{b^4}$ against $\left(\frac{\pi t}{4b^2} - \frac{\pi R t^2}{b^4}\right)$ is a linear graph. The value of K_c can therefore be obtained directly from the intercept and this value can be used together with the gradient to determine K_c.

When the normal force (N_1) on the specimen is provided by the ball, it can be calculated using the following formula,

$$N_1 \approx \frac{W \sin\theta_2}{[(\sin\theta_2)(\cos\theta_1 + \mu_1(\sin\theta_1 + \sin\theta_2)) + (\cos\theta_2)(\sin\theta_1 - \mu_1(\cos\theta_1 - \cos\theta_2))]}, \tag{2}$$

where W is the weight of the sphere; μ - coefficient of friction between the sphere and specimen; θ_1, θ_2 - angles as shown in Figure 2 and given by

$$\theta_2 = 90° - \cos^{-1}\left[\frac{(H-r)}{(R^2 - g^2/4)^{1/2} + r}\right] \text{ where } H = L_1 - L_2 - R + 2r. \tag{3}$$

3.3.5   References

1. Hawk J.A, "Abrasive wear testing" *ASM Handbook – Mech. Testing and Evaluation.*(2000): 325-337.
2. Rutherford K.L, Hutchings I.M, "A micro-abrasive wear test, with particular application to coated systems" *Surf. Coat. Tech.* 79 (1996): 231-239.
3. Batista J.C.A, Joseph M.C, Godoy C, Matthews A, "Micro-abrasion wear testing of PVD TiN coatings on untreated and plasma nitrided AISI H13 steel", *Wear* 249 (2002) 971-979.
4. Kassman A, *et. al.* "A new test method for the intrinsic abrasion resistance of thin coatings" *Surf. and Coat. Tech.* 50 (1991): 75-84.
5. Stevenson A.N.J, Hutchings I.M, "Development of the dry sand/rubber wheel abrasion test" *Wear.* 195 (1996): 232-240.

3.4 Adhesion between the Coating and Substrate

3.4.1   Definition

Adhesion may be termed as "*the state in which two surfaces are held together by interfacial forces which may consist of valence forces or interlocking forces or*

both" [1]. These bonding forces can be van der Waal's forces, electrostatic forces and/or chemical-bonding forces which are effective across the interface.

3.4.2   Standard methods

The available standard methods of adhesion testing are not directly applicable to the area of hard coatings.

3.4.3   Other methods

An important parameter in the characterization of a coating is its adhesion to the substrate. Therefore it's not surprising that there are many methods available for its evaluation. But majority of the tests can only be used in cases when the adhesion is poor. Adhesion tests typically involve inducing a known stress at the coating – substrate interface to cause coating detachment. The load required to cause failure is usually taken as the measure of adhesion. A good test must produce the stresses that would be experienced by the coating under service. Some of the commonly employed tests of adhesion measurement are the scratch test, the indentation test and the blister test.

The *scratch test* [2, 3] involves traversing a diamond probe across the surface of the specimen either under a constant load or a progressively increasing load until film failure occurs. "Scratch resistance" is understood as being the mechanical resistance of a coating to scratches [4]. The minimum critical load at which the coating stripping occurs can thus be estimated and used as a measure of adhesion. Usually, the scratch test utilizes a spherical diamond tip of Rockwell C geometry. During testing the tip load is continuously increased and a critical load for coating failure is detected. The failure criterion may be occurrence of the first crack or first induced cohesive or interfacial fracture. The actual point of failure of a coating can be detected in two ways – using an optical microscope or by use of acoustic transducers. The latter is more accurate and particularly useful in the case of thin coatings and when both the coating and substrate are visually indiscernible due to similar color or characteristics. Scratch testing can also give detailed information about different modes of coating failure and much knowledge of a coating can be gained by studying the scratched sample, e.g. in the SEM. Scratching at different locations at constant load can be used to investigate the coating quality and homogeneity.

The *blister test* [5] allows determination of the coating adhesion at elevated temperatures. In this test a hole is drilled into the substrate before coating it. This allows a fixed amount of air to be trapped at the interface. The specimen is then heated to cause the air to expand while maintaining an external load over the hole. This load is maintained to prevent premature delamination of the film till the desired temperature is achieved. When the load is removed, the gases expand causing delamination of the film. The adhesion strength is then indicated as the size of the delamination.

Another commonly used method is the *indentation test* [6] in which a conventional micro hardness indenter like Vickers' or Brale is used to introduce a

stable crack in the interface of the coating and substrate. The load on the specimen is gradually increased till the critical point is reached where the mismatch between the plastic zone sizes of the coating and substrate is large enough to cause cracking and eventually and finally film delamination. In the indentation technique, the approximate load for lateral crack initiation and the slope obtained from the indentation load-lateral crack length function are two useful adhesion parameters. The latter is demonstrated to be more discriminating in several test cases. Another indentation-based method of characterization involves studying the indentation produced under an optical microscope and relating it to predefined failure modes [7]. The failure modes are given values as HF1-HF6, according to the degree of damage around the indentation, where HF1-HF4 represents good adhesion and HF6 represents insufficient adhesion. This test was developed in Germany and is standardized in the *VDI Guidelines 3198* published in 1991.

An alternate method is the *shock wave test* [8] which stresses the interface by a pulsating disturbance. A high energy laser is focused on the backside of the specimen to explosively evaporate a small amount of material. This causes a shock wave to be generated inside the specimen. When this pulse propagates across the interface of the coating and substrate, it will cause the film to delaminate if the amplitude of the wave exceeds the adhesive strength of the coating. If the amplitude of this pulse at the interface can be evaluated, it can be used as the measure of the coating adhesion.

3.4.4   Recommended method for testing and evaluation

Near-term solution

Same as the long-term solution explained in the next section.

Long-term solution: Scratch test

Scratch testing has, together with hardness measurements, become the most common way of assessing the mechanical quality of coatings. It is the only one easily available and practical method for testing ultra-adherent thin films. The objective of the test is to qualitatively measure the force at which coating fails as compared to coatings of similar nature and thickness.

The apparatus consists of a movable diamond stylus. The stylus is dragged over the surface of the specimen under a step wise or a continuously increasing load until the delamination of the coating occurs. When the stylus is dragged under a step wise load, multiple scratch channels are required at different loads to determine the coating failure. The coating is observed under an optical microscope after every pass to determine the critical load at which initial failure has occurred. Since in practice, the coating is seldom removed entirely from the channel, the critical load is considered as the load at which the adhesive loss occurs regularly and significantly by flaking or by stripping, along the length of the channel.

13
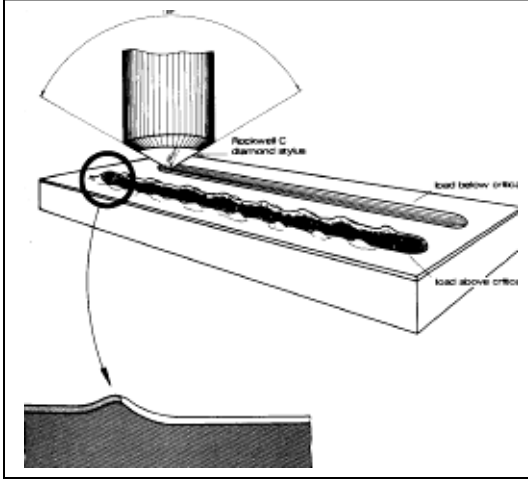
Fig. 1. Schematic representation of the stylus and scratch channel [2].
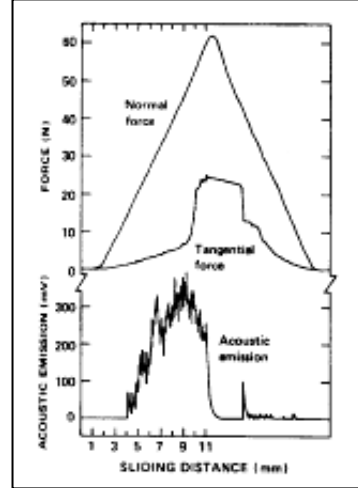
Fig. 2. Traces from the emission detector in the scratch test [3].

In the scratch test, the coating detachment can be observed by optical microscopy or by using acoustic emission detectors. An acoustic transducer is installed at the upper end of the stylus which records the acoustic signature of the coating with load. When the load on the stylus exceeds the adhesive strength of the coating, a crack is created. This crack initiation is accompanied by a burst of energy which is recorded by the transducer. The signal can either increase abruptly (Figure 1) or steadily (Figure 2) as a function of load. Alternatively, friction forces can also be monitored to estimate the critical load. Acoustic emission and frictional force measurements offer significant advantages over the optical microscopy method. Electronic recording of the test results is possible; the sensitivity of the method is increased especially when evaluating thin (less than 1 μm) hard coatings; when coatings are of the same color as the substrate, it is difficult to study the coatings by optical microscopy especially when extensive deformation of both the coating and substrate has occurred. SEM examination is frequently better than optical microscopy.

A coating, in practice, can have two failure modes: *adhesive* and *cohesive*. Since both these failures may result in abrupt changes in acoustic signals, the initiation of the cracks and the failure mode of the coating must always be confirmed by microscopic examination of the scratch channel. The exact point of failure can then be determined by measuring the travel distance between the start of the test and the evidence of the event of failure.

The critical load of the scratch test is influenced by many factors such as the substrate hardness, coating hardness, surface roughness, loading rate, indenter tip radius and friction between the coating and indenter. An expression, which incorporates most of these properties, is given by Bull *et al* [in 8],

$$F = \frac{A_1}{v_c \mu_c} \left(\frac{2EW}{t} \right)^{1/2}$$

(1)

14

where A_1 is the cross-sectional area of the track; E and ν_c - Young's modulus and Poisson's ratio of the coating, respectively; t - thickness of the coating; μ_c - coefficient of friction. The wear of the diamond stylus can also affect the critical load. Therefore, the stylus must be periodically inspected for wear to prevent its failure which may lead to erroneous results.

3.4.5   References

1.   ASTM standard D 907-03. Standard Terminology of Adhesives. ASTM International; 2003.
2.   Perry A.J, "Scratch adhesion testing of hard coatings" *Thin Solid Films.* 107 (1983): 167-180.
3.   Valli J, Makela U, "Applications of the scratch test method for coating adhesion assessment" *Wear.* 115 (1987): 215-221.
4.   Hogmark S., S. Jacobson, M. Larsson. "Design and evaluation of tribological coatings" *Wear* 246 (2000): 20–33.
5.   Kai- Tak Wan, "A novel blister test to investigate thin film delamination at elevated temperature" *Int. J. Adhesion and Adhesives.* 20 (2000): 141-143.
6.   Kim J.J, J. J.H, Lee K.R, Kwon D, "A new indentation cracking method for evaluating interfacial adhesion energy of hard films" *Thin Solid Films.* 441 (2003): 172-179.
7.   Heinke W, Leyland A, Matthews A, Berg G, Friedrich C, Broszeit E, "Evaluation of PVD nitride coatings, using impact, scratch and Rockwell-C adhesion tests" *Thin Solid Films*, 270 (1995): 431-438.
8.   Rickerby D.S, "A review of the methods for the measurement of coating-substrate adhesion" *Surf. and Coat. Tech..* 36 (1988): 541-557.

3.5   Erosive wear

3.5.1   Definition

Erosion is defined as "*progressive loss of original material from a solid surface due to mechanical interaction between that surface and a fluid, a multi-component fluid, or impinging liquid or solid particles*" [1]. Surface damage caused by impinging hard particles is usually referred to as *particle erosion*. Generally, resistance to particle erosion requires a combination of hardness and toughness, with the toughness being the dominant parameter. For a thin coating to be effective in erosion protection, individual impacts must not plastically deform the substrate material. The extension of plastic strain is controlled by the particle size, velocity and angle of impact.
In mild situations, where only the coating is permanently deformed by the impacts, particle erosion can be used to evaluate intrinsic erosion properties of the coating, or as a microscale toughness test.

3.5.2   Standard methods

The available standard methods of evaluating erosive wear are not directly applicable to thin hard coatings. The *erosion test by solid particle impingement* [1] can be used as a guide in carrying out the test explained later in this section. This method utilizes the repeated impact erosion approach in which a stream of particles is made to impact against the test specimen. This method is used to rank

15

the erosion resistance of materials under specified conditions of testing. Other standard methods like the *dry sand/rubber wheel test* [5] and the *liquid impingement erosion test* [3] can also be used as references. Although there is a correlation between abrasive wear measured using the dry sand/rubber wheel test and solid particle erosion, particularly low angle impingement, for some coatings they are distinctly different modes of wear.

3.5.3   Other methods

Erosion is often quoted as mass of material removed from the surface of the specimen by unit mass of erodent particles striking it. Sometimes, it is also expressed as the volume of material removed by unit mass of the erodent particles. Erosion depends on many parameters like impact velocity, impact angle, size and shape of the particles etc. A good erosion test must therefore not only be able to reproduce the actual working conditions but should also be capable of monitoring and measuring the parameters stated above.

The *gas blast test* [4, 5] is one of the most commonly used methods for estimating the erosive durability of thin coatings. In this method, the abrasive particles are introduced into a high velocity gas stream and made to strike the test specimen which is fixed at a known distance away from the nozzle. The erosive action of the impinging particles at a 90 deg impingement angle produces a circular wear scar on the surface of the specimen. The radius of this scar can be measured by an optical microscope or by using an image analyzer to estimate the critical dose of particles required to remove the coating. Since the particles start diverging after leaving the nozzle, the particle flux is not the same over the entire region of the scar. This can be corrected by introducing a focus coefficient in calculating the critical dose. Multiple samples can also be tested by mounting them on the outer periphery of a rotating disc in front of a jet containing erosive particles.

Another test commonly used is the *slurry erosion test* [6] which uses a focused slurry jet to cause erosion of the specimen. The abrasive particles are contained in a stream of water. This abrasive slurry is mixed with high pressure air in the nozzle to produce a high pressure jet that is made to impinge on the surface of the specimen. The specimen is usually located perpendicular to the nozzle at a known standoff distance. The angle of impingement of the jet can also be varied by tilting the specimen to a required angle. The nozzle with a square opening can be used to produce a square wear scar which allows for easy measurement of the wear area. Since the mass loss occurring in the test will be very small to be determined accurately by weighing, surface profilometry can be used to measure the geometry of the scar. The volume can then be estimated from the dimensions.

Yet another commonly used test is the *centrifugal accelerator test* [7]. The centrifugal accelerator consists of a rotating disc with a number of specimens mounted on its periphery. The abrasive particles are fed at the center of the disc and there are grooves running radially from the center of the disc that carry the particles to the outside. The particles are accelerated due to the spinning of the

16

disc and they exit the grooves at a tangential velocity equal to that of the disc. When the particles strike the surface of the specimen erosion takes place and the wear rate can be estimated by determining the volume loss after the test. This method has the advantage that a number of specimens can be simultaneously tested under the same wear conditions. Erosion at various angles can also be achieved by accordingly positioning the sample faces with respect to the particle stream.

3.5.4   Recommended method for testing and evaluation

Near-term solution

Same as the long-term solution explained in the next section.

Long-term solution: Gas blast test

The gas blast method involves impacting the specimen with a stream of hard abrasives with a known velocity and well defined divergence. In the gas blast apparatus, the particles are accelerated along a nozzle by a stream of high velocity gas or air (Fig. 1). The particles exit the nozzle at a very high speed and strike the specimen which is mounted at a fixed standoff distance from the end of the nozzle. The erosive action of the impinging particle causes a crater to be formed on the surface of the specimen. The dimensions of this crater can be measured by means of a graded optical microscope or by using an optical image analyzer.
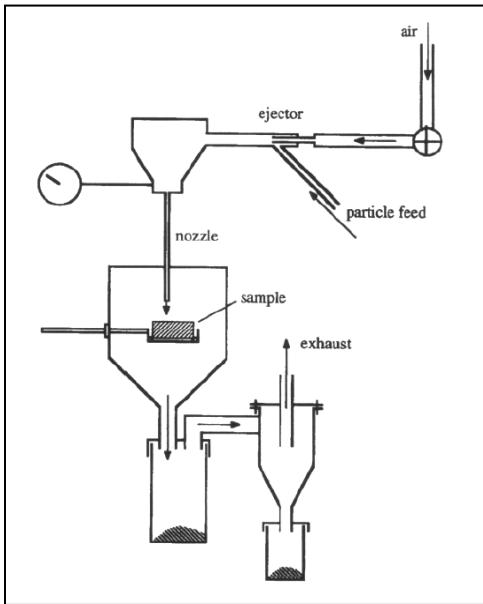
Fig. 1. Schematic representation of the gas blast apparatus [2].
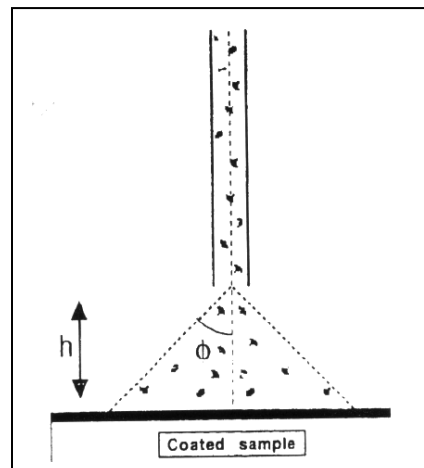
Fig. 2. Schematic representation of the divergence of erodent particles from a nozzle [3].

17

The measure of the erosion durability of the coating can then be given by the critical dose of particles required to remove the coating which can be calculated from the dimensions of the wear scar as follows [4],

$$r = \frac{h}{\beta} \ln m - \frac{h}{\beta} \ln \left(\frac{2\pi h^2 Q_c}{\beta^2} \right), \tag{1}$$

where Q_c is critical mass of particles per unit area required to remove the coating; m - total mass of erodent particles, h - nozzle to target standoff distance, β - focus coefficient (experimentally determined dimensionless quantity). Since the particles diverge when they exit the nozzle, the particle flux striking the nozzle is not the same over the entire region of the crater (Fig. 2). This angular distribution of the particle flux can be described by a simple function [4],

$$p(\phi) = \beta^2 \frac{\sin \phi}{\cos \phi} \exp(-\beta \tan \phi), \tag{2}$$

where the value of β depends on the geometry of the nozzle, the particles and the testing conditions. The accuracy of the method is affected when the coating is penetrated during the course of the test as the mass loss is contributed by the substrate also. The mass loss due to the substrate can be separated from that of the coating only if the change in the rate of mass loss as the substrate is penetrated can be measured. This can be successful only if the erosion rate of the substrate is significantly greater than that of the coating. Measuring the rate of loss without penetrating the coating is preferable.

3.5.5　References

1. ASTM standard G 76-02. Standard Test Method for Conducting Erosion Tests by Solid Particle Impingement Using Gas Jets. ASTM International; 2003.
2. ASTM standard G 65-00e1. Standard Test Method for Measuring Abrasion using the Dry Sand/Rubber Wheel Apparatus.
3. ASTM standard G 73-98. Standard Practice for Liquid Impingement Erosion Testing.
4. Shipway P.H, Hutchings I.M, "Measurement of coating durability by solid particle erosion" *Surf. Coat. Tech. 71* (1995): 1-8.
5. Rutherford K.L, Hutchings I.M, "Development of the erosion durability technique for thin coatings" *Surf. Coat. Tech. 86-87* (1996): 542-548.
6. Iwai Y, et al. "Evaluation of wear resistance of thin hard coatings by a new solid particle impact test" *Wear. 251* (2001): 861-867.
7. Hutchings I. M, "Solid particle erosive wear testing" ASM Handbook – Mechanical Testing and Evaluation. 8 (2000): 338-345.

3.6　Fatigue

3.6.1　Definition

Fatigue is defined as the "*progressive, localized and permanent structural damage that occurs when a material is subjected to cyclic or fluctuating strains at nominal stresses that have maximum values less than the static yield strength of the material*" [1].

18

3.6.2   Standard methods

The available standard methods of evaluating fatigue resistance do not
satisfactorily meet the required application area of thin hard coatings.

3.6.3   Other methods

Numerous types of test procedures have been developed for fatigue crack
initiation testing. The tests involve subjecting the interface of the coating-
substrate system to a cyclic stress and determining the number of cycles that it
can withstand without failure. Some of the tests applicable to coatings follow.

The *spherical rolling test* [2] can be used for estimating the interfacial fatigue
strength of thin hard films. In this test, a series of hardened balls are made to
rotate under load on the coated specimen. This sets up cyclic stresses at the
interface of the coating and substrate and causes spalling of the coating. The
fatigue strength is reported as the maximum stress amplitude that the coating
can withstand without failure for $5x10^6$ cycles with the spalled area less than 5%
of the contact area. Since the test is high cycle, the stresses are maintained in the
elastic region of the specimen and the results are independent of the plasticity of
the substrate.

The *coating impact test* [3] can also be used to determine the value of a critical
fatigue force of the coating. The tester consists of a hardened steel ball that is
made to impact against the specimen, repeatedly at regular intervals. This creates
stresses in the coating at the point of impact. The impact motion is exercised by
means of a sprung-mass system that comprises a pre-stressed spring, a carbide
ball, a force sensor and a cylindrical coil that acts as a sprung mass. The
oscillation is produced by magnetic forces between a permanent magnet and the
cylindrical coil. The coating is tested until failure which is marked by complete
spalling of the coating. The test allows the control of the impact force, impact
frequency and the number of impacts by means of a stored program control. A
thin film of oil is usually applied at the impact point to prevent wear of the ball.
The load can be monitored using the force sensor and a curve showing the
loading of the coating – substrate composite as a function of number of stress
cycles endured can be obtained to determine the behavior of the system under
dynamic loading and to compare different systems.

One of the simplest methods of estimating the interfacial fatigue strength is
explained by Chen *et al* [4]. This test uses the apparatus designed for evaluating
sliding wear. The specimen is in the form of a sphere pressed against a cylindrical
counter body made of hardened steel at a constant normal stress. The width of
the counter body is designed according to the contact stress, but is always
maintained less than that of the specimen. During the test, the contact parts are
rotated at a constant speed and lubricating oil is added at the interface to prevent
failure of specimen by wear or other means. The specimen is inspected for the
detachment at periodic intervals throughout the duration of the test. The
maximum stress amplitude that the specimen has withstood for $5x10^6$ cycles with

19

a detachment area less than 5% is reported as the fatigue strength of the
specimen.

3.6.4 Recommended method for testing and evaluation

Near-term solution

Same as the long-term solution explained in the next section.

Long-term solution: Spherical rolling test

In this test, a series of balls are made to rotate under contact loading on the
surface of the specimen. This sets up an interfacial stress which causes the
coating to exfoliate. The maximum sustained shear stress amplitude is then used
as the interfacial fatigue strength.

The apparatus consists of a pair of bearing races which acts as the counterparts.
The balls are made of uncoated hardened steel. The specimen, a flat surface
coated on one side, is pressed onto the balls under a normal load. The whole
system is immersed in lubricant to minimize the wear in the apparatus. The ball
bearings are made to roll on the surface to set up cyclic loading stresses in the
specimen. Since the contact fatigue is tested under high cycle running, the
loading stress is in the elastic region of the sample and the results are sensitive to
the interface condition and unaffected by the plasticity of the substrate.

The test is interrupted periodically to check for the delamination of the coating.
The coating is considered as failed if 5% of the coated contact area has exfoliated.
The load vs. number of cycles plot is then generated and the maximum load at
which the coating layer sustained a detachment area less than 5% of the contact
area after 5×10^6 cycles is taken to calculate the shear stress amplitude at the
interface depth. The experimental time can be reduced by increasing the number
of balls used in the test and also by increasing the rotation speed.
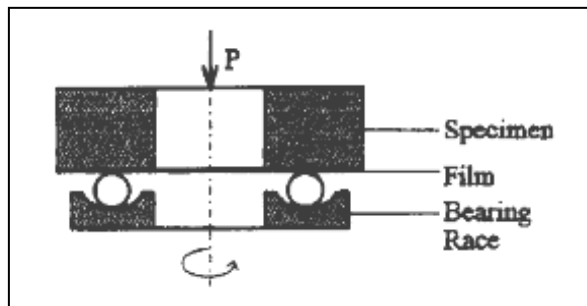
Fig. 1. Schematic representation of the spherical rolling
test [2].

This test is mostly suitable for bearing applications since it does not address the
issue of the effect of coatings on the fatigue properties of the substrate that are
important for highly stressed components such as compressor and turbine
blades, turbine shafts, and landing gear components. For these applications,
standard mechanical fatigue tests using coated test specimens are necessary.

20

3.6.5   References

1. "Fatigue and fracture mechanics" *ASM Handbook – Mechanical Testing and Evaluation.* 8 (2000): 681-683.
2. He J. W, Xu K. W, Hu N. S, "Evaluation of bonding strength of thin hard films by spherical rolling test", *Surf. Coat. Tech.* 97 (1997): 295-298.
3. Knotek O, *et al.,* "A new technique for testing the impact load of thin films: the coating impact test", *Surf. Coat. Tech.* 54-55 (1992): 102-107.
4. Chen H, Yi M. Z, Xu K. W, He J. W, "Bonding strengths of PCVD films under cyclic loading", *Surf. Coat. Tech.* 74-75 (1995): 253-258.

3.7   Fracture strength

3.7.1   Definition

Fracture may be defined as the "*mechanical separation of a solid owing to the application of stress.*" Fracture toughness is defined as a "*generic term for measures of resistance to extension of a crack*" [1].

3.7.2   Standard methods

The available standard methods of evaluating fracture resistance do not satisfactorily meet the required application area of thin hard coatings.

3.7.3   Other methods

Coating cracking or fracture is the starting point of damage of a coating. Therefore the resistance of the coating to crack propagation is very crucial. Cracking is caused by tensile stresses; therefore the presence of any compressive stresses in the specimen will allow it to take up more strain before fracture. Since this will lead to an erroneous estimation of the toughness, the coatings must be relieved of any residual stresses before testing. Although several tests have been developed to characterize the toughness of materials, few can be applied to thin hard coating.

The *four-point bend test* [2, 3] is the most widely used experimental method for determining the cracking resistance of tribological coatings. The apparatus consists of two adjustable supports and a means for measuring deflection and the applied load. The specimen is in the form of a flat beam of rectangular cross section that is coated in the middle with the ends left uncoated where they rest on the outer supports. During the test, the load is continuously increased and recorded by means of a load cell. Cracks start appearing in the coating once the critical strain is exceeded. This onset of cracking can be detected by means of an optical microscope or by using acoustic emission detectors. A measure of the crack resistance of the coating can then be estimated from a plot of crack density vs. coating strain.

A variation of the four-point bend test proposed by Jaeger *et al.* [4] involves introducing a sharp crack in the substrate before it is coated. This pre-cracking reduces the stiffness of the specimen and allows the film to be considered as free-standing. During four-point bend loading, the film first ruptures at the front face followed by crack propagation along the sides. Usually, a partially separated specimen is used to ensure stable crack propagation. Fracture toughness can then

be calculated from film load and corresponding compliance change during successive crack growth on the specimen sides. The crack opening is measured by means of inductive strain gauges fixed on the specimen for increasing the accuracy of measurement. This method, though simple in principle involves complicated specimen preparation and measurement.

Another method for measuring the fracture toughness of thin films proposed by Kamiya *et al.* [5] involves removing a part of the substrate from the film at one end to obtain an overhanging film edge. Selective etching process is employed to obtain this geometry by chemically dissolving a portion of the substrate. A rectangular notch is then cut at the edge of the over hang to serve as a crack initiator and a normal force is applied to the both sides of the notch simultaneously. A needle with a tip radius larger than the width of the notch is used for this purpose. The applied load can be measured using strain gauges attached to the specimen. Crack propagation starts beyond the critical load which can be detected using a microscope and the extensions can be measured using a scale in the eye-piece. A load vs. crack extension diagram is then plotted for the experimental data to evaluate the toughness.

The *micro-impact technique* [6] simulates a repetitive impact environment to investigate the fracture toughness of thin coatings. The specimen is made to oscillate at a high frequency by means of a piezoelectric oscillator while subjecting it to a static load. By maintaining high amplitude of vibration, the probe is made to bounce on the surface so that impact behavior can be observed. The instantaneous probe position is monitored throughout the test and a graph between probe depths and time is used to study the response of the material. Time-to-failure and the overall change in probe depth during a test are reported as measures of the resistance of the coating to fracture.

3.7.4   Recommended method for testing and evaluation

Near-term solution

Same as the long-term solution explained in the next section.

Long-term solution: Four-point bend test

The bending test is used to estimate the cracking resistance in terms of the amount of tension that a coating can withstand without cracking. The equipment consists of two pairs of convex edged load applicators. One pair is fixed while the other pair can be moved to provide the load. The specimen is a flat beam of rectangular cross section that is coated at the centre leaving the ends uncoated where they rest on the outer supports. During the test, the specimen is subjected to tension along its top surface and compression along its bottom surface by imposing a continuously increasing load using the movable supports (Fig. 1). The load is recorded by a computer connected to a load cell.

22
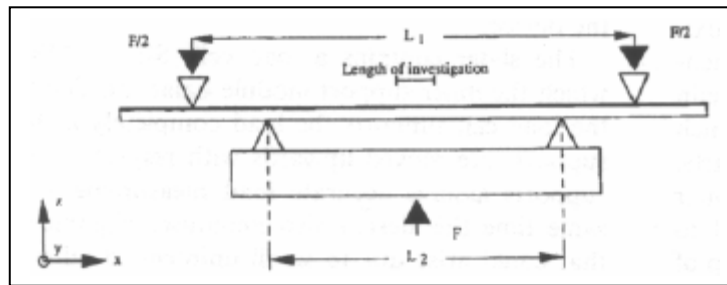
Fig. 1. Schematic representation of the four-point bend test [2].

When the coated beam is bent, the outer fibers are strained and cracks start to appear once the cracking resistance of the coating is exceeded. This corresponding strain is used as measure of the cracking resistance of the coating. The cracking can be detected in two ways – an optical microscope can be used to observe the crack appearance or acoustic emission detectors may be employed. When cracking occurs, it triggers a stress wave in the material that causes the deformation of the piezoelectric transducers attached to the specimen. The transducers generate an output signal proportional in magnitude to that of the wave. Therefore the occurrence of the crack can be identified by a sudden increase in the acoustic emission.

Most coatings produced by deposition techniques contain residual stresses. When the beam is bent, the certain elongation is required to over come this strain before cracks starts to appear. It is therefore required to consider this stress in estimating the fracture toughness or proper procedures must be followed to relieve the stresses prior to testing.

This is a good test if an appropriate fixture is used during deposition so the residual stress is allowed to accumulate as it would on an actual component. A simple strain-to-fracture measurement is very useful as a guide to applications where changes in fatigue characteristics of the substrate must be avoided or accommodated in design.

3.7.5   References

1. "Fracture toughness and fracture mechanics" *ASM Handbook – Mechanical Testing and Evaluation.* 8 (2000): 563-575.
2. Wiklund U, Bromark M, Larsson M, Hedenqvist P, Hogmark S, "Cracking resistance of thin hard coatings estimated by four point bend test", *Surf. and Coat. Tech.* 91 (1997): 57-63.
3. Cox L. C, "The four point bend test as a tool for coating characterization", *Surf. and Coat. Tech.* 36 (1988): 807-815.
4. Jaeger G, Endler I, Heilmaier M, Bartsch K, Leonhardt A, "A new method of determining strength and fracture toughness of thin hard coatings", *Thin Solid Films,* 377-378 (2000): 382-388.

23

5. Kamiya S, Kimuraa H, Sakaa M, Abeb H, "A new method for measurement of the toughness of brittle thin films", *Thin Solid Films,* 389 (2001): 180-186.
6. Ben D. Beake B. D, Garcıa M. J. I, Smith J. F, "Micro-impact testing: a new technique for investigating fracture toughness", *Thin Solid Films*, 398 –399 (2001): 438–443.

3.8   Coefficient of friction

3.8.1   Definition

Friction is the "*resistance to movement of one body over another body*" [1]. Frictional property of a material is commonly represented by the friction coefficient which is the dimensionless ratio of the friction force between the two bodies to the normal force pressing these two bodies together.

3.8.2   Standard methods

Due to the significant role played by friction in everyday activities, many standard methods have been devised to characterize friction. But all these have been developed for the evaluation of bulk materials. Since the properties of coatings differ widely from that of bulk materials, these standard methods can only be used as a guide in carrying out the tests suggested in *Recommended Method* section below.

The *Ball on flat test* [2] may be used as a reference in calculating the kinetic coefficient of friction. The test method involves sliding a spherically ended pin against the specimen surface. A vertical load is applied on the pin and it is made to reciprocate on the specimen surface. Friction forces are measured during the test by use of load cell or with a similar load sensing device and can be used to assess the change in frictional coefficient as a function of time.

3.8.3   Other methods

Micro-tribometry [3] is the most widely used technique to determine the frictional coefficients of thin films. The experiment consists of loading a ball or a pin on the surface of the specimen under a known load. The specimen is then dragged under the ball while maintaining the constant normal force. Frictional forces are set up due to the relative movement between the pin and the disc which causes the pin to distort. These forces can be measured when the pin is restrained by a force transducer. The coefficient of friction can then be calculated from the values of load and frictional force obtained from the test.
Another method for estimating the coefficient of friction of thin coating is the *Scanning Probe Microscopy* (SPM) [4]. The SPM apparatus consists of a cantilever that is loaded against the surface of the test specimen. A laser beam is made to reflect off the cantilever and is detected by a photodiode. During the experiment, the specimen is dragged under the cantilever at constant speed. This causes distortion of the cantilever due to the frictional forces acting on it. This in turn causes the reflected laser beam to impact the photodetector at a different point. This shift in focus point is measured by the apparatus to determine the frictional force which can then be used to calculate the coefficient of friction.

24

3.8.4 Recommended method for testing and evaluation

Near-term solution: Tribometry

The *tribometer* is one of the most versatile type of equipment for evaluating the
tribological properties of materials under selected conditions of load, speed and
temperature. These tribometers are capable of simulating most contact
geometries including *pin-on-disk*, *ball-on-disk*, and *block-on-disk* configurations.

A *pin-on-disk tribometer* has a pin with a hemispherical tip loaded on the
specimen (Fig. 1). The pin is usually held using a stiff lever that is designed as a
frictionless force transducer. During the test, a relative motion between the pin
and the specimen is obtained by either making the disc to rotate or reciprocate
below the pin. This relative motion sets up frictional forces between the pin and
specimen which causes distortion of the pin and the arm holding it. This causes
the transducer to generate an output signal proportional to the strain experienced
by it. The output signals are manipulated to obtain the frictional force values.
Most commercially available tribometers have the ability to automatically
calculate and display the friction coefficient in real time and also allows easy set
up of test parameters like the rotational speed, frequency, time, etc.

The pin-on-disc tribometers may give a wavy frictional force tracing due to the
variation in the surface conditions around the wear track on the specimen
surface. The lubricated coefficient of friction can also be determined by
immersing the interface of the pin and disc in oil during the test.
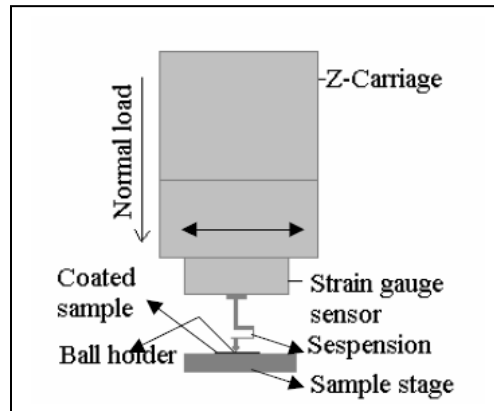
Fig. 1. Schematic representation of the experimental set-up for the friction
test [3].

The pin-on-disc or other adhesive wear tester (block-on-ring, crossed cylinder,
etc.) can be used simultaneously to measure both friction properties and wear
rates with any combination of coatings or other contact materials.

Long-term solution: Scanning probe microscopy

A scanning probe microscope can be used for evaluating the frictional coefficient
of thin coatings [4]. The first step in the process consists of scanning a portion
(20 x 20 μm) of the specimen surface to ensure that the surface irregularities are
within acceptable limits. If the surface finish is acceptable, an area of about 2 x 2
μm is the selected for carrying out the test. The SPM employs a cantilever that is

25

held in constant contact with the specimen surface (Fig. 2). A laser beam is made to incident on the surface of the cantilever and the reflected beam is detected using a photodetector.
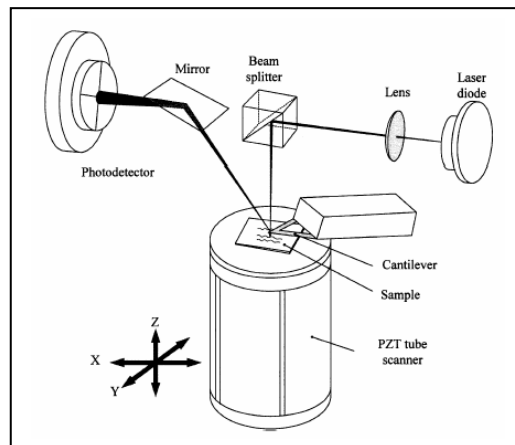
Fig. 2. Schematic representation of the SPM operation [4].

When the specimen is made to move slowly with respect to the cantilever, frictional force is induced at the interface of the pin and the specimen which causes the cantilever to twist which in turn changes the point at which the laser beam strikes the photo-detector. The detector has four independent quadrants that are capable of yielding an independent output signal. These output signals are then manipulated to obtain the required parameters like the frictional force.

The SPM apparatus is capable of measuring both friction and wear parameters and the type of probe used depends on the type of measurements involved. In measuring friction, the twisting that occurs in the cantilever due to the frictional forces is measured whereas in wear testing, the vertical deflection of the cantilever is measured. During the test, two different cantilevers are used. When the surface finish has to be evaluated, the cantilever with a lesser stiffness is employed. This reduces the actual load on the specimen and helps in improving the sensitivity of measurements. The frictional coefficient is then be calculated from the force data obtained during the test as, the average ratio of friction force to normal load. Alternatively, the frictional coefficient can also be determined from the slope of a plot of frictional force to normal load provided the slope is not zero.

3.8.5   References

1. Basse J. L, "Introduction to friction" *ASM Handbook – Friction, Lubrication and Wear Technology.* 18 (2000): 25-26.
2. ASTM standard G 133-02. Standard Test Method for Linearly Reciprocating Ball-on-Flat Sliding Wear. ASTM International; 2003.
3. Shukla P, Sikder A. K, Kumar A, Durvin R, McDonough M, Smith M. D, "Evaluation of tribological and mechanical properties of nitride thin films prepared by cathodic arc deposition", *Mat. Res. Soc. Symp. Proc.*, 750 (2003).

26

4. Fang T. H, Weng C. I, Chang J. G, Hwang C. C, "Nanotribology of amorphous
    hydrogenated carbon films using scanning probe microscopy", *Material
    Science and Engineering.* A337 (2002): 97-133. *Thin Solid Films,* 396 (2001):
    166-172.

3.9 Hardness

3.9.1 Definition

Hardness may be defined as "*the ability of a material to resist permanent
indentation or deformation when in contact with an indenter under load*" [1].

3.9.2 Standard methods

The available standard methods of evaluating hardness do not satisfactorily meet
the required application area of thin hard coatings.

3.9.3 Other methods

Hardness testing is one of the simplest and least expensive methods of
mechanically characterizing a material since it does not require much specimen
preparation and involves rather inexpensive testing equipment. Generally, a
hardness test consists of pressing an indenter of known geometry and mechanical
properties into the test material. Hardness is then quantified using one of a
variety of scales that directly or indirectly indicate the contact pressure involved
in deforming the test surface.

Conventional hardness tests like the Rockwell and Brinell tests cannot be used for
thin coatings. This is because the large loads employed in these tests may cause
the region deformed by the indentation to extend to the coating-substrate
interface. When the indentation reaches the substrate, the hardness measured is
influenced by the substrate and ceases to represent the true hardness of the
coating.

This problem may be overcome by use of light loads resulting in shallow
indentations restricted within the thickness of the coating. However, this practice
results in very low indentation depths which require measurements of very high
accuracy. One standard practice used by many investigators involves restricting
the penetration depth to less than 10% of the thickness of the coating to eliminate
the influence of the substrate. But there has been no universally accepted criteria
and many corrective formulae and methods have been put forth to improve the
accuracy of hardness measurements.

3.9.4 Recommended method for testing and evaluation

Near-term solution

Same as the long-term solution explained in the next section.

Long-term solution: Micro-hardness test

The most common approach for isolating the film properties is to make the
measurements at depths that are such a small fraction of the film thickness that

27

the behavior is essentially that of the material in bulk form. But in some applications, the films under consideration are so thin that substrate influence cannot be avoided at depths at which useful data can be obtained. In such cases, the composite hardness of the film/substrate system has to be estimated and the properties of the film derived from it.

The micro-hardness test [2, 3] provides a numerical value that distinguishes between the relative ability of materials to resist controlled penetration by a specified indenter. In a conventional test, a hard pyramidal indenter is forced into the surface of the material at a specified rate. The indenter is retracted after allowing it to remain stationary for some time. The characteristic dimensions of the residual impression are measured using a microscope and the hardness number is calculated. In many cases, instruments capable of continuously measuring the force and displacement of the indentation is used so that the load-displacement data can be easily obtained even when the indentations are too small to be conveniently imaged.
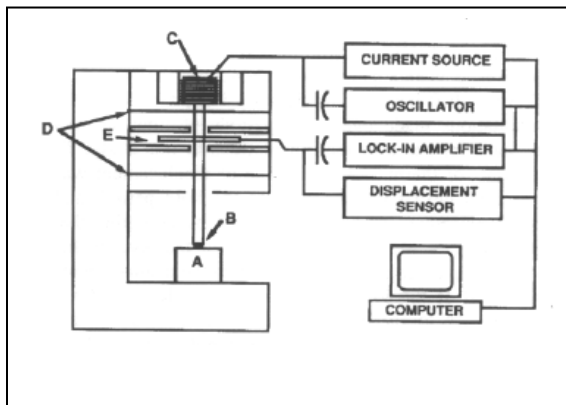
Fig. 1. Schematic representation of the apparatus for indentation experiments [2].
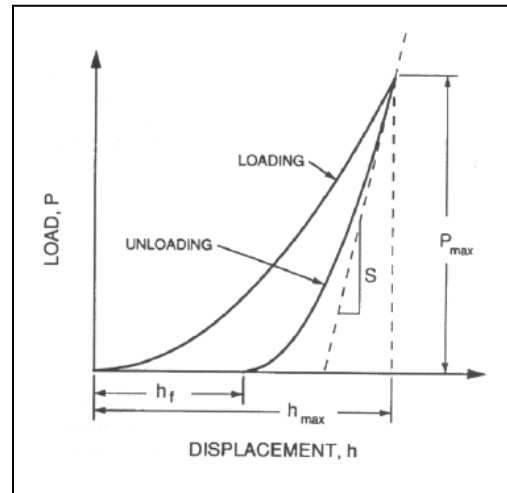
Fig. 2. Schematic representation of the load vs. indenter displacement [2].

The method proposed by Oliver *et al.* [2] uses a depth sensing indentation tester with a Berkovich indenter, a three sided pyramid with an area to depth function which is the same as that of a Vickers indenter, to carry out the test. The indenter was first loaded and unloaded three times in succession to ensure proper contact between the indenter and the specimen surface. After the third unloading, the load was held constant for a predefined hold period and the displacement was carefully monitored to detect any displacement produced by the thermal expansion of the system. After this the indenter was loaded for the fourth and final time with another hold period to detect any time dependent plastic deformation of the specimen.

The hardness defined as the mean pressure the material will support can be computed from [2],

28

$$H = \frac{P_{max}}{A} \qquad (1)$$

where P_{max} is the peak load and A is the projected area of contact at peak load (for Vickers's indenter, $A = 26.43h^2$). The projected area is calculated from the area function which relates the cross-sectional area of the indenter to the distance from its tip.

In another method, proposed by Tian *et al.* [4], the experiment is carried out in two steps to eliminate its effect of the substrate. In the first step, a maximum load of about 200 mN is selected which causes the substrate to influence the measured hardness of the coating. The load-displacement curve is then studied to determine the maximum load below which the hardness measurement will not be affected by the substrate. The initial loading curve will be linear with a large slope because a large load will be required to cause indentation of the coating. As the load increases, the slope begins to decrease as the strain extends to the soft substrate making penetration easier. In the second step, the load selected from step one is used as the maximum limit and the penetration experiment is conducted. The load-displacement curves are generated and the hardness can be calculated using Equation 1.

3.9.5   References

1. Revankar G, "Introduction to hardness testing" *ASM Handbook – Mechanical Testing and Evaluation.* 8 (2000): 197-202.
2. Oliver W. C, Pharr G. M, "An improved technique for determining hardness and elastic modulus using load and displacement sensing indentation experiments", *Journal of Material Research*, 7 (1992): 1564-1583.
3. Jonsson B, Hogmark S, "Hardness measurements of thin films", *Thin Solid Films. Tech.* 114 (1984): 257-269.
4. Tian J, Han Z, Lai Q, Yu X, Li G, Gu M, "Two-step penetration: a reliable method for the measurement of mechanical properties of hard coatings" will appear in *Surf. Coat. Tech.* (2003).

3.10 Modulus of elasticity

3.10.1 Definition

Modulus of elasticity also known as the Young's modulus is defined as "*the measure of rigidity or stiffness of a metal*" [1]. It is given by the slope of the stress-strain curve in the range of linear proportionality of stress to strain.

3.10.2 Standard methods

The available standard methods of evaluating the elastic modulus do not satisfactorily meet the required application area of thin hard coatings.

3.10.3 Other methods

Young's modulus of thin coatings is an important parameter since it has a strong influence on many characteristics like the coating adhesion, fracture and the residual stress state. Therefore, it is of fundamental importance to determine the

29

Young's modulus of thin films. Although many methods have been developed, the following are the most commonly employed.

The *instrumented indentation test* [2] employed for estimating the hardness of thin films can also be used to determine the Young's modulus of thin coatings. The procedure employed is the same as that for hardness. It involves pressing an indenter of known geometry and mechanical properties into the test material and graphing the load-displacement data during one complete cycle of loading and unloading. The Young's modulus is then calculated from the slope of the graph obtained from the test.

The *tensile test* has been used to evaluate the elastic modulus of coatings by Hollman *et al.* [5]. Here the specimens are in the form of thin foils that are coated uniformly on both sides. A plate with a hole is attached to both ends of the specimen such that the centers of the holes lie along the longitudinal axis of the coated specimens. One hole is used to suspend the specimen, while the other hole is used to load the specimen using dead weights. The loads were increased in steps and the strain induced was measured using strain gauges that were attached to the center of the specimen on either sides. The data collected was used to plot a force vs. strain graph. The Young's modulus is then obtained from the slope.

The *vibrating reed test* [5] is another simple method for estimating the Young's modulus of thin coatings. The specimen in the form of a rectangular or cylindrical beam is clamped at one or both of its ends and is excited into vibration. This vibration may be brought about in several ways; by an electromagnetic vibrator, acoustic waves, electrostatic methods etc. The resonance frequency for both coated and uncoated specimens is measured and this shift is used to estimate the modulus of elasticity.

3.10.4 Recommended method for testing and evaluation

Near-term solution

Same as the long-term solution explained in the next section.

Long-term solution: Instrumented indentation test

One of the simplest ways to determine the mechanical properties of thin films is to deform it on a very small scale. This is because the properties of thin films are easily influenced by the substrate when the indentations are larger and extend to the interface of the system. When shallow indentations are employed, the indenters are not in constant contact during the process. This can be overcome to a certain extent by using the Berkovich and Vickers indenters, which are pyramidal and hence can be ground to a point. In some cases, the films under consideration are so thin that substrate influence cannot be avoided at depths at which useful load-displacement data can be obtained. In such cases, the composite properties of the film-substrate system have to be estimated and the properties of the film derived from it.

Oliver *et al.* [2, 3] used a depth sensing indentation tester with a Berkovich indenter to estimate the mechanical properties of the specimen. The indenter was first loaded and unloaded three times in succession to ensure proper contact between the indenter and the specimen surface. After the third unloading, the load was held constant for a predefined hold period and the displacement was carefully monitored to detect any displacement produced by the thermal expansion of the system. After this the indenter was loaded for the fourth and final time with another hold period to detect any time dependent plastic deformation of the specimen.
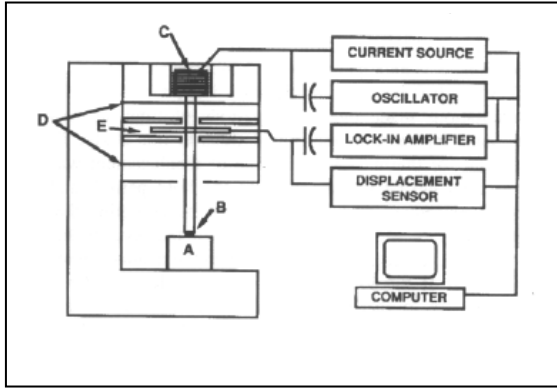
Fig. 1. Schematic representation of the apparatus for instrumented indentation [2].
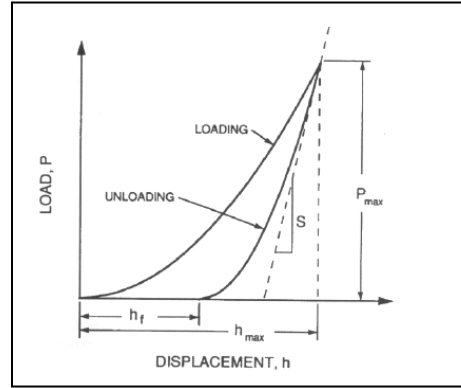
Fig. 2. Schematic representation of the load vs. indenter displacement data [2].

The key quantities measured during the process are the peak load (P_{max}), the depth at peak load (h_{max}) and the contact stiffness at initial unloading (S). The contact stiffness is obtained as the slope of the initial portion of the unloading curve. When the above data have been estimated, the modulus can be calculated as [2],

$$S = \frac{dP}{dh} = \frac{2}{\sqrt{\pi}} E_r \sqrt{A} \, , \tag{1}$$

where A is the projected area of elastic contact and E_r is the reduced modulus given by,

$$\frac{1}{E_r} = \frac{\left(1 - v^2\right)}{E} + \frac{\left(1 - v_i^2\right)}{E_i} \tag{2}$$

Here, E and v are the Young's modulus and the Poisson's ratio of the specimen, and E_i and v_i are the same parameters for the indenter, respectively.

In another method proposed by Tian *et al.* [4], the experiment is carried out in two steps to eliminate its effect of the substrate. In the first step, a maximum load of about 200 mN is selected to cause the substrate to influence the measured hardness of the coating. The load-displacement curve is then studied to determine the maximum load below which the hardness measurement will not be affected by the substrate. The initial loading curve will be linear with a large slope

because a large load will be required to cause indentation of the coating. As the load increases, the slope begins to decrease as the strain extends to the soft substrate making penetration easier. In the second step, the load selected from step one is used as the maximum limit and the penetration experiment is conducted. The load-displacement curves are generated and the Young's modulus is determined from the slope of the unloading curve.

3.10.5 References

1. *ASM Handbook – Mechanical Testing and Evaluation.* 9 (2000): 946.
2. Oliver W. C, Pharr G. M, "An improved technique for determining hardness and elastic modulus using load and displacement sensing indentation experiments", *Journal of Material Research*, 7 (1992): 1564-1593.
3. Jonsson B, Hogmark S, "Hardness measurements of thin films", *Thin Solid Films. Tech.* 114 (1994): 257-269.
4. Tian J, Han Z, Lai Q, Yu X, Li G, Gu M, "Two-step penetration: a reliable method for the measurement of mechanical properties of hard coatings" to appear in *Surf. Coat. Tech.* (2003).
5. Hollman P, Larsson M, Hedenqvist P, Hogmark S, "Tensile testing as a method for determining the Young's modulus of thin hard coatings", *Surf. and* Coat. Tech. 90 (1997): 234-238.

3.11 Residual stress

3.11.1 Definition

Residual stresses are defined as the "*stresses induced at the coating – substrate interface that may be due to the imperfections built in during the growth or it may be due to the mismatch in the coefficient of thermal expansion between the substrate and the deposit*" [1].

3.11.2 Standard methods

Optical interferometry [2] can be used for measuring the compressive residual strain in thin films. This is a fast, non-contact method of evaluation, capable of obtaining topographical 3-D data sets. This process requires the specimen as a free standing beam that is anchored at both ends. This is brought about by bulk micromachining processes. The interference profilometer is then used to measure the out-of-plane curvature in the free standing part of the specimen due to the stress. The length of the beam is measured by modeling a cosine function. The difference in length obtained is used for calculating the strain which in turn can be used to determine the associated stress.

3.11.3 Other methods

Residual stresses are contained in materials that are produced by nearly every manufacturing process. The stress can either be tensile or compressive. Extreme stress in a coating can either cause cracking or may even lead to coating detachment. Since residual stresses can substantially affect the service performance of a component, many methods are available for its characterization.

32

One of the widely used methods is the *deflection method* [3, 4] which involves measuring the amount of bending induced in a sample due to the deposition of the coating. The specimen is usually in the form of a cantilever that is fixed at one end and free at the other. A commercially available strain gauge is attached to the upper surface of the specimen. The test involves monitoring the change in output resistance of the gauge while the substrate is being coated. The mismatch in the cooling rates of the coating and the specimen induces a residual stress in the coating that causes it to bend. The strain produced due to this bending can be accurately measured by the strain gauge which in turn can be used to estimate the stress provided the elastic properties of the coating are known beforehand. Alternatively, the radius of curvature of the bent beam may also be measured by some optical methods to determine the stress.

Stress may also be measured by the *X-ray diffraction technique* [5, 6]. This method measures the strain induced in the crystal lattice due to the coating and thereby calculating the stress associated with the strain. When a sample is exposed to an X-ray beam, diffraction occurs at an angle 2θ defined by Bragg's law. Any stress present in the sample changes the lattice spacing which leads to a change in the diffraction angle. If the sample is rotated through a known angle, the stresses present in the surface will change the lattice spacing which in turn will cause a shift in the diffraction peak. The change in the angular positions of the diffraction peaks for these two orientations of the sample can be measured and this can be used to calculate of the stress present in the sample in the plane of diffraction.

The *laser curvature method* [4] can also be used to calculate the residual stresses in coatings. The system basically consists of a laser generator, an optical lens and a position sensitive detector. The laser generator is used to produce a parallel beam of light to scan the surface of the specimen. Parallel beams of light can be obtained by positioning a rotation mirror at the focal point of the lens. If the specimen surface is perfectly flat, the light rays will be reflected back to a single point on the focal plane. If any residual stress in present in the sample, it will introduce a curvature on the part of the specimen. The reflected rays from the surface will no longer be parallel and hence will not be focused at a single point. This displacement of the reflected light beams can be measured using the position detector and be used to estimate the radius of curvature. The stress can be calculated from the curvature using Stoney's formula [3].

3.11.4 Recommended method for testing and evaluation

Near-term solution: Deflection method

The deflection method is the most widely used technique for determining residual stress in a coating. This method involves measuring the change in radius of curvature of a substrate before and after it is coated. When a substrate is coated, residual stresses are set up due to the difference in thermal expansions of the coating and substrate. This mismatch at the interface causes the specimen to bend either upwards or downwards, depending upon the type of stress induced. If

this radius of curvature can be measured, the strain in the specimen can be calculated with formula developed by Stoney [3] and given by

$$\sigma = \frac{1}{6E(1-\upsilon)}\frac{t_s^2}{t_f}\frac{1}{R} \tag{1}$$

where $1/E(1-\nu)$ is the biaxial modulus of the substrate, t_s is the thickness of the substrate and t_f is the thickness of the film. In cases where the uncoated substrate has an inherent curvature (R_o), the above equation may be modified as

$$\sigma = \frac{1}{6E(1-\upsilon)}\frac{t_s^2}{t_f}\left(\frac{1}{R}-\frac{1}{R_0}\right) \tag{2}$$

The experimental setup (Figs. 1, 2) consists of a substrate fixed at one end like a cantilever with a strain gauge attached to its top surface. The bottom surface is exposed for film deposition. When the deposition process starts, residual stresses are setup in the specimen which causes it to bend. This bending induces a strain in the substrate which distorts the strain gauge attached to it resulting in a change in its electrical resistance. This change in resistance can be accurately measured and the corresponding strain can be calculated.
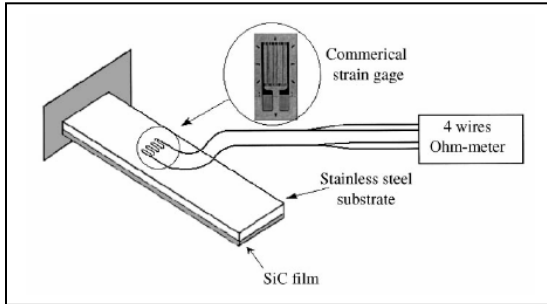
Fig. 1. Schematic representation of the set up   Fig. 2. Typical bending caused by stress [3].
for measurement of residual stress [2].

One very inexpensive and easy to perform deflection-based method suggested in [4] has been employed in order to obtain some qualitative information on the residual stress condition of the coatings. An *Almen* strip (manufactured by Electronics Inc., Mishawaka, IN, *www.shotpeener.com*) is mounted alongside the substrate and coated during the deposition process. The deflection of the *Almen* strip is read via an *Almen* mechanical gage before and after the coating deposition. Almen strips are actually precision springs made with tight tolerances from SAE grade 1070 steel. The most popular document for controlling the characteristics of the Almen strip is the *U. S. Government specification Mil-S-13165* issued on December 11, 1953.

Long-term solution: Optical interferometry [2]

An interference profilometer usually consists of an interferometric microscope, with vertical scanning capability. During the measurement process, the light source is split into two beams (Fig. 1). One beam is reflected off the surface of the sample and the other is reflected off a reference mirror. The vertical height of the

specimen at any particular point is determined by demodulating the interference
signal, created by combining the reflected light from the specimen surface and
the reflected light from a reference mirror. The use of white light in the process
results in a short coherence length for the interference pattern. This allows the
height measurements to be carried out with high accuracy.
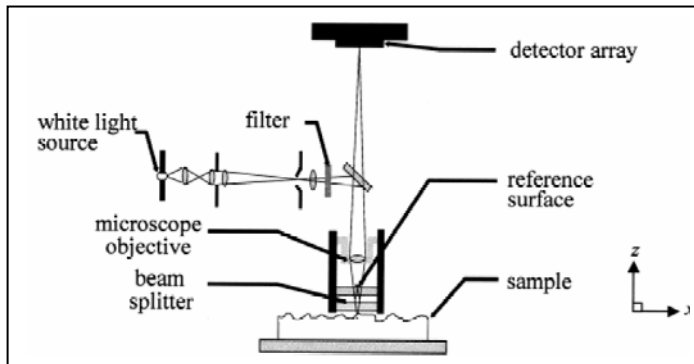

Fig. 1. Schematic representation of the optical
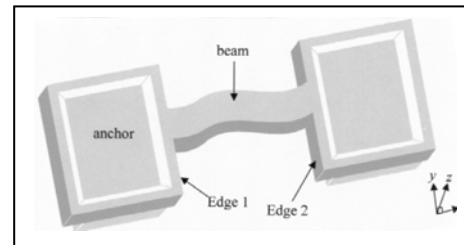interferometer [2].

Fig. 2. A micro-machined fixed-
fixed beam test specimen [2].

The first step consists of modeling the curvature of the beam using two cosine
functions that are merged at the peak or at the valley deflection. Three data
points are chosen to define each of these functions. The residual strain is then
determined from the calculated beam lengths. The data points required to define
each cosine function are determined in 5 steps: selecting four edges of the
specimen that have a distinct out-of-plane vertical displacement, obtaining a 3-D
data set, ensuring alignment, determining the endpoints of the in-plane length
measurement and finally, obtaining the three data points. The two cosine
functions are then plot with the available data to determine the length of the
curved fixed-fixed beam. The residual strain is then calculated from the
difference in lengths.

The most important part of the method is the specimen preparation. The test
structure must be in the form of a beam suspended in air and supported at both
ends and it should be of enough length to exhibit appreciable out of plane
curvature (Fig. 2). The dimensions of the beam should also be large enough to be
able to obtain the desired number of data points.

3.11.5 References

1. Bunshan R. F, Handbook of deposition technologies for films and coatings,
   2nd ed. Noyes Publications: Park Ridge (1994)
2. ASTM standard E 2245-02. Standard Test Method for Residual Strain
   Measurement of Thin, Reflecting films using an Optical Interferometer.
   ASTM International; 2003.
3. Cremonaa M, Gazolaa L.M, Scavarda do Carmoa L.C, Castrob J.T.P, Achetec
   C.A, "In situ hard coatings strain measurement using a commercial strain-
   gage device", *Thin Solid Films* 377-378 (2000) 436-440.
4. Lima R. S. and Marple B. R. "Abrasion Behavior in Nanostructured Alumina-
   Titania Coatings" *Proceedings from the 1st International Surface Engineering*

35

Congress and the 13th IFHTSE Congress, 7-10 October 2002, Columbus, Ohio.

5. Zhao Z.B, Hershberger J, Yalisove S.M, Bilello J.C, "Determination of residual stress in thin films: a comparative study of X-ray topography versus laser curvature method", *Thin Solid Films*, 415 (2002): 21–31.

6. Ma C.H, Huang J.H, Haydn Chen, "Residual stress measurement in textured thin film by grazing-incidence X-ray diffraction", *Thin Solid Films*, 418 (2002): 73–78.

3.12 Sliding (adhesive) wear

3.12.1 Definition

Sliding wear is here referred to as "*wear in a tribological system where the coated component slides against a relatively smooth counter surface, free from hard particles or hard asperities*" [1]. Naturally, sliding wear involves a very large group of tribological situations, and the wear may range from very mild chemical wear to severe adhesive wear and coating detachment, but is usually related to the adhesive wear only.

3.12.2 Standard methods

No standard methods that could be used for evaluating the sliding wear of thin hard coatings were identified. The method for estimating sliding wear by the *Reciprocating Ball-on-flat* apparatus [2] may be used as a reference when carrying out the test proposed as a long-term solution.

3.12.3 Other methods

Sliding wear occurs when interfaces in contact are made to slide and the locally adhered regions must separate Like in all wear tests, the simulation of the actual operating conditions is an important element of the test. The important parameters in sliding wear are the contact conditions (point contact, line contact, conforming etc), velocity and load at contact and the temperature at contact. The test configuration should be selected according to the desired contact condition. Some of the tests applicable to thin hard coatings are explained in this section. One of the simplest tests [1] involves sliding two elongated specimens against each other under a gradually increasing load. When the applied load exceeds the load bearing capacity of the specimens, coating failure will occur. The critical load can then be used as a measure of sliding wear resistance. This test is similar in mechanism to the scratch test and similar detecting devices like the acoustic detector can be used to identify the critical load. The contact geometry can be varied to simulate different contact conditions.

The b*all crater test* [3, 4] can be used to measure both the lubricated and un-lubricated sliding wear of thin hard coatings. In this test, a hardened steel ball is pressed and rotated against the specimen. The sliding of the ball causes a crater to be ground on the surface of the specimen. After a predefined number of rotations have elapsed, the specimen is removed and the crater dimensions are measured to evaluate the wear coefficient. A calibrated optical microscope is usually employed for measuring the diameter of the crater. The dimensions can

also be obtained by 3D optical profilometry. The wear coefficients of both the coating and the substrate can be calculated by this method. The test can also be carried out in the presence of a lubricant to evaluate the lubricated wear behavior of the coating.

Another method of evaluating the sliding wear is the *pin-on-disk test* [5]. In this method, the coatings are deposited on a cylindrical pin with a hemispherical contact tip. This pin is held stationary and in contact with a rotating disc made of the counter material. Both the pin and the disc should be polished to a very high degree of surface finish so that wear will be due to pure sliding. The pin is loaded and the test is conducted till the desired sliding distance is reached. After the completion of the test, the worn surfaces are analyzed by an optical microscope or by a profilometer. An alternate arrangement of the test involves reciprocating the disc against a spherical coated indenter. The test should be carried out long enough for appreciable mass loss to occur. So that the volume loss can be calculated and expressed as a measure of wear. Alternatively, the volume loss can also be determined from the dimensional change of the pin.

3.12.4 Recommended method for testing and evaluation

Near-term solution

Same as the long-term solution explained in the next section.

Long-term solution: **Ball Crater Test**

In this test, a sphere of hardened steel is made to rotate under load against the surface of the coated specimen (Fig. 1) (see also *Section 3.2.4* for using the ball crater test for evaluating the abrasive wear of thin film coatings and *Section* 3.13.4 for coating thickness). The normal load during the test is provided by the weight of the sphere and it can be adjusted within limits by varying the contact angle between the specimen and the sphere. For this purpose, the specimen is mounted on table with a variable inclination. An alternate arrangement involves clamping the specimen on a lever arm that can be loaded against the rotating ball. A constant tangential rotational velocity is imparted to the sphere through contact with a rotating shaft. The rotational frequency of the ball during the test can be determined with a phototransistor arrangement. A strong light beam is directed on the rotating ball using an optical fiber and the reflected signals are recorded by using a storage oscilloscope.
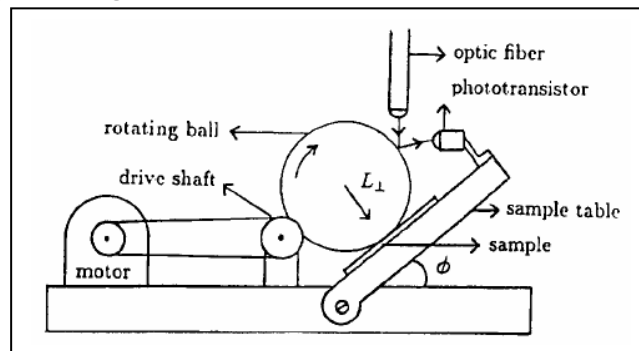

Fig. 1. Schematic representation of the ball crater test apparatus [1].

The irregularities in the surface reflectance of the ball produce periodic signals that are detected by the phototransistor and help in accurate determination of the frequency. Variations in the rotational frequency might occur due to slip between the ball and drive bar. This may be reduced by coating the drive bar with rubber to increase the friction between the ball and drive bar.

The action of the rotating sphere causes a wear scar to be imposed on the specimen surface, the diameter of which can be measured using a calibrated optical microscope. The crater diameter can then be used to determine the wear constant which is a measure of the wear resistance of the coating material. The wear constant can be determined using the following model [3],

$$k = \frac{D^2}{32fLt} \left\{ 1 - \left[1 - \frac{1}{4}\left(\frac{D}{r}\right)^2 \right]^{1/2} \right\} \tag{1}$$

where k - wear coefficient of the coating; D - crater diameter; f - rotational frequency of the sphere; L- load; t - time; r - radius of the sphere. This model has been developed considering the crater has the same geometry as the sphere. It is also important that the wear be contained with the thickness of the coating. If the coating is penetrated during the test, the substrate will contribute to the mass loss and the above model will no longer be valid. This situation should be avoided. A strain gauge may be added to the specimen for continuous monitoring of friction forces during the test. A continuous measure of the displacement can be obtained during the test if a displacement transducer is positioned above the specimen.

The use of this test is recommended because the same apparatus could be used for testing and measuring some other coating's parameter and characteristics. Various other adhesive wear tests, such as *block-on-ring* or *pin-on-disc* are more often used in the tribological practice for evaluating adhesive wear. The reason is that in adhesive wear testing it is desirable to be able to change both surfaces to be able to simulate service conditions. It is hard to coat balls or to make them out of some substrate materials. This is an advantage of a block-on-ring, crossed cylinder, or, to some extent, a pin-on-disc test.

3.12.5 References

1. Hogmark S, "Design and evaluation of tribological coatings" *Wear.* 246 (2000): 20-33.
2. ASTM standard G 133-02. Standard Test Method for Linearly Reciprocating Ball-on-Flat sliding wear. ASTM International; 2003.
3. Nothnagel G, "Wear resistance determination of coatings from cross-section measurements of ball-ground craters" *Surf. Coat. Tech.* 57 (1993): 151-154.
4. Gee M.G,Wicks M.J, "Ball crater testing for the measurement of the unlubricated sliding wear of wear-resistant coatings" *Surf. Coat. Tech.* 133-134 (2000) 376-382.
5. "Sliding contact damage testing" *ASM Handbook – Mech. Testing and Evaluation.* 8 (2000): 346-358.

3.13 Surface finish

3.13.1 Definition

Surface texture refers to "the locally limited deviations of a surface from the ideal intended geometry of the part". The surface may be considered to consist of components of different periodicities. These are referred to as roughness and waviness. Roughness is a "measure of the fine, closely spaced, random irregularities of surface texture caused by cutting tool marks, the grit of grinding wheels, and other process-related actions" and Waviness is a "measure of the wider-spaced repetitive irregularities caused by vibration, chatter, heat treatment, or warping strains".

3.13.2 Standard methods

The ASTM B 46 [1] is the standard that has been identified to deal with the geometric irregularities of the surface. It defines surface texture and its constituents: roughness, waviness, and lay. It also defines parameters for specifying surface texture. The terms and ratings in this standard relate to surfaces produced by such means as abrading, casting, coating, cutting, etching, plastic deformation, sintering, wear, erosion, etc. This standard also addresses the use of contact profilometry and interferometric microscope in the measurement of surface texture features.

3.13.3 Other methods

The most widely used technique to characterize the smoothness of a surface is the *stylus method* [2]. For investigating surface finish, the stylus should have a very small tip to be able to reproduce the irregularities on the surface and it should have a very light load so that the possibility of penetration of the surface is limited. When the stylus is made to traverse the surface of the specimen, it moves up and down due to the surface irregularities. This vertical movement of the stylus is converted into electrical signals by means of transducers attached to the stylus. The signal is then amplified and recorded on a strip chart. Roughness is the property which the stylus instruments measure. It is characterized numerically as the average deviations of the trace from an arbitrary mean.

Another important method is *optical profilometry* [3]. This is a fast, non-contact method of evaluating the surface texture of a component. A white light interference profilometer consists of an interferometric microscope with vertical scanning capability. During the test, the light source is split into two beams, one reflects off the surface of the specimen and the other is reflected from the reference mirror. These two beams are made to recombine at the detector to create interference fringes. This region of interference is recorded for each point along the surface and related to the location of the reference mirror to obtain a mapping of the roughness. The optical profilometers use two different measurement approaches to determine the surface characteristics depending on the magnitude of the surface irregularities: Phase shift interferometry and vertical scanning interferometry.

39

3.13.4 Recommended method for testing and evaluation

Near-term solution

Same as the long-term solution explained in the next section.

Long-term solution: Optical Interferometry

White light interferometry provides a fast, non-contact method of characterizing the surface topography of a component. An interference profilometer usually consists of an interferometric microscope, with vertical scanning capability (Fig. 1).
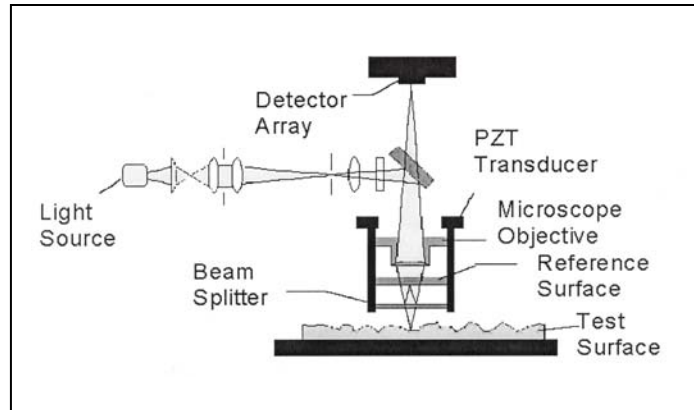

Fig. 1. Schematic representation of the optical interferometer [2].

The vertical height of the specimen at any particular point is determined by demodulating the interference signal created by combining the reflected light from the specimen surface and the reflected light from a reference mirror. The use of white light in the process results in a short coherence length for the interference pattern. This allows the height measurements to be carried out with high accuracy.

The process involves splitting the light source into two beams. One beam is reflected off the surface of the sample and the other is reflected off a reference mirror. The two reflected beams recombine at the detector to form an interference fringe pattern. Measurements are carried out by moving the objective vertically and recording the interference fringes at different heights. Usually a piezoelectric transducer is attached to the objective to increase the accuracy and to obtain a permanent record of the measurements. The region of interference is then recorded for each point and related to the location of the reference mirror along the z-axis. Lateral scanning of the specimen in the x-y plane results in a fast three-dimensional profile of the surface.
Some optical profilometers use two different measurement approaches to determine the surface characteristics depending on the magnitude of the surface irregularities, i.e., the *phase shift interferometry* and the *vertical scanning interferometry*.

40

In phase shift interferometry, a white light is filtered and passed through an interferometer objective to the test surface. The interferometer beam splitter reflects half of the incident beam to the reflected surface within the interferometer. The beams reflected from the test surface and the reference surface recombine to form interference fringes. These fringes are of alternate light and dark bands. During the measurement, a piezoelectric transducer linearly moves the reference surface a small, known amount to cause a phase shift between the test and reference beams. The system records the intensity of the resulting interference pattern at many different relative phase shifts, and then converts the intensity to wave front (phase) data by integrating the intensity data. The phase data are processed and the relative surface height is then calculated.

In vertical scanning interferometry, the white light source is filtered with a neutral density filter, which preserves the short coherence length of the white light, and the system measures the degree of fringe modulation, or coherence, instead of the phase of the interference fringes. The interferometer can produce various outputs like
  ▪ Roughness average (R_a), the arithmetic mean of the absolute values of the surface departures from the mean plane.
  ▪ Maximum profile peak/valley heights,
  ▪ Skewness, which measures the asymmetry of the surface about the mean plane, (positive, if surfaces are smooth but are covered with dust, spatters etc. and negative if the surface is smooth, but with deep scratches or pits)

Most profilometers also have an image analysis package that allows automated topographical calculations including height profiles, threshold surface area, surface depression volume, Fourier transforms, and power spectral density.

3.13.5 References
1. ASME standard B 46.1 (2002). Surface texture (Surface Roughness, Waviness and Lay). ASME International.
2. Maissel L. I, Glang R, Handbook of Thin Film Technology, *ASM Handbook – Mechanical Testing and Evaluation.* 12 (2000): 1246.
3. Kramb V, Shell E, Hoying J, Simon L, Meyendof N, "Applicability of white light scanning interferometry for high resolution characterization of surface defects".

3.14 Thickness

3.14.1 Definition
Thickness of a coating is defined here as *the perpendicular distance between the surface of the coating and the surface of the substrate on which it is deposited.*

3.14.2 Standard methods
One of the simplest methods of measuring the thickness is by observing the *cross-section* of a fractured coating. In this method [1], the coating is first over plated to a suitable thickness with a material of similar property. This serves to protect the coating when it is sectioned. A portion of the coating is then cut off

41

and mounted on a suitable material. The mounted specimen is then polished and etched taking care not to smear the interface. Etching serves to produce a clearly defined boundary between the coating and the substrate. The thickness of prepared specimen is then measured using a filar micrometer or a micrometer eye piece. The mean of a number of measurements along the interface is then reported as the thickness. The accuracy of this method depends on the instrument and the skill of the operator and reduces for thinner coatings, but the measurements are not affected by the material properties. Multilayered coating can also be measured by this method.

The *coulometric method* [2] is also commonly employed for coating thickness measurement. The thickness is determined by measuring the quantity of electricity required to dissolve the coating anodically from a known and accurately defined area. In the test, an electrolytic cell is formed with the specimen as the anode and with an electrolyte specifically selected for stripping the particular coating. A constant direct current is passed through the cell till the coating is completely depleted, which is marked by a sudden change in the voltage. The thickness of the coating may be calculated from the quantity of electricity used, the area of coating exposed, the electrochemical equivalent of the coating metal, the anodic-current efficiency, and the density of the coating.

The *beta backscatter method* [3] is a non-destructive method of estimating the coating thickness. This method measures the mass of coating per unit area, which can be used to express the thickness provided that the density of the coating is known. When a collimated beam of beta particles is directed on to the test specimen, a portion of these are reflected (i.e. backscattered) which is captured by a special Geiger Mueller tube. This backscatter is dependent on the atomic number of the material and therefore with proper instrumentation can be used for the measurement of the mass per unit area of the specimen. When the density of the coating is known, the thickness can be evaluated from the data obtained. Since both the coating and the substrate will cause backscattering, the method is applicable only if the atomic numbers or equivalent atomic numbers of the coating and substrate differ by an appropriate amount.

Another non-destructive method for thickness estimation is *X-ray spectrometry* [4]. This method also measures the mass per unit area of the coating which is used to calculate the thickness. When the test specimen is exposed to a collimated beam of X-rays, both the film and the substrate emit secondary radiation which is characteristic of the materials. Since the secondary radiation from the specimen contains many components apart from those characteristic of the coating and substrate, the desired components must be separated before their intensities can be measured. This can be done either by wavelength dispersion or by energy dispersion procedures. The measured intensities can then be correlated to the thickness by the use of primary standards.

42

3.14.3 Other methods

The *Ball Crater* technique [5, 6] used to measure the abrasive resistance and the
sliding wear of thin hard coatings (see also *Sections 3.2.4 & 3.11.4*) can be
successfully used to determine the coatings thickness, too. A hardened steel ball
is made to rotate on the surface of the specimen under load. The resulting wear of
the coating produces a taper section on the surface that can be used to measure
the coating thickness. Usually abrasive slurry is drip fed at the interface to
increase the wear rate.

3.14.4 Recommended method for testing and evaluation

Near-term solution

The *Ball Crater* technique will be a cost effective and easy to implement method
to measure the coating thickness along with some other parameters such as
abrasive wear resistance and coefficient of friction.

Long-term solution: Cross-sectioning method [1]

In this method, the thickness of the coating is measured from the microscopical
examination of the cross-section of the specimen using a microscope. The first
step consists of over plating the specimen to a thickness of about 10 μm. This is
done to prevent damage to the coating when it is cut off for mounting. Over
plating also helps to eliminate the rounding of the edges of the coating. The
specimen is then cut off, mounted and polished. Polishing is done by grinding the
specimen with a suitable abrasive paper in the presence of a lubricant. When
polishing is carried out minimum pressure should be applied to prevent beveling
of the surface. Once the desired degree of surface finish is achieved, etching is
carried out to improve the contrast between the metal layers. Etching also
removes any traces of smeared metal and produces a clearly defined and narrow
dark line at the interface of the two metals. The determination of the coating
thickness is performed by direct measurements on the polished cross-sections
using a SEM. At least five measurements of coating thickness are taken along the
micro-section of the specimen. The arithmetic average of the measurements is
then reported as the thickness.

The accuracy of this method depends on many factors like the surface roughness
of the substrate, accuracy of the measuring instrument, skills of the operator, etc.,
and reduces for thinner coatings, but the measurements are not affected by the
material properties. Multilayered coating can also be measured by this method. It
is sometimes advantageous to mount the sample at an angle to get an artificial
amplification of the cross section.

3.14.5 References

1. ASTM standard B 487-85(2002). Standard Test Method for Measurement of
   Metal and Oxide Coating Thickness by Microscopical Examination of a Cross
   Section. ASTM Int.; 2003.
2. ASTM standard B 504-90(2002). Standard Test Method for Measurement of
   Thickness of Metallic Coatings by the Coulometric Method. ASTM Int.; 2003.

3. ASTM standard B 567-98. Standard Test Method for Measurement of Coating
    Thickness by the Beta Backscatter Method. ASTM Int.; 2003.
4. ASTM standard B 568-98. Standard Test Method for Measurement of Coating
    Thickness by X-Ray Spectrometry. ASTM Int.; 2003.
5. Rutherford K.L, Hutchings I.M, "A micro-abrasive wear test, with particular
    application to coated systems" *Surf. Coat. Tech.* 79 (1996): 231-239.
6. Batista J.C.A, Joseph M.C, Godoy C, Matthews A, "Micro-abrasion wear
    testing of PVD TiN coatings on untreated and plasma nitrided AISI H13 steel",
    Wear 249 (2002) 971-979.

APPENDIX I

SUMMARY OF METHODS

Parameter	Method		Equipment		Page
	Near-term	Long-term	Near-term	Long-term	
Abrasive wear	Micro-abrasive test		Ball Crater Apparatus		9
Adhesion	Scratch test		Micro-scratch tester		13
Erosive wear	ASTM G76-02		Gas blast apparatus		16
Fatigue	Spherical rolling test		Spherical rolling tester		19
Fracture strength	Four-point bend test		Four-point bend tester		22
Coefficient of friction	Tribometry	Scanning probe microscopy	24	Scanning probe microscope	23
Hardness	Micro-hardness test		Nanoindenter		26
Modulus of elasticity		Micro-indentation test	29	Nanoindenter	29
Residual stress	Deflection test	ASTM E2245-02	32	Optical interferometer	32
Sliding wear	Ball crater test		Ball Crater Apparatus		36
Surface finish	Optical profilometry		Optical profilometer		38
Thickness	Ball crater test	ASTM B 487-85	41	SEM	41

APPENDIX II

RECOMMENDED STANDARDS

(Available in hard copy only)